Theoretical Investigation of the Optical Properties of Coupled Nano-Waveguides

Master Thesis
in Fulfillment of the Requirements of the Degree of

Master of Science in Physics

Submitted to the Institute of Applied Physics
of the Faculty of Physics and Astronomy
of the Friedrich-Schiller-University Jena

by Johannes Wilde
Born 1st of September 1991 in Göttingen
Matriculation Number: 125960

Jena, March 2017

Reviewers: Prof. Dr. rer. nat. Thomas Pertsch

Prof. Dr. rer. nat. Ulf Peschel

Contents

1. Introduction

Photon pair generation is a very interesting concept essential for quantum information networks [1, 2] or sensing application at otherwise unaccessible frequencies [3]. For the implementation several different materials with different non-linear processes have been used previously [4–6]. The aim of this thesis is to design and theoretically investigate the properties of photon-pair generation via spontaneous parametric down-conversion [SPDC] in a structure made of coupled periodic nano-waveguides [nano-WGs]. A sketch of the structure that is going to be investigated is shown in Fig. 1.

SPDC describes the spontaneous conversion of a single photon of a pump beam inside a non-linear optical material into two new photons, the signal and idler photons. For the optically non-linear material of the guiding structure lithium niobate [$LiNbO_3$] was chosen. It shows a strong χ_2 non-linearity [8], has a wide transparency window from 0.4 µm – 5 µm [9] and wafers of $LiNbO_3$ are commercially available.

Because the efficiency of non-linear optical processes is dependent on the intensity of the pump field, it was chosen to use waveguides [WGs] for the structure. These confine the light and thus prevent the loss of intensity usually experienced in homogeneous media by a broadening of the beam along propagation. The linear optical fields can then be described using WG-modes.

For an efficient conversion energy-conservation and the phase-matching condition have to be fulfilled. Therefore periodically structured nano-WGs were chosen. Nano-WGs, i.e. WGs with sub-wavelength transversal dimensions, offer a strong control over the properties of the guided modes. The periodic structuring allows to affect the modes in such a way, that different pairs of modes can be phase-matched to each other.

The periodic structuring at the same time can lead to slow light. This means that the energy of a mode propagates slower through the medium, compared to the speed of light in that medium. This slow down corresponds to an increase of intensity, which is

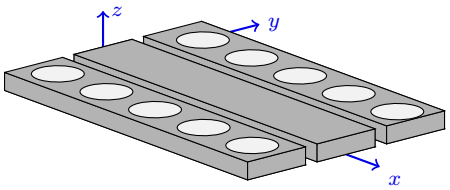

Fig. 1: Schematic view of the investigated structure, as proposed in [7] [shown without substrate here].

beneficial for the efficiency of the non-linear process.

Because the fabrication of nano-structures in $LiNbO_3$ still features challenges and small imperfections are unavoidable, one unit cell of the designed structure should be as big as possible, while still featuring the desired optical properties. In order to avoid mechanical problems, the structure is assumed to be on a substrate [silica, SiO_2]. This in conjunction with the periodicity will make the pump unavoidably lossy, as will be shown in section 2.2.

To prevent the pump from experiencing the periodicity and thus avoid its strong losses, the structure shown in Fig. 1 was chosen. Here the pump was assumed to be confined to the unstructured center WG, while signal and idler extend over all three WGs. The guided modes of signal and idler are, in contrast to the pump, inherently loss-less.

For an efficient numerical description an analytical formula will be presented in section 2.4, which describes the creation probabilities for different photon pairs in terms of the linear optical modes of the system via the joint spectral amplitude [JSA]. The linear optical modes are determined, using fully vectorial eigen-solvers for Maxwell's equations [11, 19].

This thesis is structured in the following way: In section 2 the theoretical framework is presented, explaining linear optics using Maxwell's equations, Bloch theory, perturbative weak-coupling theory and how the available numerical tools were used to calculate the needed solutions. Following this in section 3 a detailed description of the linear design of the proposed structure is presented. The properties of this linear design concerning SPDC are then numerically evaluated in section 4. To finish a conclusion is presented in section 5.

2. Analytical Description of SPDC in Coupled Periodic Waveguides

In this section the theoretical prerequisites for the simulation of spontaneous parametric down-conversion [SPDC] and the design of the properties of the created photon-pairs in coupled, periodically structured and anisotropic waveguides will be presented. In order to describe said systems efficiently with the available numerical tools, the rather weak non-linear process of SPDC was described analytically with a perturbation approach which uses the linear eigensolutions of the system as a basis. If one could derive those eigensolutions analytically, no numeric calculations would have been necessary at all [as long as one would also be able to solve the mathematical operations analytically]. This however was not the case, so that the modes [i.e. the linear optic eigensolutions] were obtained numerically and the actual evaluation of the formulas was done numerically as well.
The mathematical formalism and some useful physical insights that can be derived from it will be presented in section 2.1. The effects of the periodic structuring are best described using Bloch's theory, whose main results will be expressed in section 2.2. In section 2.3 the theory of weakly coupled waveguides [WGs] will be presented. Following that in section 2.4 a sketch of the analytical calculations for the description of SPDC will be given. And lastly there will be some explanations on what numerical methods were used [section 2.5] and how experimentally unavoidable losses were incorporated [section 2.6].

2.1. Linear Optics Using Maxwell's Equations

The propagation of light through linear optical materials is physically described as the evolution of electromagnetic fields characterized by permeabilities and susceptibilities. The most general equations, describing all purely electromagnetic phenomena, are the Maxwell equations [10, chapter 6.3]:

$$\begin{aligned} \vec{\nabla} \times \vec{E}(\vec{r},t) &= -\frac{\partial}{\partial t}\vec{B}(\vec{r},t) \quad , \quad \vec{\nabla} \times \vec{H}(\vec{r},t) = \vec{j}(\vec{r},t) + \frac{\partial}{\partial t}\vec{D}(\vec{r},t) \, , \\ \vec{\nabla} \cdot \vec{D}(\vec{r},t) &= \rho(\vec{r},t) \quad , \quad \vec{\nabla} \cdot \vec{B}(\vec{r},t) = 0 \, . \end{aligned} \tag{1}$$

$\vec{E}(\vec{r},t)$ is called the electric field, $\vec{D}(\vec{r},t)$ the displacement field, $\vec{H}(\vec{r},t)$ the magnetic field, $\vec{B}(\vec{r},t)$ the magnetic induction field, $\vec{j}(\vec{r},t)$ the free current density and $\rho(\vec{r},t)$ the free charge density.

Now dielectric media without free charges $[\rho(\vec{r},t) \equiv 0]$ and free currents $[\vec{\jmath}(\vec{r},t) \equiv 0]$ are assumed and for ease of notation the problem is reformulated in temporal Fourier space using complex numbers:

$$\vec{X}(\vec{r},t) =: \int_0^\infty \mathrm{d}\omega\, \vec{X}(\vec{r},\omega)\, \mathrm{e}^{-\mathrm{i}\omega t} + c.c. \quad , \quad \forall \vec{X} \in \{\vec{E},\vec{D},\vec{H},\vec{B}\}. \tag{2}$$

Please note that the different quantities are distinguished not only by their names, but also by there arguments. So $\vec{H}(\vec{r},t)$ is denoting the real-valued magnetic field and $\vec{H}(\vec{r},\omega)$ a complex-valued Fourier component.

For $\omega \neq 0$, which will be valid throughout this thesis, the lower equations in (1) are automatically fulfilled by solutions of the upper ones [11], so the only remaining equations are:

$$\vec{\nabla} \times \vec{E}(\vec{r},\omega) = \mathrm{i}\omega \vec{B}(\vec{r},\omega) \quad , \quad \vec{\nabla} \times \vec{H}(\vec{r},\omega) = -\mathrm{i}\omega \vec{D}(\vec{r},\omega)\,, \tag{3}$$

where linear, non-magnetic, inhomogeneous and anisotropic dielectric media are assumed:

$$\vec{D}(\vec{r},\omega) = \varepsilon_0 \overbrace{[1 + \hat{\chi}_1(\vec{r},\omega)]}^{\hat{\varepsilon}_r(\vec{r},\omega)} \vec{E}(\vec{r},\omega) \quad , \quad \vec{B}(\vec{r},\omega) = \mu_0 \vec{H}(\vec{r},\omega)\,. \tag{4}$$

ε_0 is the vacuum permittivity, μ_0 the vacuum permeability, $\hat{\chi}_1(\vec{r},\omega)$ the linear electric susceptibility tensor and $\hat{\varepsilon}_r(\vec{r},\omega)$ the relative permittivity tensor describing the linear optical properties of the media.

For non-magnetic and transparent media $\hat{\varepsilon}_r$ is real and can always be diagonalized by choosing a suitable coordinate system, the principal coordinate system. In this system the refractive index components are defined as follows: $n^\alpha = \sqrt{{\varepsilon_r}^{\alpha\alpha}}$, $\alpha \in \{1,2,3\}$. A crystal is called uniaxial if $n^1 = n^2 \neq n^3$ [coordinates chosen w.l.o.g.] or biaxial if $n^1 \neq n^2 \neq n^3 \neq n^1$ [12].

Using (4) in (3) to formulate the problem in terms of $\vec{H}(\vec{r},\omega)$ and $\vec{D}(\vec{r},\omega)$ only and following that replacing $\vec{D}(\vec{r},\omega)$ in the left one via the right one [positions as in (3)] and using the identity $\varepsilon_0\mu_0 = \dfrac{1}{c_0^2}$, with the vacuum speed of light c_0, one obtains the "master equation" [13]:

$$\vec{\nabla} \times \left[\hat{\varepsilon}_r^{-1}(\vec{r},\omega)\, \left[\vec{\nabla} \times \vec{H}(\vec{r},\omega)\right]\right] = \left[\frac{\omega}{c_0}\right]^2 \vec{H}(\vec{r},\omega)\,. \tag{5}$$

This is an eigenvalue problem purely in terms of $\vec{H}(\vec{r},\omega)$ with eigenvalue ω. Via (3) and (4) all other fields can be deduced from $\vec{H}(\vec{r},\omega)$.

Some general properties of the solutions can directly deduced from (5). For periodic and/or confined solutions it follows that $\omega \in \mathbb{R}$ [13]. Also the different eigensolutions $\vec{H}(\vec{r},\omega)$ are orthogonal under the following inner product:

$$\left(\vec{F},\vec{G}\right) = \iiint \vec{F}^* \cdot \vec{G}\, \mathrm{d}^3 r\ , \tag{6}$$

i.e.

$$\left(\vec{H}(\vec{r},\omega),\vec{B}(\vec{r},\omega')\right) = 0 \quad \text{and} \quad \left(\vec{D}(\vec{r},\omega),\vec{E}(\vec{r},\omega')\right) = 0 \quad \text{for} \quad \omega \neq \omega'\ . \tag{7}$$

But also for degenerate solutions, i.e. for $\omega = \omega'$, one can choose superpositions of those, which are orthogonal [13]. Thus, after normalizing all modes, one can calculate an orthonormal basis of electromagnetic modes from solutions of (5).

One useful characteristic for categorizing the modes is their symmetry. One necessity for modes to be able to exhibit a symmetry is that the initial problem is symmetric as well. This categorization will prove useful later on, because bands of opposing symmetry do not interact. What this means will be explained in the section 2.2.
In the following I will focus on the effects of a mirror-symmetry of the structure. Any field $f(x)$ will be called "even with respect to x" if $f(x) = f(-x)$ and labeled even(x) or "odd with respect to x" if $f(x) = -f(-x)$ and labeled odd(x).
For an anisotropic crystal in its principal axes system e.g. a x-mirror-symmetry [i.e. $\hat{\varepsilon}_r((x,y,z),\omega) = \hat{\varepsilon}_r((-x,y,z),\omega)$] is assumed. By making the corresponding coordinate transformation in (3), i.e. $(x,y,z) \to (-x,y,z)$, and then comparing the result with the un-transformed one, one can find two sets of solutions. The one set of modes will be called[1] x_{even} and features $E_x(\vec{r},\omega)$, $H_y(\vec{r},\omega)$ and $H_z(\vec{r},\omega)$ field components that are even with respect to x and $E_y(\vec{r},\omega)$, $E_z(\vec{r},\omega)$ and $H_x(\vec{r},\omega)$ field components that are odd[2] with respect to x. The other set is called x_{odd} and features $E_x(\vec{r},\omega)$, $H_y(\vec{r},\omega)$ and $H_z(\vec{r},\omega)$ field components that are odd with respect to x and $E_y(\vec{r},\omega)$, $E_z(\vec{r},\omega)$ and $H_x(\vec{r},\omega)$ field components that are even with respect to x.

Analogous classifications can be made for y- and z-mirror-symmetric problems. The results are shown in Table 1 on page 6.

The findings can be summarized as follows: For each mirror-symmetry [e.g. x-mirror-

[1] The naming convention of the modes in this thesis was chosen so that it corresponds to the outputs of the used simulation software. In looking at Table 1, we see that the label of the full mode corresponds to the symmetry of the $E_x(\vec{r},\omega)$-component. This differs from the notation e.g. in [13].

[2] The electric field is a true vector field, while the magnetic field is a pseudovector field. This is why each magnetic field component [e.g. H_x odd(x)] always exhibits the opposite symmetry compared to the same component of the electric field [E_x even(x)].

Table 1: Possible symmetries of the modes depending on the symmetry of the problem.

mirror symmetry of the problem	label of the full mode	possible symmetries of the solutions					
		$E_x(\vec{r},\omega)$	$E_y(\vec{r},\omega)$	$E_z(\vec{r},\omega)$	$H_x(\vec{r},\omega)$	$H_y(\vec{r},\omega)$	$H_z(\vec{r},\omega)$
x	x_{even}	even(x)	odd(x)	odd(x)	odd(x)	even(x)	even(x)
	x_{odd}	odd(x)	even(x)	even(x)	even(x)	odd(x)	odd(x)
y	y_{odd}	odd(y)	even(y)	odd(y)	even(y)	odd(y)	even(y)
	y_{even}	even(y)	odd(y)	even(y)	odd(y)	even(y)	odd(y)
z	z_{even}	odd(z)	odd(z)	even(z)	even(z)	even(z)	odd(z)
	z_{odd}	even(z)	even(z)	odd(z)	odd(z)	odd(z)	even(z)

symmetry] there are two groups of solutions [x_{even} and x_{odd}]. For each field [e.g. $\vec{E}$] in each group the field component corresponding to the direction of the mirror-symmetry [$E_x(\vec{r},\omega)$] has the opposite symmetry property [e.g. even(x)] compared to the other two components of the same field [here $E_y(\vec{r},\omega)$ and $E_z(\vec{r},\omega)$ are odd(x)].

The respective symmetries are not mutually exclusive. This means that if the initial problem exhibits more than one mirror-symmetry [e.g. in y and z], the solutions can be categorized in combinations of the categories corresponding to the single symmetries [e.g. $y_{\text{even}}z_{\text{odd}}$].

2.2. Bloch Theory and Band Diagrams

Felix Bloch published in 1928 a paper regarding the quantum mechanic description of electrons in crystals [14]. Crystals exhibit — in theory — perfect periodicity. Bloch reasoned that if the problem shows a periodicity, then the solutions will show the same. This idea is not restricted to electrons in crystals but can be applied to all problems, which can be described as a wave phenomenon in a periodic potential.

In order for the effect of the periodicity to be strong, the wavelength should be in the order of the periodicity. For wavelengths much larger than the periodicity an effective medium description will suffice, for wavelengths much smaller than the periodicity typically other effects dominate the properties of the solutions.

The optical equivalent to crystals are photonic crystals [PCs], which are dielectric materials with a macroscopic periodicity. The macroscopic periodicity corresponds to the bigger wavelength of light in the visible to infrared spectral range compared to electrons. Said periodicity can in PCs be one-dimensional [1D], two-dimensional [2D]

or three-dimensional [3D]. In the following the theory for 1D photonic crystals shall be presented in terms of one monochromatic magnetic field $\vec{H}(\vec{r},\omega)$, i.e. any of the Fourier components contributing to the physical field $\vec{H}(\vec{r},t)$.

For a possibly lossy, 1D-periodic photonic crystal [PC] the refractive index tensor reads as follows:

$$\hat{\varepsilon}_r(\vec{r},\omega) = \hat{\varepsilon}_r(\vec{r}+\vec{R}_n,\omega) \quad , \quad \forall \vec{R}_n = n\,\vec{a}\ ,\ n \in \mathbb{Z}\ . \tag{8}$$

For this thesis the direction of periodicity was w.l.o.g. chosen to be oriented along $\vec{e}_x$, so that the primitive lattice vector is $\vec{a} = a\,\vec{e}_x$.

From Bloch theory [14] it follows directly that the solutions can be written in the following form:

$$\vec{H}(\vec{r},\omega(k)) = \vec{H}(\vec{r},k)\ \mathrm{e}^{\mathrm{i}\,k\,x}\ . \tag{9}$$

k is the wavevector component along $\vec{e}_x$, $\vec{H}(\vec{r},\omega(k))$ are called Bloch modes and $\vec{H}(\vec{r},k)$ the Bloch mode profiles. The latter are periodic with the same periodicity as the structure, i.e. $\vec{H}(\vec{r},k) = \vec{H}(\vec{r}+\vec{R}_n,k)$. The k in this expression is the wavenumber along $\vec{e}_x$ and $\omega(k)$ the dispersion relation of the Bloch mode. The dispersion relations will be obtained numerically.

Bloch theory however not only predicts a periodicity of the solutions in real space, but also in the reciprocal space, i.e. in terms of the wavenumbers:

$$\omega(k) = \omega(k + n\frac{2\pi}{a}) \quad , \quad \forall n \in \mathbb{Z}\ . \tag{10}$$

From (9) one sees, that the Bloch modes will show the same periodicity in terms of k. Therefore it makes no sense to distinguish between the Bloch modes of k and $k + n\frac{2\pi}{a}$ and one restricts the values of k to $(-\frac{\pi}{a},\frac{\pi}{a}]$, the first Brillouin zone [1. BZ]. This does not mean that the wavenumbers of the modes are restricted as well. Every periodic function can be decomposed into a Fourier series. If one does so with the Bloch mode profiles, one will find:

$$\vec{H}(\vec{r},\omega(k)) = \Bigg[\overbrace{\sum_n \vec{h}(y,z,k+n\,\tfrac{2\pi}{a})\,\mathrm{e}^{\mathrm{i}\,n\frac{2\pi}{a}\,x}}^{\vec{H}(\vec{r},k)}\Bigg]\mathrm{e}^{\mathrm{i}\,k\,x} = \sum_n \vec{h}(y,z,k+n\,\tfrac{2\pi}{a})\,\mathrm{e}^{\mathrm{i}[k\,+\,n\frac{2\pi}{a}]x}\ . \tag{11}$$

Here one sees, that each Bloch mode consists of several WG mode-like fields $\vec{h}(y,z,k+n\,\frac{2\pi}{a})\,\mathrm{e}^{\mathrm{i}[k\,+\,n\frac{2\pi}{a}]x}$ with wavenumbers $k+n\,\frac{2\pi}{a}$. The x-independent $\vec{h}(y,z,k+n\,\frac{2\pi}{a})$ will be called Bloch harmonics.

Another important symmetry of the eigenvalues stems from the reciprocity of the used

optical materials. The reciprocity means, that forward and backward propagating modes behave the same way along their respective propagation direction. For the eigensolutions this means [15]

$$\vec{H}^*(\vec{r},\vec{k}) = \vec{H}(\vec{r},-\vec{k}) \quad , \quad \omega(\vec{k}) = \omega(-\vec{k}) \; . \tag{12}$$

The direct result of this is that only half of the 1. BZ has to be numerically simulated, as the other half can be obtained via simple mathematical operations.

A part of the dispersion relation $\omega(k)$ that is continuous and continuous in it's first derivative with respect to k will be called a band. Because typically one gets more than one band, each band will be labeled with an index i: $\tilde{\omega}_i(k)$.
The group velocity of the modes of band i can be directly deduced from the corresponding band

$$v_{\mathrm{gr}\,i}(k) = \frac{\partial}{\partial k}\tilde{\omega}_i(k) \; . \tag{13}$$

Analogous to the refractive index of an optical medium the slow-down factor of the mode relative to the speed of light in vacuum is called group index and defined as

$$n_{\mathrm{gr}_i}(k) = \frac{c_0}{v_{\mathrm{gr}\,i}(k)} \; . \tag{14}$$

The $+\vec{e}_x$ direction will be called "forward" and correspondingly every mode with a positive group velocity "forward propagating" and with a negative group velocity "backward propagating". For the special case of a group velocity equal to zero [$|n_{\mathrm{gr}\,i}(k)| \to \infty$] the mode will be called a "stopped mode".

In order to be able to unambiguously invert the dispersion relations later on, I am going to further divide all bands into continuous functions, where $\omega(k)$ is bijective; these will be called "bandlets" and denoted with $\omega_i(k)$. In the graphic image of a non-lossy band diagram this means that the bands are cut at the positions where the group velocity changes sign, i.e. at local extrema.

In order to better understand how to interpret a bandlet, three schematic non-lossy band diagrams are shown in Fig. 2 on page 9.

The first band diagram [Fig. 2 (a)] is for an isotropic, homogeneous medium $\varepsilon_r(\omega)$. The well known eigensolutions are transverse plane waves with the inverse dispersion relation [10, chapter 7]

$$\left|\vec{k}(\omega)\right| = \frac{n(\omega)}{c_0}\,\omega \tag{15}$$

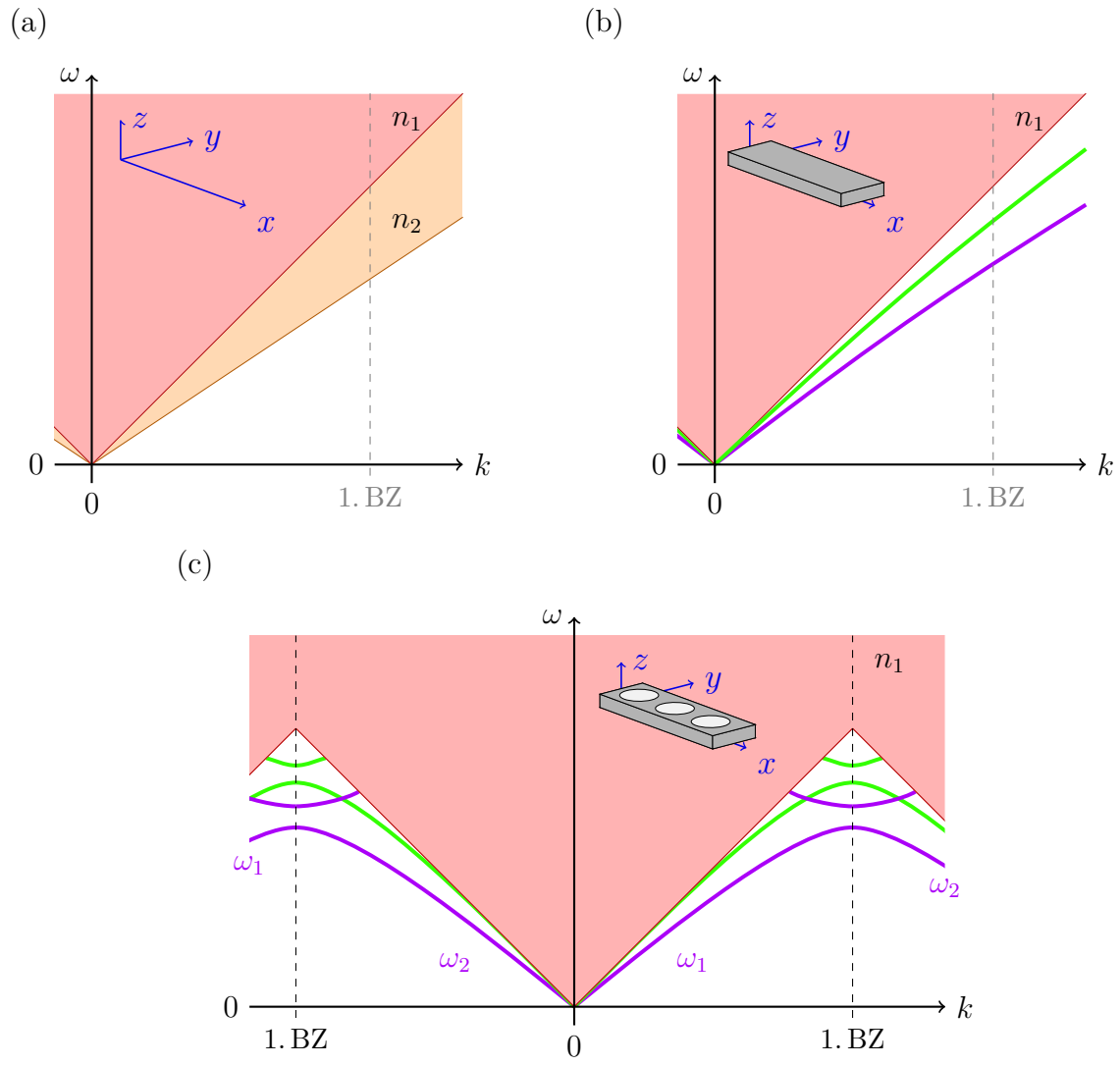

Fig. 2: Schematic band diagrams for three cases: (a) homogeneous media [refractive indices n_1 or n_2], (b) a single WG [n_2] in a surrounding medium [n_1] and (c) a 1D periodic WG [n_2] in a surrounding medium [n_1]. It is always $n_2 > n_1$. In the insets schematic sketches of an excerpt of a typical problem for the respective band diagram can be found. The border of the 1. BZ in (a) and (b) is only noted to make the axes of abscissa comparable to the one in (c). In the shaded regions an infinite number of modes exist. And the discrete modes in different colors exhibit different symmetries with respect to each other.

and the refractive index $n(\omega) = \sqrt{\varepsilon_r(\omega)}$.

As done throughout this thesis, the band diagram is shown as a function of k only. I will mention again that k is the x-component of the full wavevector $\vec{k}$. For the plane waves of the homogeneous medium the full wavevector can point into an arbitrary direction in

3D space. This means that for every $k < \frac{n(\omega)}{c_0}\,\omega$ there exist modes with $\vec{k}$-vectors with non-zero y- and/or z-components, which as well fulfill (15) at the same frequency. This is the reason, why for homogeneous media at least one mode exists for every point above the line $k = \frac{n(\omega)}{c_0}\,\omega$. The border line at $k = \frac{n(\omega)}{c_0}\,\omega$ is called the light-line of the medium. Its significance will be explained when discussing Fig. 2 (b). The higher the refractive index of the material is, the lower the light-line will be in the band-diagram.

For a WG consisting of a homogeneous high refractive index medium n_2 inside a surrounding of lower refractive index n_1, one will get a band diagram similar to the one shown schematically in Fig. 2 (b). Analogously to the effect of confinement of a system in quantum mechanics, one will not get a continuum of guided solutions, but a discrete spectrum of modes[3] seen by the bright and dark green lines in Fig. 2 (b). Alongside these also the modes of the surrounding medium exist.
For the optical design of a WG bigger refractive indices for the surrounding are unfortunate, as all WG modes that are at or above the light-line will be leaky. This is because for every WG mode at or above the light-line of the surrounding medium it exists at least one mode of the surrounding medium it can couple to. All energy coupled out of the WG is lost.
Below the light-line however no modes exist for the outer medium. For the modes of the WG one finds that the absolute value of it's wavenumber is bigger than the maximally allowed value for the outer medium, namely $\frac{n_1}{c_0}\omega$. To be able to fulfill the dispersion relation (15) in the surrounding medium, the transversal components have to be complex. This corresponds to an exponentially decaying amplitude transversal to the WG, which is why the mode is called "confined to the WG".

A schematic band diagram for a periodically structured WG is shown in Fig. 2 (c). As predicted by Bloch theory for a periodic medium [see (10)], the band diagram is periodic as well. In comparing Fig. 2 (c) to (b) a folding of the bands can be observed. At the same time the bands of the periodic structure differ from the ones of the unstructured WG in the important point, that the mainly straight lines are now parabolic when approaching the edges of the 1. BZ. The distance in frequency separating the new bands is called a "band gap".
The physical origin for the parabolic behavior of the bands at the edge of the 1. BZ is the interaction of the forward and backward propagating WG modes. This can be seen in (11), where the Bloch harmonics contributing to the full Bloch mode are written explicitly. This coupling of different modes results in a shift of the wavenumber $k(\omega)$.

[3]Where "mode" is just the physical equivalent to the mathematical term "eigensolution".

A periodic system is even stronger affected by the losses for WG modes above the light-line. That is because, as can be seen in Fig. 2 (c), the possible frequencies for guided modes are now limited to values smaller than $\frac{c_0}{n_1}\frac{\pi}{a}$ at the edges of the 1. BZ and to even smaller values everywhere else.

2.3. Coupling of Parallel, Unstructured Waveguides

The structure to be investigated in this thesis consists of three coupled WGs. Via the coupling one can adjust the interaction of the modes of the different WGs, which then affects the band diagram of the full structure. In order to get an idea of how the coupling of modes affects the overall solutions, I'm going to give an analytical result from a perturbative approach for weakly coupled WGs. For stronger coupling, as aspired for the final structure, this approach will break down and full numerical simulations will be necessary. To get an idea of the principle effect of coupling on a band diagram the following formulation nevertheless is instructive.

As a starting point two x-independent parallel WGs are considered. For simplicity of notation it is assumed that modes of only one bandlet of WG A couple with only one bandlet of the other WG B. The corresponding bandlets will be labeled $k^A(\omega)$ and $k^B(\omega)$. The normalized modes of the single WGs as well as of the coupled WGs are WG modes, whose electric field profiles can be described as follows [16]:

$$\vec{E}^X(\vec{r},\omega) = \vec{e}^X(y,z,k^X(\omega))\, \mathrm{e}^{\mathrm{i}\, k^X(\omega)x}\ , \tag{16}$$

where X is either A, B or AB and $\vec{e}^X(y,z,k_n(\omega))$ are the normalized[4] electric field profiles. A sketch of a typical problem is shown in Fig. 3.

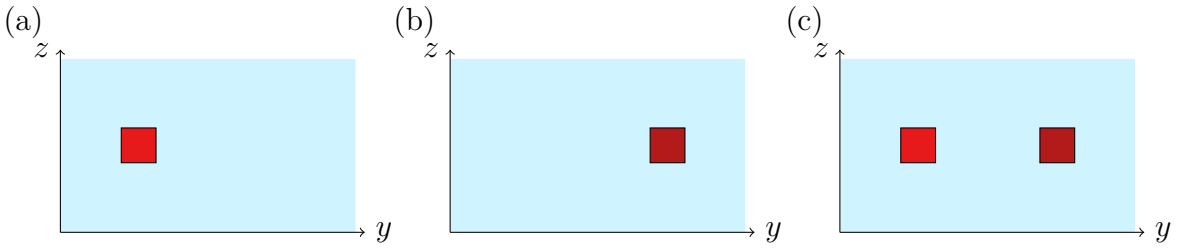

Fig. 3: Schematic pictures of the transversal profiles of two single waveguides [(a) $\hat{\varepsilon}_r^A$, (b) $\hat{\varepsilon}_r^B$] and the coupled system [(c) $\hat{\varepsilon}_r^{AB}$].

[4] I.e. $\iint_\perp \left[\vec{e}^X(y,z,k) \times \vec{h}^{X\,*}(y,z,k)\right] \cdot \vec{e}_x \,\mathrm{d}y\,\mathrm{d}z = 1$.

The approximative assumption used for the derivation of the final results is that the modes of the coupled structure $[AB]$, called "supermodes", can be described via simple superpositions of the modes of the single WGs. For strong coupling, i.e. when the WGs are close to each other, this assumption is not valid. For weak coupling, however, the following results can be obtained [16]:

$$k_{\pm}^{AB}(\omega) = \frac{k^A(\omega) + k^B(\omega)}{2} \pm \sqrt{\Delta^2(\omega) + \kappa^2(\omega)}\,, \tag{17}$$

with the phase mismatch term

$$\Delta(\omega) = \frac{k^A(\omega) - k^B(\omega)}{2}\,, \tag{18}$$

the coupling parameter from WG B to WG A

$$\kappa^{AB}(\omega) = \frac{\omega}{2} \iint_{\mathbb{R}^2} \varepsilon_0 \left[\hat{\varepsilon}_r^{AB}(y,z) - \hat{\varepsilon}_r^{B}(y,z)\right] \vec{e}^{\,B}(y,z,k^B(\omega)) \cdot \vec{e}^{\,A*}(y,z,k^A(\omega))\,\mathrm{d}y\,\mathrm{d}z\,, \tag{19}$$

the coupling parameter from WG A to WG B

$$\kappa^{BA}(\omega) = \frac{\omega}{2} \iint_{\mathbb{R}^2} \varepsilon_0 \left[\hat{\varepsilon}_r^{AB}(y,z) - \hat{\varepsilon}_r^{A}(y,z)\right] \vec{e}^{\,A}(y,z,k^A(\omega)) \cdot \vec{e}^{\,B*}(y,z,k^B(\omega))\,\mathrm{d}y\,\mathrm{d}z \tag{20}$$

and the full coupling parameter as seen in the splitting of the bandlets

$$\kappa(\omega) = \sqrt{\kappa^{AB}(\omega)\,\kappa^{BA}(\omega)}\,. \tag{21}$$

Before interpreting these results, I will mention that $[\hat{\varepsilon}_r^{AB}(y,z) - \hat{\varepsilon}_r^{A}(y,z)]$ differs drastically from $\hat{\varepsilon}_r^{B}(y,z)$. The first quantity is non-zero at the positions of WG B only, while $\hat{\varepsilon}_r^{B}(y,z)$ is non-zero everywhere. As a result the integral in (19) needs only be evaluated over the transverse section of WG A. The same holds for (20) and WG B.

To better understand the effects of (17)–(21) an excerpt of a schematic band diagram is shown in Fig. 4. There the bandlets of the single WGs $k^A(\omega)$ and $k^B(\omega)$ as well as the coupled bandlets of the full structure $k_{\pm}^{AB}(\omega)$ are shown.
Right at the crossing of $k^A(\omega)$ and $k^B(\omega)$ the phase mismatch is zero and the bandlets of the coupled structure most strongly affected by the coupling. The further away one gets from the crossing point, the bigger the phase mismatch becomes and correspondingly the coupling weaker. Too far away from the crossing the bandlets $k_{\pm}^{AB}(\omega)$ will coincide with $k^A(\omega)$ or $k^B(\omega)$ again. This way the part of $k^A(\omega)$ below the crossing and the part of

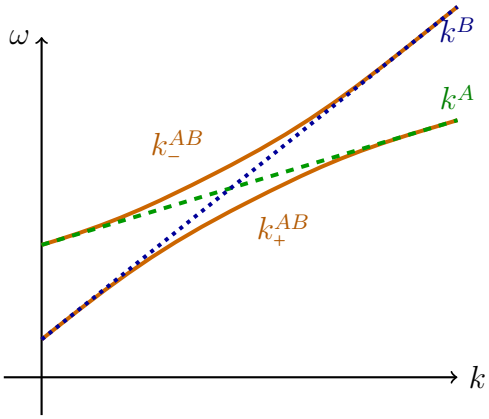

Fig. 4: Schematic excerpt of a band diagram showing the uncoupled bandlets $k^A(\omega)$ [dashed line] and $k^B(\omega)$ [dotted line] and the anti-crossing bandlets $k_+^{AB}(\omega)$ and $k_-^{AB}(\omega)$ [solid lines] of the coupled structure.

$k^B(\omega)$ above the crossing are connected in $k_-^{AB}(\omega)$ and vice versa in $k_+^{AB}(\omega)$.

Because this way a crossing of bandlets for the coupled structure is avoided, this effect is called “anti-crossing”.

For the special case of coupled identical WGs the same descriptions holds. For the coupling of the same modes in the two WGs above formulas then simplify because the bandlets are identical. The phase mismatch is correspondingly zero over the full bandlet and the effect of (17) in the resulting band diagram looks not so much like an anti-crossing but like a symmetric shift by $\kappa(\omega)$ left and right of the bandlet of the single WG. This result will be especially useful in section 3.3.

2.4. Perturbative Description of Spontaneous Parametric Down-Conversion

Now that the prerequisites for understanding the linear optical properties of the investigated structure are stated, I will now focus on the non-linear optical interaction. For the chosen process of spontaneous parametric down-conversion [SPDC], which is a quantum optical effect, the creation probabilities for different photon pairs will be written analytically in terms of the involved modes. SPDC describes the down-conversion of a photon of a pump beam sent into a $\hat{\chi}_2$ non-linear medium to two new ones, called signal and idler. In the following a sketch of the derivation of the necessary formalism for SPDC in 1D periodic, non-linear media, which are Kleinman-symmetric [12], will be

presented. In order to keep it short and because most important parts can be understood this way, I will restrict this description to the case of lossless signal and idler. A more general result will be given in the end.

The general approach will be very similar to the description of the coupling of the WGs above: The system will be first described linearly, i.e. in terms of modes. The non-linear process will then be a perturbation and describe the coupling of different modes.

Following Sipe et al. [17] the system is described using number states[5] and accordingly the following notation for the three fields[6] of SPDC in a $1D$-periodic [w.l.o.g. along $\vec{e}_x$] photonic system is introduced:

$$\hat{\vec{\mathfrak{E}}}^{(\zeta)}(\vec{r}) = \sum_m \!\!\!\!\!\!\int \mathrm{d}k \left[\hat{a}^{(\zeta)}_{mk}\, \vec{E}^{(\zeta)}_m(\vec{r},k) \frac{\mathrm{e}^{\mathrm{i}\,kx}}{\sqrt{2\pi}} + \hat{a}^{(\zeta)\,\dagger}_{mk}\, \vec{E}^{(\zeta)\,*}_m(\vec{r},k) \frac{\mathrm{e}^{-\mathrm{i}\,kx}}{\sqrt{2\pi}} \right] \sqrt{\frac{\hbar\omega^{(\zeta)}_m(k)}{2}} \,. \tag{22}$$

Here m numbers the bandlets, ζ names pump $[p]$, signal $[s]$ or idler $[i]$ respectively, † means the adjoint, * means complex conjugate and $\hat{a}^{(\zeta)}_{mk}$ or $\hat{a}^{(\zeta)\,\dagger}_{mk}$ are the annihilation or creation operators for the mode of ζ in bandlet m at k. Similar notations can be formulated for $\hat{\vec{D}}(\vec{r})$, $\hat{\vec{H}}(\vec{r})$ and $\hat{\vec{B}}(\vec{r})$ as well. I would like to note that the field operators do not show any time dependence, because this problem is formulated in the Schrödinger picture now.
With the commutator $\left[\hat{a},\hat{b}\right] = \hat{a}\hat{b} - \hat{b}\hat{a}$, Kronecker delta $\delta_{mm'}$ and Dirac delta function $\delta(k-k')$ one requires for a canonical formulation:

$$\left[\hat{a}^{(\zeta)}_{mk}, \hat{a}^{(\zeta)}_{m'k'}\right] = 0 \quad \text{and} \quad \left[\hat{a}^{(\zeta)}_{mk}, \hat{a}^{(\zeta)\,\dagger}_{m'k'}\right] = \delta_{mm'}\,\delta(k-k') \,. \tag{23}$$

The amplitudes of the modes are normalized as follows [assuming as above a non-magnetic medium and only confined modes]:

$$\iiint_{\mathrm{UC}} \mathrm{d}^3 r\, \varepsilon_0 \varepsilon_r^{\alpha\beta}(\vec{r})\, E^{(\zeta)*\alpha}_m(\vec{r},k)\, E^{(\zeta)\beta}_{m'}(\vec{r},k) = \delta_{mm'} \,. \tag{24}$$

Here UC stands for one unit cell of the considered structure, α and β are labeling the three spatial components and Einstein summation convention is used.

The Hamiltonian, i.e. the operator, which expectation value is understood to be the

[5] Also called Fock states.

[6] Physically there are no three different fields, it is $\hat{\vec{E}}(\vec{r}) = \sum_\zeta \hat{\vec{E}}^{(\zeta)}(\vec{r})$. For this notation however I will distinguish between them.

energy of the state of the system, of an electro-magnetic system is the following [17]:

$$\hat{H} = \iiint \mathrm{d}^3 r \left[\int_0^{\hat{\vec{B}}(\vec{r})} \hat{\vec{H}}'(\vec{r})\, \mathrm{d}\hat{\vec{B}}'(\vec{r}) + \int_0^{\hat{\vec{D}}(\vec{r})} \hat{\vec{E}}'(\vec{r})\, \mathrm{d}\hat{\vec{D}}'(\vec{r}) \right] . \tag{25}$$

For an intrinsically lossless, non-magnetic medium away from any material resonances, where Kleinman symmetry holds [12], and assuming only weak $\hat{\chi}_2$-effects, one can show that the Hamiltonian now takes the following form [15]:

$$\hat{H} \approx \overbrace{\sum_\zeta \oint_m \mathrm{d}k \, [\underbrace{\hat{a}_{mk}^{(\zeta)\dagger} \hat{a}_{mk}^{(\zeta)}}_{=\hat{N}_{mk}^{(\zeta)}} + \tfrac{1}{2}] \, \hbar\omega_m^{(\zeta)}(k)}^{\hat{H}_{\mathrm{lin}}} \overbrace{- \frac{\varepsilon_0}{3} \iiint \mathrm{d}^3 r \, \hat{E}^\alpha(\vec{r}) \chi_2^{\alpha\beta\gamma}(\vec{r}) \hat{E}^\beta(\vec{r}) \hat{E}^\gamma(\vec{r})}^{\hat{H}_{\mathrm{NL}}} . \tag{26}$$

Here $\hat{N}_{mk}^{(\zeta)}$ is the number operator, $\hat{H}_{\mathrm{lin}}$ the Hamiltonian considering purely linear optics and $\hat{H}_{\mathrm{NL}}$ the part describing the non-linear effects.

Because the conversion efficiency is very low the pump is assumed to be a classical field and undepleted:

$$\vec{E}^{(p)}(\vec{r}, t) = \oint_m \mathrm{d}\omega A_m^{(p)}(\omega) \underbrace{\vec{e}_m^{(p)}(\vec{r}, \omega)\, \mathrm{e}^{\mathrm{i}\, k_m^{(p)}(\omega) x}}_{\vec{E}_m^{(p)}(\vec{r}, \omega)} \mathrm{e}^{-\mathrm{i}\,\omega t} + c.c. . \tag{27}$$

Signal and idler will be rewritten in terms of ω instead of k as well. Because this transformation requires a monotonic relation of k and ω, bandlets and not full bands have to be used here. Considering this I used $\hat{a}_{m\omega}^{(\zeta)} := \sqrt{\left|\frac{\partial k_m^{(\zeta)}(\omega)}{\partial \omega}\right|} \hat{a}^{(\zeta)}_{mk_m^{(\zeta)}(\omega)} = \sqrt{\frac{1}{c_0}\left|n_{\mathrm{gr}m}^{(\zeta)}(\omega)\right|}\, \hat{a}^{(\zeta)}_{mk_m^{(\zeta)}(\omega)}$, $n_{\mathrm{gr}m}^{(\zeta)}(\omega) = n_{\mathrm{gr}m}^{(\zeta)}(k_m^{(\zeta)}(\omega))$ and $\vec{e}_m^{(\zeta)}(\vec{r}, \omega) = \vec{E}_m^{(\zeta)}(\vec{r}, k_m(\omega))$ and got:

$$\hat{\vec{E}}^{(\zeta)}(\vec{r}) = \oint_m \mathrm{d}\omega \left[\hat{a}_{m\omega}^{(\zeta)}\, \vec{e}_m^{(\zeta)}(\vec{r}, \omega) \frac{\mathrm{e}^{\mathrm{i}\, k_m^{(\zeta)}(\omega) x}}{\sqrt{2\pi}} + \hat{a}_{m\omega}^{(\zeta)\dagger}\, \vec{e}_m^{(\zeta)\,*}(\vec{r}, \omega) \frac{\mathrm{e}^{-\mathrm{i}\, k_m^{(\zeta)}(\omega) x}}{\sqrt{2\pi}} \right] \sqrt{\frac{\hbar\omega \left|n_{\mathrm{gr}m}^{(\zeta)}(\omega)\right|}{2c_0}} . \tag{28}$$

Considering all of the above and additionally using the knowledge that in SPDC one signal and one idler photon are created and one pump photon destroyed, i.e. all other un-phase-matched-to terms are disregarded at this point already, the non-linear Hamiltonian can be shown to have the following form:

$$\begin{aligned}\hat{H}_{\mathrm{NL}} \approx \frac{-\hbar\varepsilon_0}{2\pi c_0} \oint\!\!\!\!\!\!\int_{m_p m_s m_i} \mathrm{d}\omega_p\,\mathrm{d}\omega_s\,\mathrm{d}\omega_i\; \mathrm{e}^{-\mathrm{i}\,\omega_p t}\; A^{(p)}_{m_p\omega_p}\,\hat{a}^{(s)\dagger}_{m_s\omega_s}\,\hat{a}^{(i)\dagger}_{m_i\omega_i}\sqrt{\left|n^{(s)}_{\mathrm{gr}\,m_s}(\omega_s)\right|\left|n^{(i)}_{\mathrm{gr}\,m_i}(\omega_i)\right|} \\ \sqrt{\omega_s\omega_i}\iiint \mathrm{d}^3 r\,\chi_2^{\alpha\beta\gamma}(\vec{r})\,e^{(p)\,\alpha}_{m_p}(\vec{r},\omega_p)\,e^{(s)\,*\,\beta}_{m_s}(\vec{r},\omega_s)\,e^{(i)\,*\,\gamma}_{m_i}(\vec{r},\omega_i) \\ \mathrm{e}^{\mathrm{i}\left[k^{(p)}_{m_p}(\omega_p)-k^{(s)}_{m_s}(\omega_s)-k^{(i)}_{m_i}(\omega_i)\right]x} \;+\; H.c. \\ =: \frac{-\hbar\varepsilon_0}{2\pi c_0} \oint\!\!\!\!\!\!\int_{m_p m_s m_i} \mathrm{d}\omega_p\,\mathrm{d}\omega_s\,\mathrm{d}\omega_i\; \mathrm{e}^{-\mathrm{i}\,\omega_p t}\;\hat{a}^{(s)\dagger}_{m_s\omega_s}\,\hat{a}^{(i)\dagger}_{m_i\omega_i}\,S_{m_p m_s m_i}(\omega_p,\omega_s,\omega_i) + H.c.\end{aligned} \tag{29}$$

Here $H.c.$ stands for the Hermitian conjugate and $\frac{\varepsilon_0}{c_0}\,S_{m_p m_s m_i}(\omega_p,\omega_s,\omega_i)$ for the joint spectral amplitude [JSA].

In the exponential of above equation the well known phase-matching term can be seen. Because the phase-matching however is really between the Bloch harmonics, a more explicit expression for the phase-matching is going to be introduced. The additional quantities $\mathfrak{b}^{(\zeta)}_m \in \mathbb{Z}$ will be chosen so, that the Bloch harmonic with $\tilde{k}_m = k_m + \mathfrak{b}^{(\zeta)}_m \frac{2\pi}{a}$ couple most efficiently. The phase-mismatch then reads

$$\Delta k_{m_p m_s m_i}(\omega_p,\omega_s,\omega_i) := k^{(p)}_{m_p}(\omega_p) - k^{(s)}_{m_s}(\omega_s) - k^{(i)}_{m_i}(\omega_i) + \overbrace{\left[\mathfrak{b}^{(p)}_{m_p} - \mathfrak{b}^{(s)}_{m_s} - \mathfrak{b}^{(i)}_{m_i}\right]\frac{2\pi}{a}}^{=:\Delta\mathfrak{b}_{m_p m_s m_i}} . \tag{30}$$

Using additionally the periodicity of the structure as well as of the mode profiles the mode-overlap term in $S_{m_p m_s m_i}(\omega_p,\omega_s,\omega_i)$ can be rewritten. In the intermediate steps all non-essential arguments and indices are left out, so that the steps can be easier understood.

$$\begin{aligned}&\iiint \mathrm{d}^3 r\,\chi_2^{\alpha\beta\gamma}(\vec{r})\,e^{(p)\,\alpha}_{m_p}(\vec{r},\omega_p)\,e^{(s)\,*\,\beta}_{m_s}(\vec{r},\omega_s)\,e^{(i)\,*\,\gamma}_{m_i}(\vec{r},\omega_i)\,\mathrm{e}^{\mathrm{i}\left[k^{(p)}_{m_p}(\omega_p)-k^{(s)}_{m_s}(\omega_s)-k^{(i)}_{m_i}(\omega_i)\right]x} \\ &=: \iiint \mathrm{d}^3 r\,\chi_2^{\alpha\beta\gamma}\,e^{(p)\,\alpha}\,e^{(s)\,*\,\beta}\,e^{(i)\,*\,\gamma}\,\mathrm{e}^{\mathrm{i}\left[k^{(p)}-k^{(s)}-k^{(i)}\right]x} \\ &= \iiint \mathrm{d}^3 r\,\chi_2^{\alpha\beta\gamma}\,e^{(p)\,\alpha}\,e^{(s)\,*\,\beta}\,e^{(i)\,*\,\gamma}\,\mathrm{e}^{\mathrm{i}\left[\Delta k-\Delta\mathfrak{b}\right]x} \\ &= \int_0^{N\,a}\mathrm{d}x\iint_{\mathbb{R}^2}\mathrm{d}y\,\mathrm{d}z\,\chi_2^{\alpha\beta\gamma}\,e^{(p)\,\alpha}\,e^{(s)\,*\,\beta}\,e^{(i)\,*\,\gamma}\,\mathrm{e}^{-\mathrm{i}\,\Delta\mathfrak{b}\,x}\,\mathrm{e}^{\mathrm{i}\,\Delta k\,x} \\ &=: \sum_{n=0}^{N-1}\int_0^{a}\mathrm{d}x\iint_{\mathbb{R}^2}\mathrm{d}y\,\mathrm{d}z\,f(x+na)\,\mathrm{e}^{\mathrm{i}\,\Delta k[x+na]} \\ &= \int_0^{a}\mathrm{d}x\iint_{\mathbb{R}^2}\mathrm{d}y\,\mathrm{d}z\,f(x)\sum_{n=0}^{N-1}\mathrm{e}^{\mathrm{i}\,\Delta k[x+na]} .\end{aligned} \tag{31}$$

Here the length of the structure was assumed to be $L = Na$ and in the second to last equality the periodicity of $f(x)$ was used [$f(x+na) = f(x)$]. For clarity I will mention

that all terms in the last expression are still inside the integral.
In order to analytically evaluate this expression, the fact that the phase-mismatch is small and thus the terms in the sum slowly varying over the course of one period was used. That is why the sum is taken out of the integral. Following this the sum is approximated with an integral and can be expressed analytically:

$$\begin{aligned}
&\iiint_{\mathrm{UC}} \mathrm{d}^3 r\, f(x) \sum_{n=0}^{N-1} \mathrm{e}^{\mathrm{i}\,\Delta k [x+na]} \\
&\approx \left[\iiint_{\mathrm{UC}} \mathrm{d}^3 r\, f(x)\right] \sum_{n=0}^{N-1} \mathrm{e}^{\mathrm{i}\,\Delta k\, na} \\
&\approx \left[\iiint_{\mathrm{UC}} \mathrm{d}^3 r\, f(x)\right] \frac{1}{a} \int_0^{Na} \mathrm{d}x\, \mathrm{e}^{\mathrm{i}\,\Delta k\, x} \\
&= \left[\iiint_{\mathrm{UC}} \mathrm{d}^3 r\, f(x)\right] \frac{\mathrm{e}^{\mathrm{i}\,\Delta k\, Na} - 1}{\mathrm{i}\,\Delta k a} \\
&= \left[\iiint_{\mathrm{UC}} \mathrm{d}^3 r\, \chi_2^{\alpha\beta\gamma}\, e_{m_p}^{(p)\,\alpha}(\vec{r},\omega_p)\, e_{m_s}^{(s)\,*\,\beta}(\vec{r},\omega_s)\, e_{m_i}^{(i)\,*\,\gamma}(\vec{r},\omega_i)\, \mathrm{e}^{-\mathrm{i}\,\Delta\mathfrak{b}_{m_p m_s m_i} x}\right] \\
&\qquad\qquad \frac{\mathrm{e}^{\mathrm{i}\,\Delta k_{m_p m_s m_i}(\omega_p,\omega_s,\omega_i) L} - 1}{\mathrm{i}\,\Delta k_{m_p m_s m_i}(\omega_p,\omega_s,\omega_i)\, a}\,.
\end{aligned} \tag{32}$$

The integration is now over one unit cell only. Especially for long structures this notably decreases the time and memory one needs for the numerical calculations.

The fraction in the last expression can be rewritten as follows[7]:

$$\mathrm{e}^{\mathrm{i}\,\Delta k_{m_p m_s m_i}(\omega_p,\omega_s,\omega_i)\frac{L}{2}}\, N \operatorname{sinc}\left(\Delta k_{m_p m_s m_i}(\omega_p,\omega_s,\omega_i)\,\frac{L}{2}\right). \tag{33}$$

Here one sees directly, that on a global scale a bigger phase-mismatch leads to a smaller JSA $S_{m_p m_s m_i}(\omega_p,\omega_s,\omega_i)$. "global" is used here, to exclude the local oscillations of the $\operatorname{sinc}()$ function. A smaller JSA corresponds to a smaller creation probability of the corresponding signal and idler photons, as can be seen further below.

Combining (29) and (32) $S_{m_p m_s m_i}(\omega_p,\omega_s,\omega_i)$ can be rewritten.

$$\begin{aligned}
S_{m_p m_s m_i}(\omega_p,\omega_s,\omega_i) \approx A_{m_p\omega_p}^{(p)} \sqrt{\omega_s\omega_i} \sqrt{\left|n_{\mathrm{gr}\,m_s}^{(s)}(\omega_s)\right|\left|n_{\mathrm{gr}\,m_i}^{(i)}(\omega_i)\right|}\, \frac{\mathrm{e}^{\mathrm{i}\,\Delta k_{m_p m_s m_i}(\omega_p,\omega_s,\omega_i) L} - 1}{\mathrm{i}\,\Delta k_{m_p m_s m_i}(\omega_p,\omega_s,\omega_i)\, a} \\
\left[\iiint_{\mathrm{UC}} \mathrm{d}^3 r\, \chi_2^{\alpha\beta\gamma}(\vec{r})\, \vec{e}_{m_p}^{(p)}(\vec{r},\omega_p)\, \vec{e}_{m_s}^{(s)*}(\vec{r},\omega_s)\, \vec{e}_{m_i}^{(i)*}(\vec{r},\omega_i)\, \mathrm{e}^{-\mathrm{i}\,\Delta\mathfrak{b}_{m_p m_s m_i} x}\right].
\end{aligned} \tag{34}$$

[7] The convention $\operatorname{sinc}(x) = \frac{\sin(x)}{x}$ is used.

Now that the JSAs $S_{m_p m_s m_i}(\omega_p, \omega_s, \omega_i)$ are in a numerically convenient form, I will isolate the effects of the non-linear Hamiltonian. Therefore the description is transformed from the Schrödinger picture $[\mathrm{i}\hbar\partial_t |\Psi(t)\rangle = \left[\hat{H}_{\mathrm{lin}} + \hat{H}_{\mathrm{NL}}\right] |\Psi(t)\rangle]$ to an interaction picture $[\mathrm{i}\hbar\partial_t |\Psi_I(t)\rangle = \hat{H}_{\mathrm{NL}\,I}(t) |\Psi_I(t)\rangle]$. With the time evolution operator of the linear Hamiltonian

$$\hat{U}_0(t_0, t) = \mathcal{T}\left(\mathrm{e}^{\frac{1}{\mathrm{i}\hbar}\int_{t_0}^{t} \mathrm{d}t'\, \hat{H}_{\mathrm{lin}}}\right) , \tag{35}$$

where $\mathcal{T}()$ is the time-ordering operator, the relevant transformations are

$$|\Psi_I(t)\rangle = \hat{U}_0^{(-1)}(t_0, t) |\Psi(t)\rangle \quad , \quad \hat{H}_{\mathrm{NL}\,I}(t) = \hat{U}_0^{(-1)}(t_0, t)\, \hat{H}_{\mathrm{NL}}\, \hat{U}_0(t_0, t) . \tag{36}$$

The non-linear Hamiltonian in the chosen interaction picture then reads as [the differences to the Hamiltonian of the Schrödinger picture in (29) are set in bold]

$$\hat{H}_{\mathrm{NL}\,I}(t) = \frac{-\hbar\varepsilon_0}{2\pi c_0} \iint_{m_p m_s m_i} \mathrm{d}\omega_p\, \mathrm{d}\omega_s\, \mathrm{d}\omega_i\, \mathrm{e}^{-\mathrm{i}[\omega_p \mathbf{-\omega_s - \omega_i}]t}\, \hat{a}^{(s)\dagger}_{m_s\omega_s} \hat{a}^{(i)\dagger}_{m_i\omega_i}\, S_{m_p m_s m_i}(\omega_p, \omega_s, \omega_i) + H.c. \tag{37}$$

Assuming an initial state consisting solely of vacuum and the pump $[|\Psi_0\rangle = |\ldots, 0, \ldots\rangle \otimes |\Psi_{\mathrm{pump}}\rangle]$, the end state long after the interaction can be written in a first order approximation $[\mathrm{e}^x|_{x\approx 0} = 1 + x + \mathcal{O}(x^2)]$ as follows:

$$\begin{aligned}
|\Psi_{\mathrm{end}}\rangle &= \mathrm{e}^{\frac{1}{\mathrm{i}\hbar}\int_{t_0}^{t} \mathrm{d}t'\, \hat{H}_{\mathrm{NL}\,I}(t')}\ |\Psi_0\rangle \\
&\approx \left[1 + \frac{1}{\mathrm{i}\hbar}\int_{t_0}^{t} \mathrm{d}t'\, \hat{H}_{\mathrm{NL}\,I}(t')\right] |\Psi_0\rangle \\
&= \left[1 + \frac{\mathrm{i}\varepsilon_0}{c_0} \iint_{m_p m_s m_i} \mathrm{d}\omega_p\, \mathrm{d}\omega_s\, \mathrm{d}\omega_i\, \hat{a}^{(s)\dagger}_{m_s\omega_s} \hat{a}^{(i)\dagger}_{m_i\omega_i}\, S_{m_p m_s m_i}(\omega_p, \omega_s, \omega_i)\right. \\
&\qquad\qquad \left. \frac{1}{2\pi}\int_{t_0}^{t} \mathrm{d}t'\, \mathrm{e}^{-\mathrm{i}[\omega_p - \omega_s - \omega_i]t'} + H.c.\right] |\Psi_0\rangle \\
&= |\Psi_0\rangle + \frac{\mathrm{i}\varepsilon_0}{c_0} \iint_{m_p m_s m_i} \mathrm{d}\omega_s\, \mathrm{d}\omega_i\, S_{m_p m_s m_i}(\omega_s + \omega_i, \omega_s, \omega_i) \\
&\qquad\qquad |\ldots, 0, 1^{(s)}_{m_s\omega_s}, 0, \ldots, 0, 1^{(i)}_{m_i\omega_i}, 0, \ldots\rangle \otimes |\Psi_{\mathrm{pump}}\rangle .
\end{aligned} \tag{38}$$

For this it was chosen a t_0 long before the interaction and the equality $\frac{1}{2\pi}\int_{\mathbb{R}} \mathrm{e}^{\mathrm{i}[\omega_s + \omega_i - \omega_p]t}\, \mathrm{d}t = \delta(\omega_s + \omega_i - \omega_p)$ was used. This Kronecker delta expresses the physical concept of energy conservation, i.e. $\omega_p = \omega_s + \omega_i$. For the last equality in (38) the integration over the pump frequency ω_p was evaluated.

Above derivation now is systematically limited to lossless signal and idler modes. For lossy signal and idler modes the problem has to be described with a Green function [18]. Apart from incorporating losses, however, the same assumptions as described above were made. For the form shown in the following the amplitudes of signal and idler photon were assumed to be measured at their respective output in the structure; the amplitude of the pump was specified at it's input. For forward propagating modes the input is at $x = 0$ and the output at $x = L$. For backward propagating modes it is the other way around[8]. In order to distinguish the lossy formulation from the lossless one, a different variable name was chosen for the joint spectral amplitude. For a lossless system nevertheless the results of the lossy formulation are identical to the loss-less formulation.

$$|\Psi_{\mathrm{end}}\rangle = |\Psi_0\rangle + \oint\!\!\!\!\!\!\int_{m_p m_s m_i} \mathrm{d}\omega_s \, \mathrm{d}\omega_i \, \mathrm{JSA}_{m_p\, m_s\, m_i}(\omega_s + \omega_i, \omega_s, \omega_i) \; |\ldots, 0, 1^{(s)}_{m_s\omega_s}, 0, \ldots, 0, 1^{(i)}_{m_i\omega_i}, 0, \ldots\rangle \otimes |\Psi_{\mathrm{pump}}\rangle \; . \tag{39}$$

with the joint spectral amplitude [15]

$$\mathrm{JSA}_{m_p m_s m_i}(\omega_p, \omega_s, \omega_i) = \mathrm{i}\, A^{(p)}_{m_p\omega_p} \frac{1}{c_0} \sqrt{\omega_s \omega_i}\, \boxed{n_{\mathrm{gr}}}_{m_s m_i}(\omega_s, \omega_i)\, \boxed{\mathrm{MO}}_{m_p m_s m_i}(\omega_p, \omega_s, \omega_i) \cdot \boxed{\mathrm{PM}}_{m_p m_s m_i}(\omega_p, \omega_s, \omega_i) \; . \tag{40}$$

The first abbreviation will be called the group index term. It is defined as follows:

$$\boxed{n_{\mathrm{gr}}}_{m_s m_i}(\omega_s, \omega_i) = \sqrt{\left| n^{(s)}_{\mathrm{gr}\, m_s}(\omega_s) \right| \left| n^{(i)}_{\mathrm{gr}\, m_i}(\omega_i) \right|} \; . \tag{41}$$

The second abbreviation will be called the mode overlap term:

$$\boxed{\mathrm{MO}}_{m_p m_s m_i}(\omega_p, \omega_s, \omega_i) = \iiint_{\mathrm{UC}} \mathrm{d}^3 r \, \varepsilon_0 \, \chi_2^{\alpha\beta\gamma}(\vec{r})\, e^{(p)\,\alpha}_{m_p}(\vec{r}, \omega_p)\, e^{(s)\,*\,\beta}_{m_s}(\vec{r}, \omega_s)\, e^{(i)\,*\,\gamma}_{m_i}(\vec{r}, \omega_i)\, \mathrm{e}^{-\mathrm{i}\,\Delta\mathfrak{b}_{m_p m_s m_i} x} \; . \tag{42}$$

As for this expression to be meaningful, the Bloch mode profiles $\vec{e}^{\,(\zeta)}_m(\vec{r}, \omega)$ have to be normalized according to (24) on page 14.

[8] For an actual experiment efficient coupling in and out of the structure would have to be ensured. The effects of coupling in and out of the structure are not taken into account in this thesis.

Lastly the third abbreviation is the phase-matching term. For a forward propagating pump mode it reads:

$$\boxed{\mathrm{PM}}_{m_p m_s m_i}(\omega_p,\omega_s,\omega_i) = \begin{cases} \dfrac{\mathrm{e}^{\mathrm{i}\,\Delta k'_{m_p m_s m_i}(\omega_p,\omega_s,\omega_i)L}\;\mathrm{e}^{-k_{m_p}^{(p)\prime\prime}(\omega_p)L} - \mathrm{e}^{-[k_{m_s}^{(s)\prime\prime}(\omega_s)+k_{m_i}^{(i)\prime\prime}(\omega_i)]L}}{\mathrm{i}\,\Delta k_{m_p m_s m_i}(\omega_p,\omega_s,\omega_i)\,a} & ,\overset{s}{\rightarrow}\overset{i}{\rightarrow} \\ \dfrac{\mathrm{e}^{\mathrm{i}\,\Delta k'_{m_p m_s m_i}(\omega_p,\omega_s,\omega_i)L}\;\mathrm{e}^{-[k_{m_p}^{(p)\prime\prime}(\omega_p)-k_{m_s}^{(s)\prime\prime}(\omega_s)]L} - \mathrm{e}^{-k_{m_i}^{(i)\prime\prime}(\omega_i)L}}{\mathrm{i}\,\Delta k_{m_p m_s m_i}(\omega_p,\omega_s,\omega_i)\,a} & ,\overset{s}{\rightarrow}\overset{i}{\leftarrow} \\ \dfrac{\mathrm{e}^{\mathrm{i}\,\Delta k'_{m_p m_s m_i}(\omega_p,\omega_s,\omega_i)L}\;\mathrm{e}^{-[k_{m_p}^{(p)\prime\prime}(\omega_p)-k_{m_i}^{(i)\prime\prime}(\omega_i)]L} - \mathrm{e}^{-k_{m_s}^{(s)\prime\prime}(\omega_s)L}}{\mathrm{i}\,\Delta k_{m_p m_s m_i}(\omega_p,\omega_s,\omega_i)\,a} & ,\overset{s}{\leftarrow}\overset{i}{\rightarrow} \\ \dfrac{\mathrm{e}^{\mathrm{i}\,\Delta k'_{m_p m_s m_i}(\omega_p,\omega_s,\omega_i)L}\;\mathrm{e}^{-[k_{m_p}^{(p)\prime\prime}(\omega_p)-k_{m_s}^{(s)\prime\prime}(\omega_s)-k_{m_i}^{(i)\prime\prime}(\omega_i)]L} - 1}{\mathrm{i}\,\Delta k_{m_p m_s m_i}(\omega_p,\omega_s,\omega_i)\,a} & ,\overset{s}{\leftarrow}\overset{i}{\leftarrow} \end{cases}. \tag{43}$$

$\overset{s}{\rightarrow}$ denotes a forward propagating signal mode, $\overset{s}{\leftarrow}$ a backward propagating signal mode, $\overset{i}{\rightarrow}$ a forward propagating idler mode and $\overset{i}{\leftarrow}$ a backward propagating idler mode. Single or double primes are used to denote the real or complex value of the respective quantity. The phase-mismatch is defined in exactly the same way as for loss-less modes [see (30) on page 16].

For a backward propagating pump mode the right-hand side [RHS] of (43) has to be multiplied by $[-1]\;\mathrm{e}^{k_{m_p}^{(p)\prime\prime}(\omega_p)\,L}$. In this thesis the pump mode used for the calculation of a JSA is always chosen to be forward propagating, to avoid possible confusion. I want to add that lossy forward propagating modes have a positive imaginary part and lossy backward propagating modes a negative imaginary part in the used convention[9].

The JSA for each created photon pair describes the complex-valued amplitude of their number state. To correctly interpret it, the following facts should be considered. On the one hand one finds that, because of the approximation of the time evolution operator in (38), the final state $|\Psi_{\mathrm{end}}\rangle$ [see (39)] is not normalized. On the other hand the motivation for just that approximation was, that the non-linear efficiency is very weak. This means that, in the same order of accuracy as expected from the used approximation, the squared absolute value of the JSA can still be used for the probability density in terms of signal

[9] Optical media with a weak gain can be described with exactly the same mathematical formalism. In this thesis however only non-active materials without gain were considered.

and idler frequency for the creation of the respective photon pair.

With this result one can now determine the creation probabilities of photon pairs for SPDC using purely linear optic simulations. The fact that the integral in the mode overlap term os over one unit cell only, reduces the computational demands compared to a full simulation. Considering structures with a length of 1000 periods or more, this is quite advantageous. Additionally it is the mode overlap term the only one requiring the actual knowledge of the mode profiles. All other factors in (40) can be determined from quantities obtainable from the band-diagram alone. Furthermore there are quantities totally independent of the bandlets and their modes: the spectrum of the pump and the length of the structure. To study the effect of the latter two quantities one thus only needs to recalculate numerically much less demanding factors.

2.5. Numerical Methods Used for the Calculations of Electromagnetic Fields

For the numerical calculation of the modes two different freely available software packages were used. The first is called MPB and "computes fully-vectorial eigenmodes of Maxwell's equations with periodic boundary conditions by a preconditioned conjugate-gradient minimization of the block Rayleigh quotient in a plane wave basis" [11]. The second one is called MEEP [19] and is a finite-difference time-domain [FDTD] solver [20].
The way to calculate band diagrams and mode profiles with one of these two programs differs quite drastically. MPB is an eigenmode solver, i.e. it directly outputs the eigenmodes of a structure programmed into it; it has however to start at the mode lowest in frequency for one k and consecutively calculate all orthogonal higher modes. This means that above the light-line of the surrounding medium MPB also calculates all its modes and is therefore useless for our purposes above the light-line of the substrate.
MEEP on the other hand is a FDTD solver and thus only able to evolve fields in time. In order to find possible modes of a structure, one can excite it with a source at a non-symmetry point and subsequently observe how the fields propagate. By searching for components with slowly decaying amplitudes and constant frequency at one point in the structure, one can find possible eigenfrequencies ω. This was numerically done with a program called harminv[21, 22]. In order to find the corresponding eigenmodes one then has to narrow-bandedly excite the structure again at the respective position and let the excited field propagate long enough, so that all other than the desired mode decay away.

The method described for finding band diagrams with MEEP is rather time consuming, which is why MPB was used to calculate everything under the light-line of the substrate and MEEP only for the modes above the light-line, where MPB systematically fails.

A short comment on boundaries shall be made here: In MPB the boundaries are always periodic. In MEEP the boundaries in propagation direction were chosen periodic. In the transversal directions absorbers were selected, which made it possible to make the simulation domain smaller, compared to periodic ones. The usual choice of perfectly matched layers [PMLs] was disregarded after some very strange results, because they fail for periodic structures [23].

For the geometric sizes, frequencies and wave vectors not actual physical dimensions were specified in the simulations, but they were normalized with the units stated in Table 2. This was implemented in MPB and MEEP because the Maxwell equations are scale invariant [13]: For the same structure with negligible dispersion scaled up or down in size $[\tilde{\varepsilon}_r(\vec{r},\omega) = \varepsilon_r(s\,\vec{r},\frac{\omega}{s}),\ s \in \mathbb{R}^+]$ the new solution will be the same as for the initial problem at a lower or higher frequency $\tilde{\omega} = \frac{\omega}{s}$, only scaled in its size accordingly $[\tilde{\vec{H}}(\vec{r},\omega) = \vec{H}(s\,\vec{r},\frac{\omega}{s})]$. For this to be a physically useful result, the features of the structure should remain macroscopic.

Table 2: Normalizing factors in the numerical simulations.

geometric lengths	a
frequency $[\nu]$	$\frac{c_0}{a}$
angular frequency $[\omega]$	$\frac{2\pi c_0}{a}$
wave vector $[k]$	$\frac{2\pi}{a}$

One useful equality to relate the normalized results to real physical units is the following:

$$\frac{\omega}{\frac{2\pi c_0}{a}} = \frac{\nu}{\frac{c_0}{a}} = \frac{a}{\lambda_0}\,. \tag{44}$$

This means that the normalized [angular] frequency value relates the physical period a to the free space wavelength λ_0. The bigger the normalized frequency value, the bigger the period will be with respect to the free space wavelength of the light.

Lastly I would like to mention, that above simulations were time-consuming and the bandlets and modes shown in the following sections were therefore only calculated in the necessary precision. To achieve the band diagrams and JSA figures shown in the following sections, I interpolated from the discrete simulation data to the seemingly continuous one.

For this purpose the **spline** function and the **griddedInterpolant** function employing splines provided by MATLAB were used.

2.6. Introduction of Losses

Experimentally in nanostructures small imperfections always exist and thus losses. Numerically these losses were incorporated via a small absorption of the material, because physically these two loss mechanisms show a very similar behavior. This was only possible in MEEP and with above method for finding band diagrams the results had real k and complex ω values, i.e. the modes were spatially perfectly periodic and decayed in time. This however does not correlate to the picture of modes propagating in a slightly lossy structure; there spatially decaying fields that oscillate purely harmonic in time, i.e. modes with complex k and real ω values, are needed. In order to get from one picture to the other the same perturbative approach as in [24] was used, which essentially assumes that the functional relation found for real k and complex ω is valid for the whole complex k and complex ω space and then projects on a different subspace, namely complex k and real ω. A mathematical description can be found in the appendix on page page iii.

For the numerical description the mode profiles were assumed to be unaltered, as the losses the modes suffer over one UC are weak. The total loss of a mode for a structure consisting of several UCs though can be quite big.

3. Linear Optics Design

The aim of the chosen design was to achieve a feature rich dispersion relation and correspondingly the creation of interesting photon pairs. In this section the design process for the chosen design will be presented. In section 3.1 a short motivation for the chosen structure will be given. In section 3.2 the assumed physical properties of the used materials will be stated. After that the effects of different alterations of the investigated system will be explained: in section 3.3 coupling of WGs and in section 3.4 the introduction of periodicity and substrate. Following this the full structure will be designed in section 3.5 with regard to the signal- and idler-modes and in section 3.6 with regard to the pump-mode. Lastly, a summary of the found bands and modes will be given in section 3.7.

3.1. The Chosen Design

Prior to this thesis there existed some designs with the purpose of being able to control the effects of a non-linear optical process, namely second harmonic generation [25, 26]. Those are shown in Fig. 5 (a) and (b). For the experimental realization however some problems arose: Both of them were designed free-standing in air and therefore rather hard to fabricate. The design from [26] additionally had a period of 320 nm, which was too small to reliably fabricate. This originated from the fact that the second harmonic and the fundamental harmonic modes were both designed to be under the light line, so that both modes were lossless. In the design of [25] the period was around 500 nm, the structure however very big and thus prone to mechanical problems. Also the second harmonic mode was above the light-line of air and thus rather lossy.

I now wanted to circumvent these problems of fabricating the structure and having a

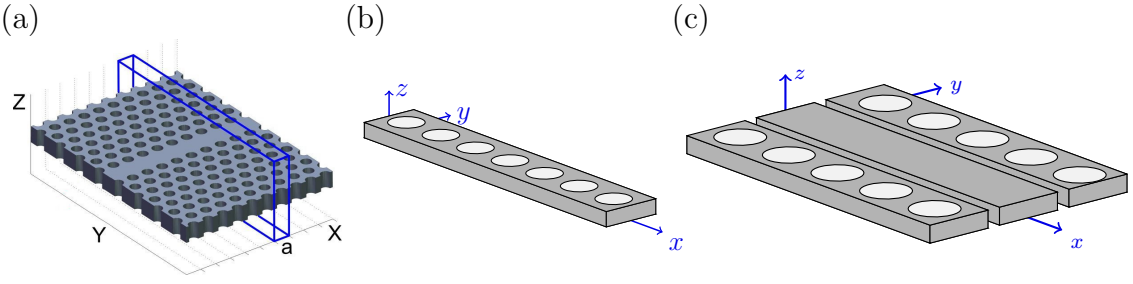

Fig. 5: Schematic view of the investigated structures in: (a) [25], (b) [26] and (c) [7] [shown without substrate].

lossy higher frequency mode with the structure from [7] shown schematically in Fig. 5 (c). The mechanical problems are hopefully avoided by not removing the substrate from under the structure, on which the latter is fabricated. And in order to make the high frequency mode [the pump for SPDC] nearly lossless, I wanted to confine it to the center WG, which does not have any periodic structuring. Thus, the high frequency mode should not be folded in the band-diagram and thus be still under the light line. At the same time the low frequency modes [signal and idler for SPDC] are spatially broader in the transversal directions and were therefore assumed to spread over all three WGs. Accordingly signal and idler will be affected by the periodicity of the structure, which enables one to strongly alter the modes by changing the structure.

3.2. Material Properties

The pump was chosen to be in the range of $\lambda^{(p)} \sim 1500\,\mathrm{nm}$ [telecom-wavelength] and signal and idler correspondingly around $\lambda^{(s)} \sim \lambda^{(i)} \sim 750\,\mathrm{nm}$. The non-linear structure itself was assumed to be made of lithium niobate [$LiNbO_3$] in a z-cut orientation [27], because it shows a quite strong second-order nonlinearity. The substrate was assumed to be made of silica [SiO_2], according to commercially available wafers. Concerning the simulations, the rest of the space was filled with air. The corresponding refractive indices used for the simulations of bands and mode-profiles are shown in Table 3.

Table 3: Optical material properties at the chosen wavelengths.

	signal/idler	pump
λ_0	$1500\,\mathrm{nm}$	$750\,\mathrm{nm}$
n_{air}	1	
$n_{\mathrm{SiO_2}}$ [28]	1.445	1.454
$\hat{n}_{\mathrm{LiNbO_3}}$ [29]	$\begin{pmatrix} 2.213 & 0 & 0 \\ 0 & 2.213 & 0 \\ 0 & 0 & 2.139 \end{pmatrix}$	$\begin{pmatrix} 2.262 & 0 & 0 \\ 0 & 2.262 & 0 \\ 0 & 0 & 2.182 \end{pmatrix}$
$\hat{d}_{\mathrm{LiNbO_3}}$ [8]	$\begin{pmatrix} 0 & 0 & 0 & 0 & 30 & -3 \\ -3 & 3 & 0 & 30 & 0 & 0 \\ -5 & -5 & 30 & 0 & 0 & 0 \end{pmatrix} \mathrm{pm\,V^{-1}}$	

For the sake of completeness the second order susceptibility of z-cut $LiNbO_3$ is mentioned here already, but will not be used prior to section 4. It is related to χ_2 via the

following relations [12]

$$\chi_2^{\alpha\beta\gamma} = 2d^{\alpha\delta} \quad , \tag{45}$$

with the contracted indices

δ	1	2	3	4	5	6
β	1	2	3	2	1	1
γ	1	2	3	3	3	2

·

3.3. Coupling of Waveguides

To get a better understanding of the structure and how to affect its properties, I will start by describing the building blocks of the structure separately. The most simple one is a single rectangular WG, as shown in Fig. 6 (a). In Fig. 6 (b) its lowest bands can be seen. It should be noted that the bands should have as high frequency values as possible, because they are the proportionality factors that relate the size of one period to the free space wavelength of the light [see (44) on page 22] and the smaller one period becomes, the harder it is to fabricate the structure. Then again the pump and idler modes are supposed to be loss-less. That is why they have to be under the light-line of the substrate $\omega = \frac{c_0}{n_{SiO_2}} k$, which will be introduced later on. For $n_{SiO_2} = 1.445$ this means, that at the edge of the 1. BZ the frequency corresponds to $\omega = 0.346$. For periodic modes this will represent the maximum frequency value for them, to be non-leaky. In order to be able to slightly alter the bands later on, a small margin between the light-line and the bands will be kept in this thesis.

Now the bands are folded at the edge of the 1. BZ, i.e. at $k = 0.5\frac{2\pi}{a}$, although no periodicity has been introduced into the structure yet. This originates from MPB, which uses periodic boundaries in all three dimensions and thus always introduces a periodicity. This one will have to keep in mind when interpreting the band-diagrams in Fig. 7 and Fig. 9 as well. Physically this corresponds to Bloch modes with only one non-zero Bloch harmonic.

According to the scale invariance of the Master equation [explained on page 22], the bands can be scaled by changing the lateral sizes of the WG. For a smaller WG the bands will be scaled up, for a bigger WG the bands will be scaled down in the band-diagram.

An excerpt of the real part of the dominant component of the Bloch mode profiles of the modes marked in Fig. 6 (b) can be seen in Fig. 6 (c) and (d). Only the yz-plane is shown, because this is a WG and WG modes have a constant mode profile along the propagation direction of the WG. From the shown slices of the fields it can be seen, that

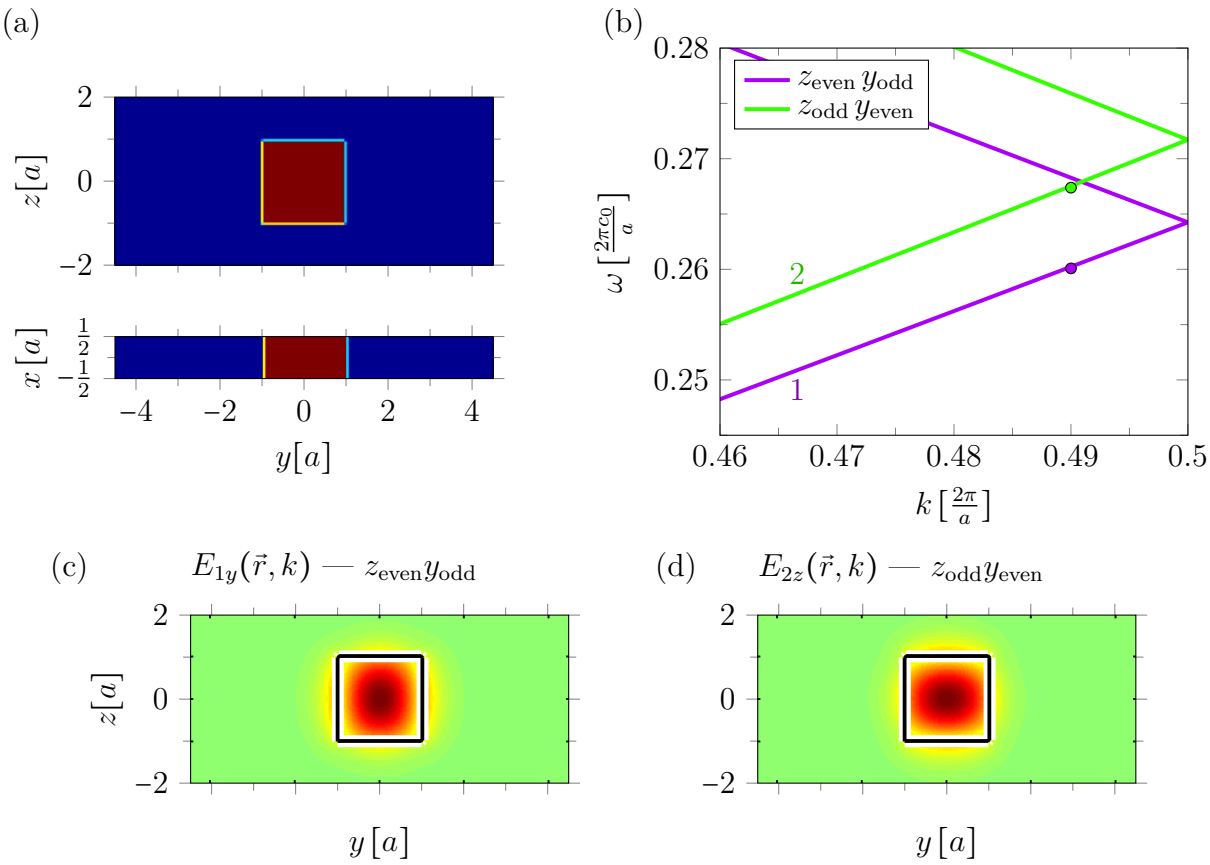

Fig. 6: Epsilon profile [(a)] and band diagram [(b)] for an infinitely long single WG with width and height of $2\,a$. In (c) and (d) the dominant component of the electric field of the Bloch mode profile $\vec{E}(\vec{r},k)$ of the modes marked in (b) can be seen [at $k = 0.49\frac{2\pi}{a}$ and $x = 0$].

along $\vec{e}_y$ and $\vec{e}_z$ these modes behave like simple first order modes.
Regarding the stated symmetries of the modes, I will mention again, that these are with respect to the $E_x(\vec{r},k)$-fields of the modes. This means, that according to the relations stated in Table 1 on page 6, the $E_y(\vec{r},k)$-field of the first mode is even(z) and even(y) and the $E_z(\vec{r},k)$-field of the second mode is even(z) and even(y), which can be seen in Fig. 6 (c) and (d) as well.

Another important point is that the first band has a dominant y-component of the $\vec{E}(\vec{r},k)$-field and the second band a dominant z-component. Just by looking at the shown structure in Fig. 6 (a) one might expect the first two bands to be degenerate. For simplicity it is however displayed a permittivity profile, which was averaged over the different anisotropy components of the epsilon tensor. For the calculations a negative uniaxial, z-cut $LiNbO_3$ crystal was used, which has a smaller refractive index for the E_z

component. This explains why the lowest $\vec{E}_y(\vec{r}, k)$-dominant band has smaller eigenvalues compared to the lowest $\vec{E}_z(\vec{r}, k)$-dominant band. If using a y-cut crystal the dominant components of the first two bands will be exchanged and if using an x-cut crystal the two lowest bands will become degenerate.

For completeness it should be noted that these results differ from the simple Hermite-Gaussian modes of rectangular WGs, because the paraxial approximation is violated by the small lateral extent of the WGs compared to the used wavelength. Accordingly all of the modes are not purely transversal but have a non-negligible longitudinal $E_x(\vec{r}, k)$-field.

In Fig. 7 the simulation results for the coupling of two square, identical waveguides are shown. Again in the excerpt of the band-diagram in Fig. 7 (b) the lowest bands of this band-diagram can be seen. Compared to the single WG band-diagram of Fig. 6 (b) two times as many bands can be seen. This relates qualitatively very well to the findings from the waveguide coupling theory as presented in section 2.3, that for two coupled identical WGs one would find for each band of the single WG two new ones centered around the band of the single one.

To quantitatively relate to these predictions, in Fig. 8 the fully numerical results are compared to the predictions of the WG coupling theory. As expected from an approximative theory for weakly coupled WGs, the predictions of the theory break down for too strong coupling, i.e. too small a distance between the WGs. As can be seen in Fig. 8 the threshold distance for the considered modes is around $d \approx 0.5\,a$.
This makes it obvious that for a correct description of the structure proposed for this thesis, numerical simulations of the full structure can not be avoided. To understand and describe the physics, the theoretical findings are still useful.

The simulation for Fig. 7 was executed at $d = 0.5\,a$, i.e. where the coupling theory still predicted the splitting of the modes quite well. Accordingly the assumption for the coupling theory, that the field profiles of the new modes are superpositions of the single WG modes, can be seen in Fig. 7 (c) to (f). Only in the gap between the waveguides an alteration of the fields is already visible. For the modes that are, with respect to their dominant electric field component, even(y) [Fig. 7 (c) and (e)] the field in the gap is enhanced, for the ones that are odd(y) [Fig. 7 (d) and (f)] it is lessened.

Having the final structure in mind, now the coupling of three waveguides will be investigated. The simulation results are shown in Fig. 9. The number of modes in the same region compared to the single-WG band-diagram has tripled. The shift of the

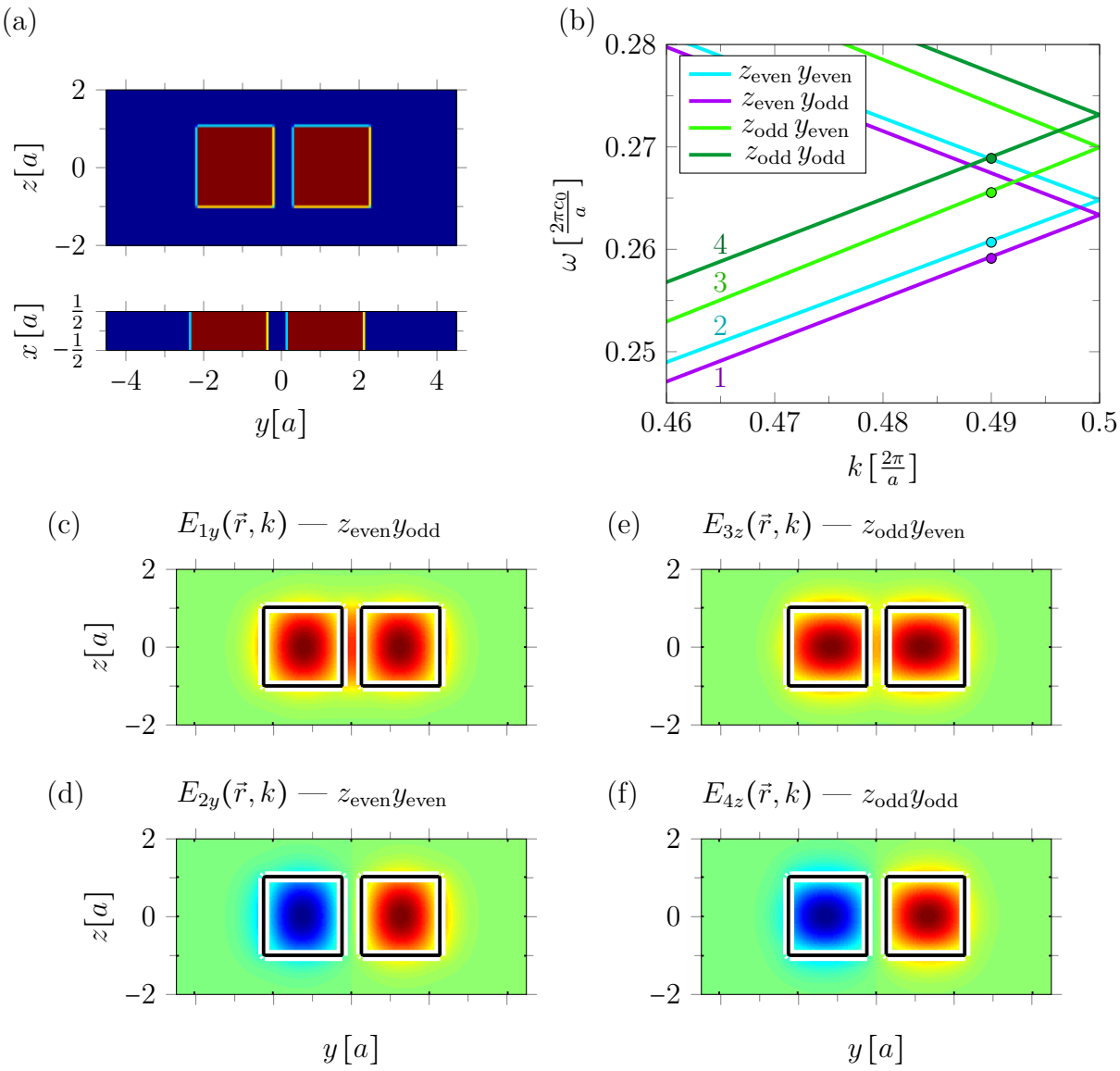

Fig. 7: Epsilon profile [(a)] and band diagram [(b)] for two infinitely long, parallel WGs with width and height of $2\,a$ separated by $0.5\,a$. In (c)–(f) the real part of the dominant component of the electric field of the Bloch mode profiles $\vec{E}(\vec{r},k)$ of the modes marked in (b) can be seen [at $k = 0.49\frac{2\pi}{a}$ and $x = 0$].

bands is noticeably asymmetric and not one of the bands is exactly at the position of the single-WG band. The field profiles are more complicated superpositions of the single-WG modes; because of the opposing z-symmetry, however, the lower three modes are superpositions of the first single-WG mode and the upper three are superpositions of the second single-WG mode only.

By making all of the WGs bigger or smaller one can now scale the bands down or up.

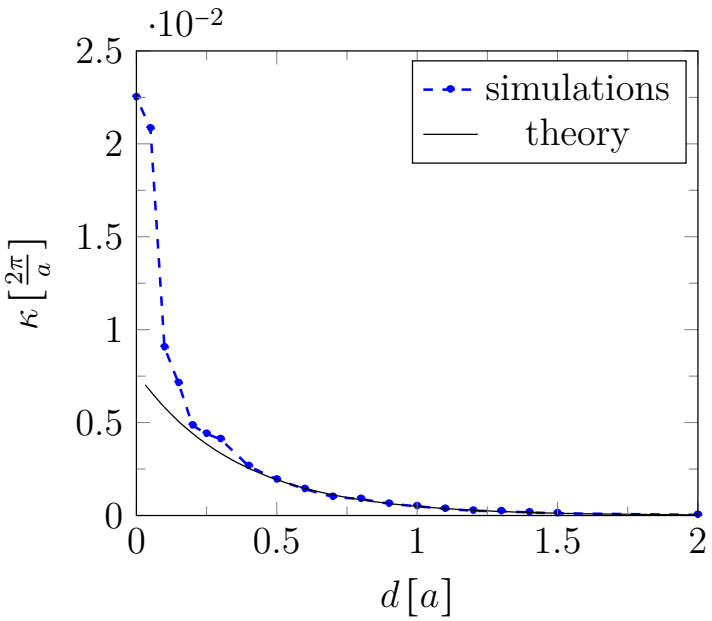

Fig. 8: Dependence of the [averaged] shift of the lowest z-even bands with opposite y-symmetry over the separation of two infinitely long WGs [each with width and height of $2\,a$] around $k \sim 0.49\,\frac{2\pi}{a}$; full numeric simulations - dashed line, results using a simulated mode and the theory of section 2.3 on page 11 - solid line.

And by changing the distance between the WGs one can change the separation of the bands: For an infinitely big distance the bands will become degenerate and be at exactly the same position of the single-WG bands; for a distance going to zero the bands will separate more and more until they are for a distance of $d = 0$ the eigenmodes of a WG of width $3\,a$ and height $1\,a$.

3.4. Periodic Waveguides and Substrate

To allow the interaction of forward and backward propagating modes, i.e. to make the band-folding at the edge of the 1. BZ a physical effect, a periodicity is introduced into the structure. This was achieved by assuming cylindrical holes filled with air in the center of the WG. Some results of the corresponding simulation can be seen in Fig. 10.
Compared to the bands of the unstructured single WG of equal outer dimensions in Fig. 6 (b) on page 27 an overall shift of the bands to higher frequencies can be observed. This can qualitatively be understood by the fact that, if more of the electromagnetic field is concentrated in regions of low refractive index, i.e. in the hole in the structure, then the energy will become higher.

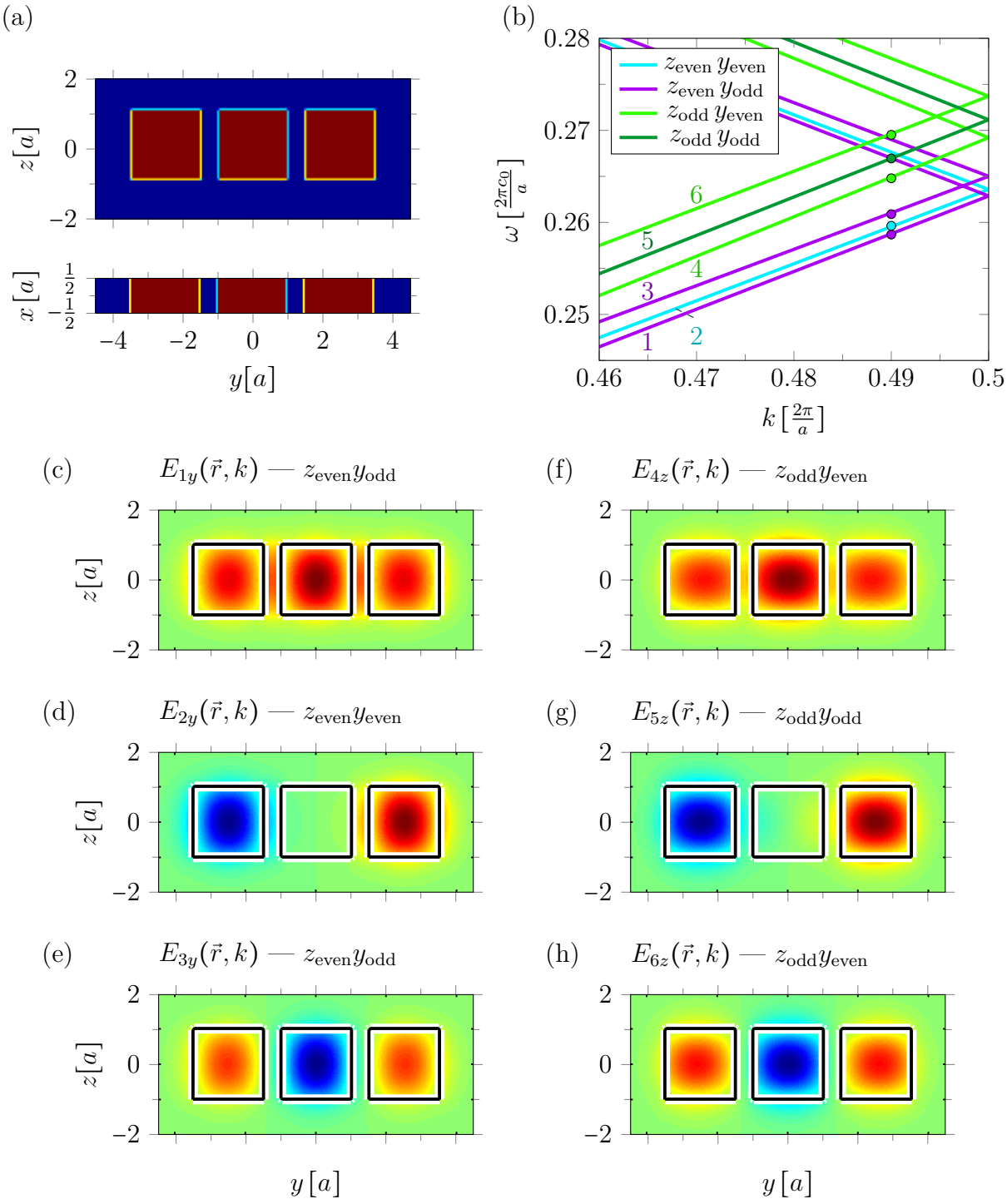

Fig. 9: Averaged epsilon profile [(a)] and band diagram [(b)] for three infinitely long, parallel WGs, each with width and height of $2\,a$. Neighboring WGs are separated by $0.5\,a$. In (c)–(h) the real value of the dominant component of the electric field of the Bloch mode profile $\vec{E}(\vec{r},k)$ of the modes marked in (b) can be seen [at $k = 0.49\frac{2\pi}{a}$ and $z = 0$].

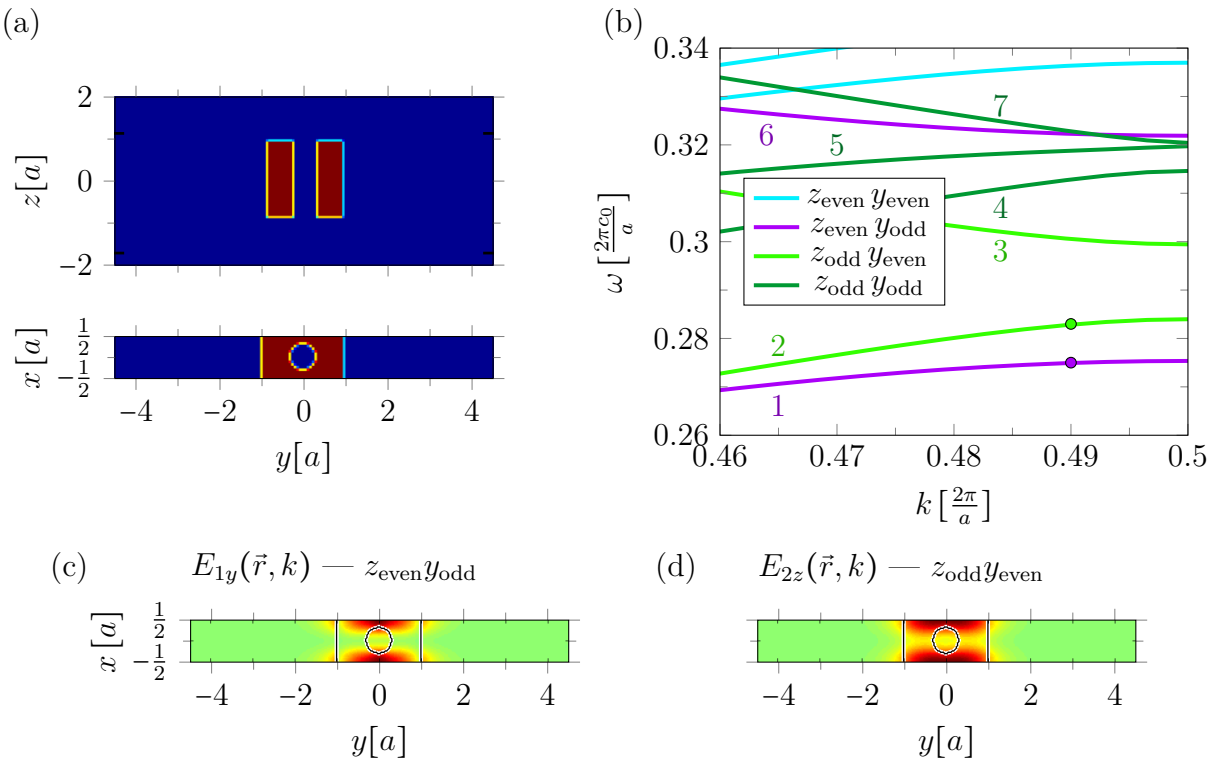

Fig. 10: Epsilon profile [(a)] and band diagram [(b)] for one WG with width and height of $2\,a$ and a cylindrical hole of radius $0.3\,a$ in its center, oriented along $\vec{e}_z$. In (c) and (d) the real part of the dominant component of the electric field of the Bloch mode profile $\vec{E}(\vec{r},k)$ of the modes marked in (b) can be seen [at $k = 0.49\frac{2\pi}{a}$ and $z = 0$].

Additionally, the bands are not straight lines anymore, but become parabolic while approaching the edge of the 1. BZ. This behavior originates from an anti-crossing of the forward propagating modes with their respective backward propagating counterparts. The strength of the anti-crossing, i.e. the size of the frequency gap between the bands, strongly depends on the modes. It is e.g. the frequency separation between bands 1 and 6 approximately three times as big as the one between bands 2 and 3, which again is approximately two times as big as the one between bands 4 and 7.

Having a look at the borderline case of the hole radius approaching 0, it is clear that the band-diagram will have to become the one of the unstructured single WG. So for smaller hole radii the bands will shift downwards in frequency, become less bent while approaching the edge of the 1. BZ and show smaller band gaps. In the opposite borderline case of very big hole radii, the guiding structure will eventually vanish and all bands will shift above the light-line of the surrounding medium — which is why for this thesis only radii smaller or equal to $0.4a$ were considered.

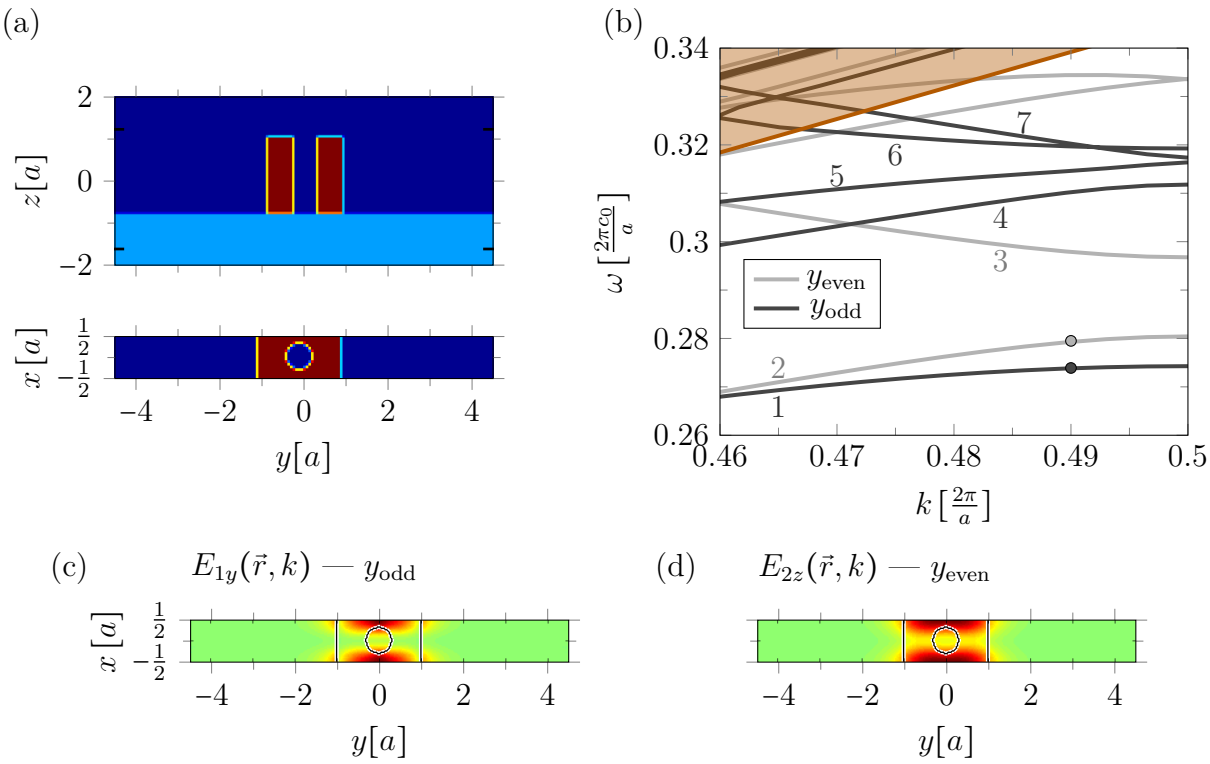

Fig. 11: Epsilon profile [(a)] and band diagram [(b)] for one WG with width and height of $2\,a$ and a cylindrical hole of radius $0.3\,a$ in it's center, oriented along $\vec{e}_z$, on a SiO_2 substrate. The dark orange line in (b) is the light-line of the substrate. In (c) and (d) the real part of the dominant component of the electric field of the Bloch mode profile $\vec{E}(\vec{r},k)$ of the modes marked in (b) can be seen [at $k = 0.49\frac{2\pi}{a}$ and $z = 0$].

The modes shown in Fig. 10 (c) and (d) have the same dominant $\vec{E}(\vec{r},k)$-field components and symmetries as the ones of the unstructured single WG as seen in Fig. 6 (c) and (d). Regarding their actual mode profiles there is one important difference: The Bloch mode profiles are not constant in x anymore, but exhibit a zero-crossing at the center of the holes in their dominant electric field component.

Such a free-standing structure is in an experiment, especially if one wants to use more than only a few periods, fragile. That is why a substrate is introduced under the structure. Some results of the corresponding simulation can be seen in Fig. 11.

Regarding the optical properties of the structure, the substrate has two important effects.
On the one hand it introduces a new light-line, which is lower compared to the light-line of air. This is the reason, why I designed all the previous WGs in way, so that the lowest

bands were around $\omega \sim 0.3\,\frac{2\pi c_0}{a}$ at the edge of the 1. BZ and not around $\omega \sim 0.47\,\frac{2\pi c_0}{a}$, which would have been possible for a structure solely surrounded by media with refractive indices of 1. The corresponding light-line for a SiO_2 substrate can be seen in Fig. 11 (b). In comparison with Fig. 10 (b) one sees that under the new light-line the bands are mostly unchanged, apart from a small shift down in frequency.
On the other hand the substrate breaks the z-symmetry of the structure. This theoretically allows previously orthogonal modes with opposing z-symmetry to couple. In the shown excerpt of the band-diagram this applies to bands 6 and 7; but for those two bands the dominant electric field components are $E_y(\vec{r},\omega)$ and $E_z(\vec{r},\omega)$ respectively, which is why the coupling of the two modes is quite weak and not visible in this band-diagram.

3.5. Coupled Periodic Waveguides on a Substrate

After the optical properties of the single building blocks for the final structure were explained, I am now going to put them together. Two sketches of the structure and the labels used to name the different parameters are shown in Fig. 12.

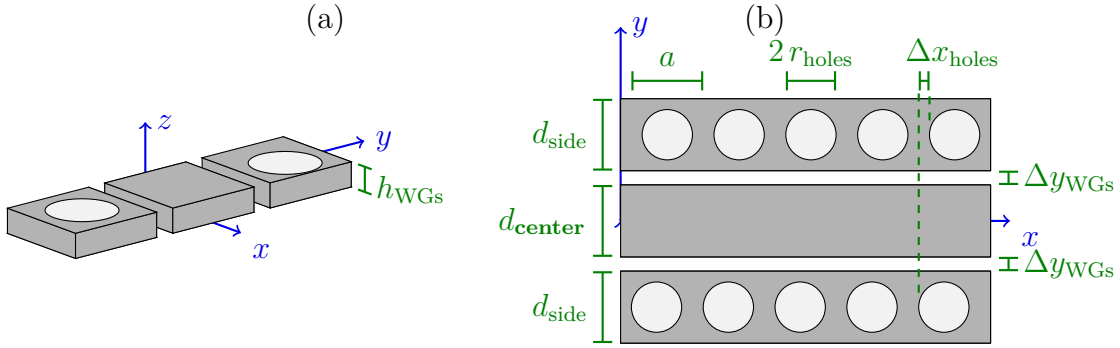

Fig. 12: Schematic view of the structure under investigation [without substrate] with the names used for the different geometric properties of the structure - (a) a projected 3D view of only one unit cell and (b) a sectional view from the top of five unit cells.

To start the design process, the structure shown in Fig. 13 was chosen. It features no visible coupling of the different WGs as of yet, due to the large distance between the WGs. In order to see all of the bands, the degenerate bands 2, 3, 5 and 6 are plotted with dashed lines in Fig. 13 (b).

The bands 1 and 4 in Fig. 13 (b), whose bands resemble a straight line, are mostly confined to the center WG; the remaining ones, i.e. bands 2, 3, 5 and 6, mostly to the outer WGs. Similar to the single WG bands the bands can be scaled up or down in

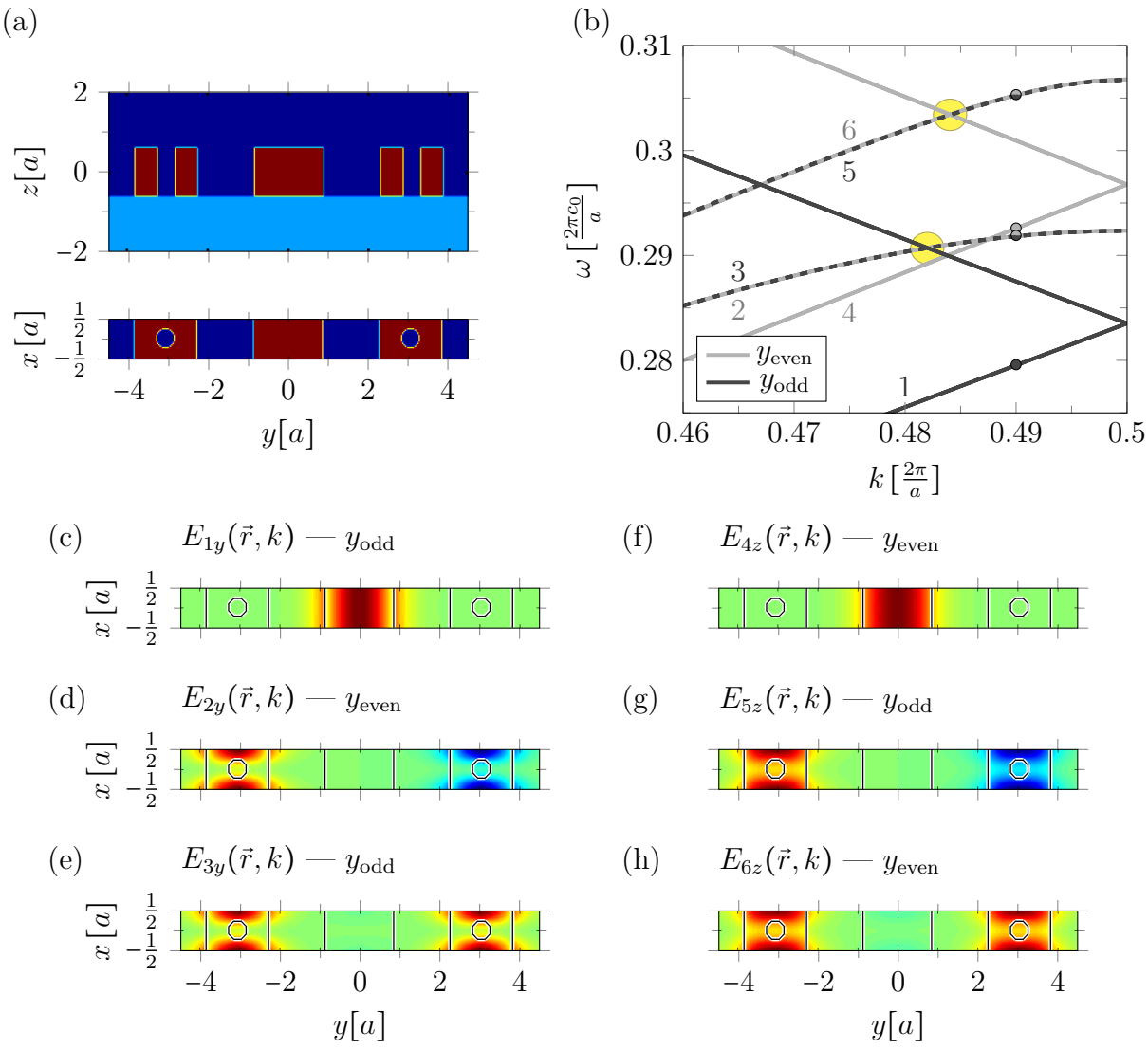

Fig. 13: Averaged epsilon profile [(a)] and band diagram [(b)] for a nearly uncoupled, y-symmetric structure [$d_{\text{center}} = 1.7\,a$, $d_{\text{side}} = 1.55\,a$, $h_{\text{WGs}} = 1.2\,a$, $r_{\text{holes}} = 0.2\,a$, $\Delta x_{\text{holes}} = 0.0\,a$, $\Delta y_{\text{WGs}} = 1.4\,a$]. The big circles in (b) mark, where anti-crossings are expected for stronger coupling. In (c)–(h) the real part of the dominant component of the electric field of the Bloch mode profile $\vec{E}(\vec{r},k)$ of the modes marked in (b) can be seen [at $k = 0.49\frac{2\pi}{a}$ and $z = 0$].

frequency by making the amount of high refractive index material smaller or larger. It can be made larger by making the WGs wider, higher or decreasing the hole radius and smaller vice versa.

In the band diagram a lot of crossings of bands can be seen. The two positions, where measurable band gaps are expected to appear with stronger coupling of the structure, are marked with big yellow circles. At those positions the modes of the same symmetry

will interact, i.e. bands 1 and 3 at the crossing lower in frequency and band 4 and 6 at the crossing higher in frequency. All other crossings won't split noticeably, because the opposing symmetry of the modes prevents an interaction [bands 1 and 2, bands 4 and 3 and bands 4 and 5] or because the mode overlap will be very small because of different dominant field components [bands 2 and 4 and bands 1 and 5]. The symmetry-prohibited anti-crossings are theoretically expected to have a coupling constant equal to zero, while for the crossings of modes with different dominant field components the coupling constants are possibly non-zero but too small to be identifiable.
By breaking the y-symmetry of the structure the modes that now show opposing symmetries can be designed to couple. This means that anti-crossings will appear at the positions marked with yellow circles in Fig. 13 (b). The crossings of modes with different dominant field components will at the same time be nearly unaffected.

As a first step I shifted the WGs closer together. This increased the interaction of the different modes. The band-diagrams corresponding to some of the simulated distances are shown in Fig. 14.

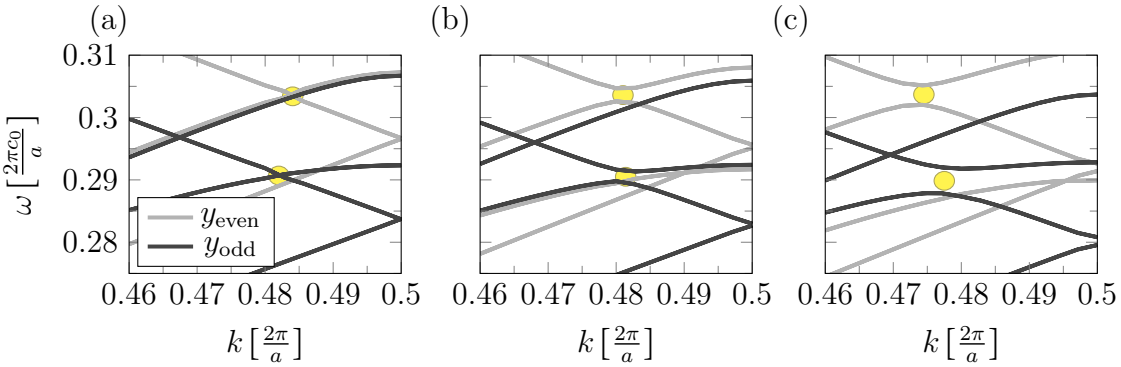

Fig. 14: Band diagrams for the variation of Δy_{WGs}: (a) $0.8\,a$, (b) $0.5\,a$, (c) $0.2\,a$ [$d_{\text{center}} = 1.7\,a$, $d_{\text{side}} = 1.55\,a$, $h_{\text{WGs}} = 1.2\,a$, $r_{\text{holes}} = 0.2\,a$, $\Delta x_{\text{holes}} = 0.0\,a$].

The nearer to each other the WGs are, the stronger the coupling of the bands will be. In going from Fig. 14 (a) to (c) one can make two important observations: The initially degenerate outer-WG bands are shifted more and more apart and anti-crossings appear at the expected positions. As mentioned earlier, these two observations are due to the same physical mechanism - the coupling of modes as explained in section 2.3.

Furthermore, in Fig. 14 (c) the previously straight bands of the initially purely center WG modes are found to bend toward the edge of the 1. BZ. This is a sign of those modes interacting with the periodicity of the outer WGs.

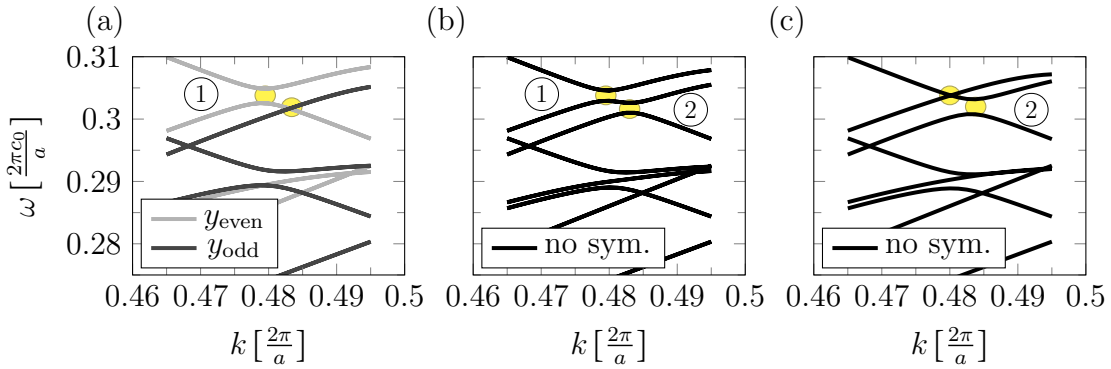

Fig. 15: Band diagrams for the variation of Δx_{holes}: (a) $0.0\,a$, (b) $0.25\,a$, (c) $0.5\,a$ [$d_{\text{center}} = 1.7\,a$, $d_{\text{side}} = 1.55\,a$, $h_{\text{WGs}} = 1.2\,a$, $r_{\text{holes}} = 0.2\,a$, $\Delta y_{\text{WGs}} = 0.4\,a$].

In the following I am going to focus on the shown anti-crossing, which is higher in frequency. That is because I did find a pump mode convenient for coupling to those, as will be shown in section 3.6 on page 39. The three bands that are nearest to said anti-crossing will be chosen for the signal and idler modes.

In order to couple the bands of opposing y-symmetry, the y-symmetry of above structure was broken. This was done by displacing the row of holes in one of the outer waveguides along $\vec{e}_x$, i.e. by varying Δx_{holes}. Some of the band-diagrams of the corresponding simulations can be seen in Fig. 15. The values considered range from no displacement to $\Delta x_{\text{holes}} = 0.5\,a$ only, because the bands for $\Delta x_{\text{holes}} = [0.5 + \tilde{x}]\,a$ are the same as for $\Delta x_{\text{holes}} = [0.5 - \tilde{x}]\,a$ with $\tilde{x} \in \mathbb{R}$. Additionally the bands are periodic in a.

Fig. 15 (a) still incorporates the y-symmetry and is quite similar to the band-diagrams shown in Fig. 14. The only difference is, that in order to minimize fabrication errors I wanted to have a reasonable thickness to width ratio, which is why $\Delta y_{\text{WGs}} = 0.4\,a$ was chosen.
For Fig. 15 (b) it was $\Delta x_{\text{holes}} = 0.25\,a$. This means that the y-symmetry of the structure is broken. Accordingly a coupling of the bands at the previously symmetry-prohibited crossings can be observed, most importantly at (2). At the same time the band gap at the anti-crossing (1) is weaker. Other than at the positions of coupling the bands are unchanged in their course and position.

The band-diagram for $\Delta x_{\text{holes}} = 0.5\,a$ can be seen in Fig. 15 (c). Here one sees that the band gap at anti-crossing (1) disappeared and the one for anti-crossing (2) is maximal. This can be explained by the fact, that for $\Delta x_{\text{holes}} = 0.5\,a$ the structure has a symmetry again: a glide reflection symmetry. This means that by mirroring the structure from the

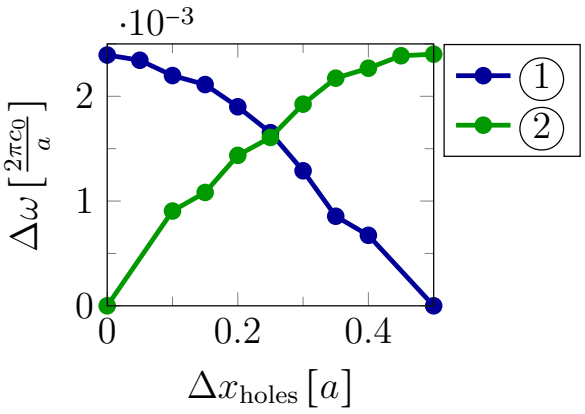

Fig. 16: Frequency gaps of the anti-crossings of the upper three bands shown in Fig. 15 with a read-out error of $0.3 \cdot 10^{-3}\frac{2\pi c_0}{a}$ as a function of the variation of the shift of one row of holes Δx_{holes}.

positive-x half-space on the yz-plane at $x = 0$ and then shifting it by $0.5\,a$ along $\vec{e}_x$, we get the full structure again[10]. This symmetry could neither be specified with MPB nor MEEP, which is why for the numerical simulations no symmetry was specified explicitly. The apparent mirror symmetry of the problem in $\vec{e}_x$ is broken by the periodic boundary conditions along $\vec{e}_x$ for all $k \neq n \cdot 0.5\,\frac{2\pi}{a}$ with $n \in \mathbb{Z}$.
For a quantitative picture the band gaps of the anti-crossings as labeled with (1) and (2) in Fig. 15 are shown as a function of Δx_{holes} in Fig. 16 for all numerically calculated values of Δx_{holes}. Here one can see the previously mentioned fact, that for $\Delta x_{\text{holes}} = 0$ or $0.5\,a$ the respective band gaps really are maximal. I want to note that this dependence of the size of the band-gaps is strongly mode-dependent and therefore has to be numerically calculated individually for each structure and each set of modes that do anti-cross.

In order to maximize the interaction of the different bands, it was chosen $\Delta x_{\text{holes}} = 0.25\,a$. All geometric parameters for the designed structure are recapped in Table 4. The interesting mode profiles and a band diagram zoomed to the interesting region for the signal and idler bands can be found in section 3.7 on page 40. Before that I will now show the pump bands in the next subsection.

Table 4: Geometric properties of the designed structure [in units of the period a].

a	d_{center}	d_{side}	h_{WGs}	r_{holes}	Δx_{holes}	Δy_{WGs}
1.0	1.7	1.55	1.2	0.2	0.25	0.4

[10] Mathematicall this is represented by the frieze group p11g [30].

3.6. The Pump Mode

Up till now all simulations were done with MPB. The pump however lies above the light-line, which is why I had to use MEEP.

The interesting frequency and wavevector region for the simulation was determined from the energy-conservation and phase-matching conditions for SPDC. Energy-conservation requires the sum of the frequencies of signal and idler to be equal to the frequency of the pump, i.e. $\omega_p = \omega_s + \omega_i$. The phase-matching condition requires the absolute value of the real part of the difference of the wavevector of the pump and the sum of the wavevector of signal and idler to be zero, i.e. $\mathrm{Re}\left(\Delta k_{m_p m_s m_i}\right) = 0$ [compare (30) on page 16]. As can be seen in Fig. 15 (b), signal and idler have a frequency around $0.3\,\frac{2\pi c_0}{a}$ and accordingly the pump has to be around a frequency of $0.6\,\frac{2\pi c_0}{a}$. And the wavenumbers of signal and idler are around $0.48\,\frac{2\pi}{a}$, which is why the pump should be around $0.96\,\frac{2\pi}{a}$. In the 1. BZ this corresponds to $k = -0.04\,\frac{2\pi}{a}$. Because the band diagrams are symmetric in k, I chose to calculate the bands in the positive half of the 1. BZ.

The bands calculated for the final structure as specified in Table 4 are shown in Fig. 17. These are not all possible bands of the structure, but the ones that are mainly confined to the center WG and were excited with an $E_z(\vec{r},\omega)$ point-source with Gaussian temporal profile positioned at a non-symmetry point inside the center WG.

One sees that the modes of bands named 1 and 2 in Fig. 17 (b) show two lobes in the vertical direction [i.e. along $\vec{e}_z$] in their dominant electric field component. This will lead to a very small mode overlap term $\boxed{\mathrm{MO}}_{m_p m_s m_i}(\omega_p,\omega_s,\omega_i)$ with any two of the modes, chosen in the previous chapter, which were all one-lobed in the vertical direction. For the modes of band 2 the fact that its modes are $E_y(\vec{r},\omega)$-dominant will additionally lead to an even smaller mode overlap term.

The mode of band 3 shown in Fig. 17 (e) in contrast is one-lobed in the vertical direction and three-lobed in the horizontal direction [i.e. along $\vec{e}_y$] in its dominant electric field component, which is $E_z(\vec{r},\omega)$. That is why the modes of bands 3 promise a stronger mode overlap with the previously chosen signal and idler modes and my reason to focus solely on band 3 for the pump mode in the following calculations.
From the mode profile in Fig. 17 (e) one can see now, that the mode is confined to the center WG. The same holds for every other simulated mode of this band. This confinement is also represented by the decay length L_{decay} of theses modes, which is calculated by $L_{\mathrm{decay}} = \frac{1}{\mathrm{Im}(k)}$ and represents the distance, over which the intensity of the mode decays by e^{-2}. For all simulated modes of band 3 the decay length was in the

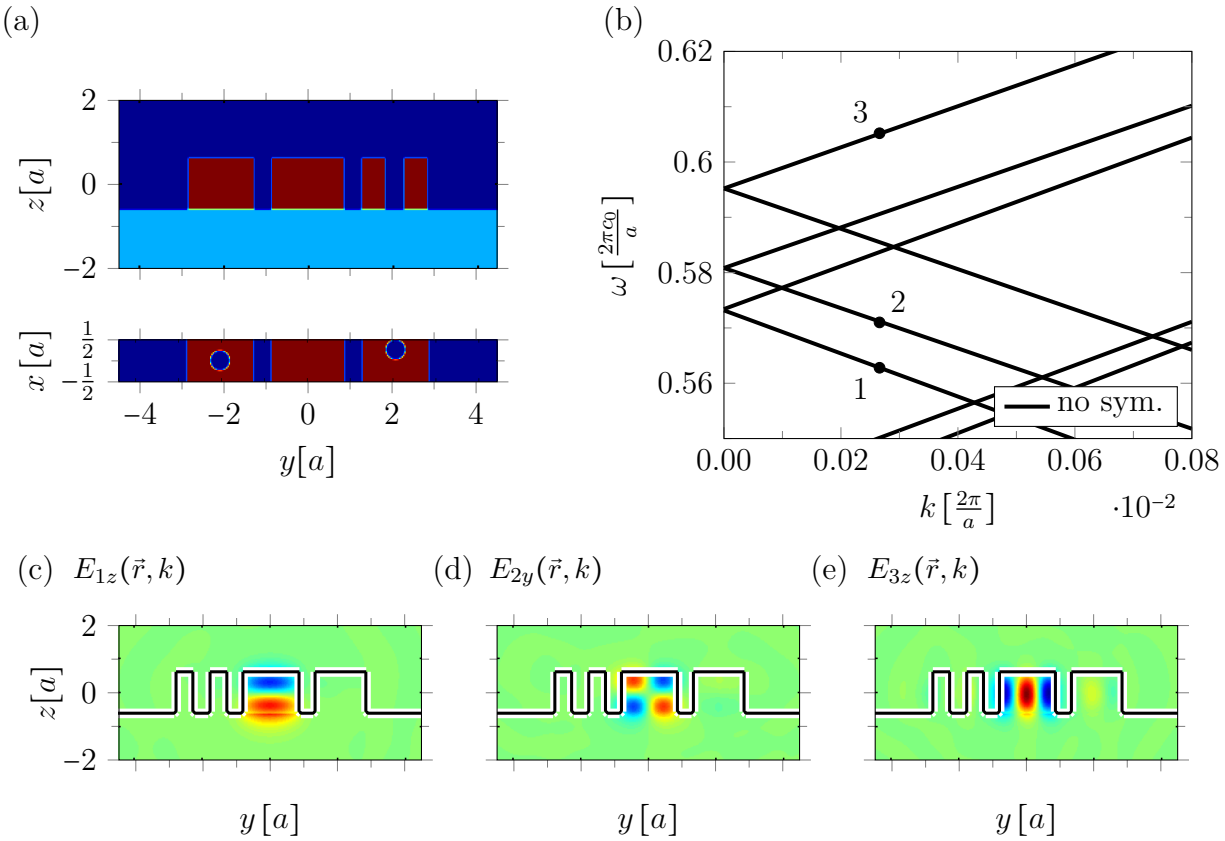

Fig. 17: Epsilon profile [(a)] and E_z-excited band diagram [(b)] for the designed structure [$d_{\text{center}} = 1.7\,a$, $d_{\text{side}} = 1.55\,a$, $h_{\text{WGs}} = 1.2\,a$, $r_{\text{holes}} = 0.2\,a$, $\Delta x_{\text{holes}} = 0.25\,a$, $\Delta y_{\text{WGs}} = 0.4\,a$]. In (c)–(e) the real part of the dominant component of the electric field of the Bloch mode profile $\vec{E}(\vec{r},k)$ of the modes marked in (b) can be seen [at $x = 0$ and $k = 0.47\frac{2\pi}{a}$].

order of 10^3. Also the bands are linear in the whole band diagram, which also indicates that the interaction of the modes of band 3 with the periodicity of the outer WGs is negligible. Correspondingly the pump modes were found to be a Bloch mode with only one noteworthy Bloch harmonic, as intended. The dominant Bloch harmonic for the forward propagating pump mode is the one with $\mathfrak{b}^{(p)} = 1$.

3.7. Pump and Signal/Idler Modes Combined

To summarize the found linear optical properties of the designed structure, the selected bands of signal, idler and pump and some mode profiles are shown in Fig. 18.

In order to get a visual impression where phase-matching and energy-conservation for

SPDC are possible, the pump band is folded down to the interesting region in the 1. BZ via:

$$\omega = \frac{1}{2}\tilde{\omega} \qquad , \qquad k = \frac{1}{2}\left[-\tilde{k} + \frac{2\pi}{a}\right] , \tag{46}$$

with $\tilde{\omega}$ and $\tilde{k}$ the numerical results from the positive half of the 1. BZ $[\frac{\pi}{a} \geq \tilde{k} \geq 0]$.
Now to visually determine possible phase-matched modes for SPDC, one has to look at the band-diagram showing the real parts of the bandlets. There one has to select two signal and idler modes, i.e. two points on the signal and idler bandlets. These one has to connect with a straight line. On this line one then needs to find the point in the center between the points of the selected signal and idler modes. If this point lies on the down-folded bandlet of the pump, then one will have found a phase-matched triple of modes. By doing so in the full 1. BZ all Bloch harmonics are considered.
For the special case that the two signal and idler modes are identical, the point in the center of the line connecting those two is the same point. Visually this corresponds to a crossing of the pump bandlet with a signal and idler bandlet.

In the band diagram one sees three points, where the down-folded pump bandlet crosses signal and idler bandlets, i.e. three points of phase-matching. In addition to these there exist a lot more possible phase-matching points in this band diagram, which are not so obvious. All possibilities for this structure will be shown in the next section.

From the mode profiles of the signal- and idler-modes one can see that they change quite drastically along one band at the region of the anti-crossings. Away from the anti-crossings the mode profiles change much less. Considering how this band-diagram was designed, similarities can be seen in the field profiles of Fig. 18 (a), (d) and (h), of Fig. 18 (b), (f) and (i) and of Fig. 18 (c), (e) and (g), i.e. along the bands of the uncoupled structure. Along the unchanged regions of the bands the mode profiles are similar to the uncoupled modes. Only directly at the anti-crossings the fields are changed continuously from the mode profile of the one band to the mode profile of the other band that coupled.

As the pump mode is mainly confined to the unstructured center WG, it is nearly unchanged in its mode profile along the course of one band in the depicted region.

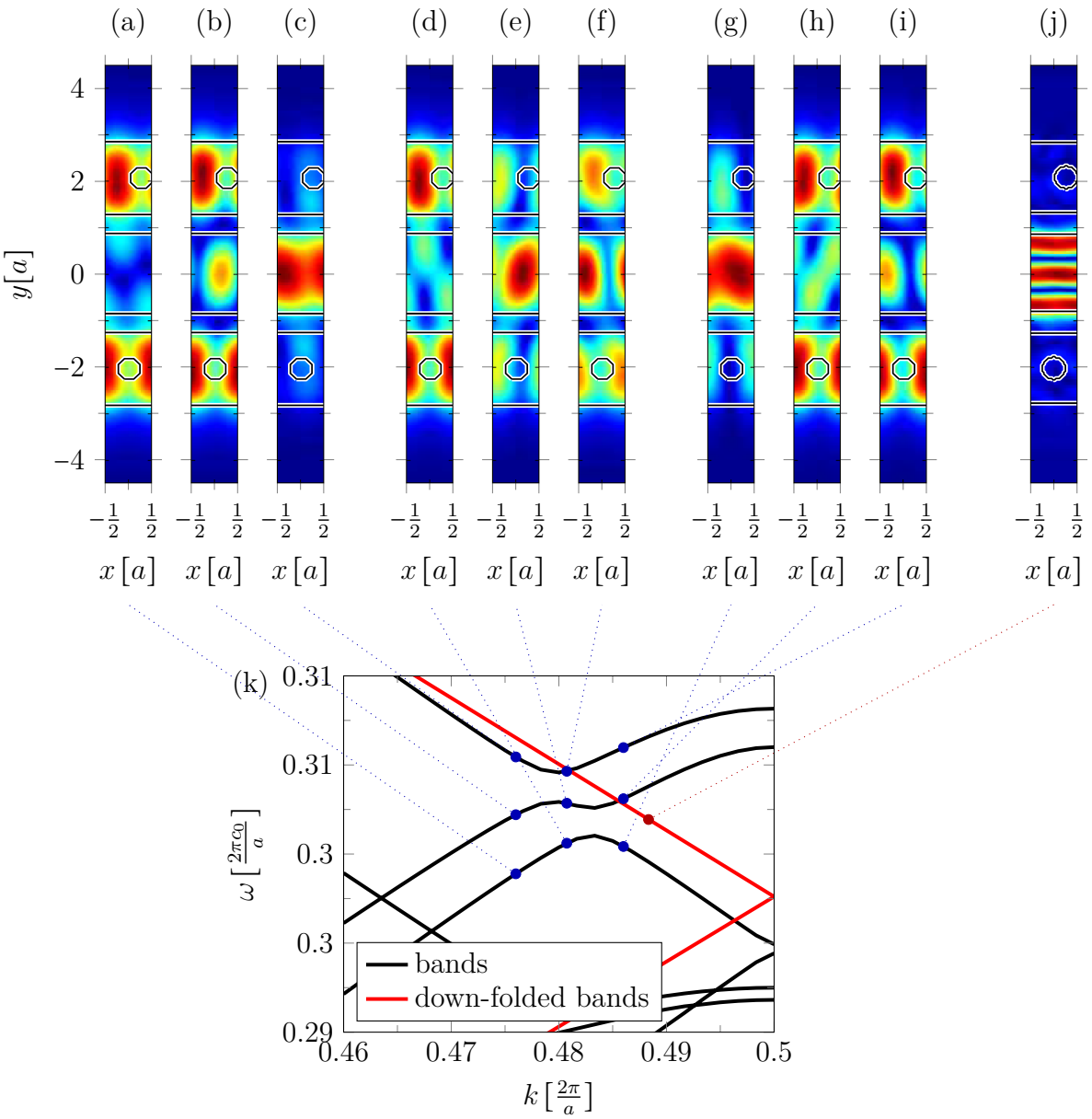

Fig. 18: The absolute values of the z-component of the electric field of the Bloch mode profile $|E_z(\vec{r}, k)|$ are shown at $z = 0$ for the modes of the designed structure [$d_{\text{center}} = 1.7\,a$, $d_{\text{side}} = 1.55\,a$, $h_{\text{WGs}} = 1.2\,a$, $r_{\text{holes}} = 0.2\,a$, $\Delta x_{\text{holes}} = 0.25\,a$, $\Delta y_{\text{WGs}} = 0.4\,a$]: (a)–(i) for signal-/idler-modes and (j) for the chosen pump mode. In (k) the corresponding band diagram is shown, where the bands of the pump are down-folded to the region of signal and idler.

4. SPDC in Lossy Coupled Structured Waveguides

Every fabricated structure has imperfections. This introduces losses into the modes of the perfect structure. In this section the results of the lossy JSA-calculations will be given. In section 4.1 the lossy bandlets and the corresponding group indices are shown. In section 4.2 all of the interesting parts of the JSA for one bandlet combination are shown exemplarily. Following that the summed squared absolute values of the JSA for all considered bandlets are given in section 4.3.
Lastly the effects of different lengths of the structure [section 4.4] and an artificially induced shift of the pump-bandlet relative to the signal- and idler-bandlets [section 4.5] are investigated.

4.1. Lossy Modes of the Designed Structure

In order to incorporate losses, I calculated the signal- and idler-modes again with MEEP and specified additionally $\mathrm{Im}(\varepsilon_r) = 0.001$ at the center frequency of the source of the respective simulation. The resulting imaginary frequency components varied by $\pm 10\,\%$ around $-2.6 \times 10^{-5}\,\frac{2\pi c_0}{a}$, after erroneous outlying points had been removed. For simplicity an averaged value was chosen for the imaginary frequency component of all signal and idler modes.

In Fig. 18 (k) on page 42 one sees that the down-folded pump bandlet nearest to the region of interest has a negative slope, which means that the pump is backward propagating. To have a forward propagating pump mode the bands on the negative side of the 1. BZ were calculated. These could be easily derived from the bands in the positive half of the 1. BZ via $\omega(-k) = \omega(k)$.
It was determined in the end of section 3.6, that the forward propagating pump mode consists mainly of one Bloch harmonic with $k \sim 1\frac{2\pi}{a}$ around $\omega \sim 0.6\frac{2\pi c_0}{a}$. For an efficient coupling signal and idler modes with dominant Bloch harmonics with $k \sim 0.5\frac{2\pi}{a}$ for $\omega \sim 0.3\frac{2\pi c_0}{a}$ thus are beneficial. To emphasize this fact I chose to show the bands in the positive 2. BZ in Fig. 19 (a).

For the numerical calculations I also considered the bandlets in the positive half of the 1. BZ, as shown in Fig. 18 on page 42. The effect of this on the resulting JSA proved rather small, as can be expected from the visible phase-mismatch of the forward propagating pump to those bandlets. That is why I won't mention those bandlets explicitly in this

section.

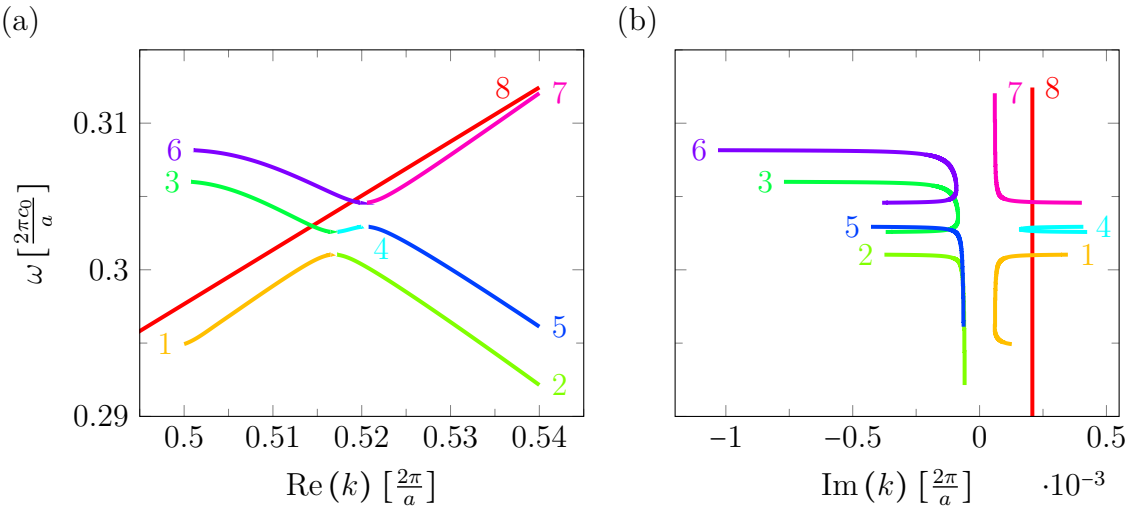

Fig. 19: Perturbatively calculated lossy pump- [8] and signal-/idler-bandlets [1–7] of the designed structure [$d_{\mathrm{center}} = 1.7\,a$, $d_{\mathrm{side}} = 1.55\,a$, $h_{\mathrm{WGs}} = 1.2\,a$, $r_{\mathrm{holes}} = 0.2\,a$, $\Delta x_{\mathrm{holes}} = 0.25\,a$, $\Delta y_{\mathrm{WGs}} = 0.4\,a$] considered for the JSA-calculations.

The color-scheme of the previous section was abandoned and the bands were divided into bandlets. For the rest of this section the bandlets will be referred to with the numbers given in Fig. 19.

Considering that slow-light enhances the interaction of the modes with the material not only for non-linear optical processes, but also for losses, it can be understood that the absolute value of the imaginary part of k becomes much bigger when approaching an anti-crossing. The bandlets with positive imaginary k values correspond to lossy forward propagating modes $\vec{E}(\vec{r},t)$ and vice versa, as can be seen from the chosen representation for the Fourier components with $\vec{E}(\vec{r},t) \propto \mathrm{Re}\left(\mathrm{e}^{\mathrm{i}[kx-\omega t]}\right)$. In this thesis no gain was considered, which is why all bandlets in Fig. 19 are lossy along their respective propagation direction.

At slow-light regions the losses become very big. The group indices, which for anti-crossings of lossless modes diverge, at the same time do not diverge anymore for lossy modes at the anti-crossings. This will be shown exemplarily later on. Hence the contribution to the final JSA from the regions right at the anti-crossing was neglected: For the finding of the lossy bandlets I did not extrapolate from the frequency range of the lossless bandlets. Visually this can be seen in Fig. 19 (a) and (b), where the bandlets stop abruptly near the anti-crossings.

In all other respects the bandlets are similar to the non-lossy results of figure Fig. 18 (k)

on page 42.

In Fig. 20 the absolute values of the group indices are shown. To be able to visually distinguish the different group indices better, the ones of forward propagating modes are shown on the positive side and the ones for backward propagating modes on the negative side. This is achieved by multiplying the absolute value with the sign of the real part. In order to make this plot more relatable to the previous plots, the group index $n_{\mathrm{gr}_i}(k_i(\omega))$ was plotted along the abscissa and the frequency along the ordinate.

The group index of the pump $n_{\mathrm{gr}_8}(\omega)$ has a nearly constant value over the considered frequency range. The signal- and idler-group indices do, like the imaginary part of the k-values, get bigger when reaching the anti-crossings. Here one sees now that the group indices don't become infinitely large at the anti-crossings, but show local extrema. Because these extrema are rather hard to see in the full picture of Fig. 20 (a), a smaller excerpt is shown in Fig. 20 (b). Here only two extrema are shown; every other group index bandlet also reaches a maximum at an anti-crossing. This means, as a result of the arbitrarily chosen material losses of $\mathrm{Im}\,(\varepsilon_r) = 0.001$ the absolute values of the group indices are smaller than 25 for all considered bandlets.

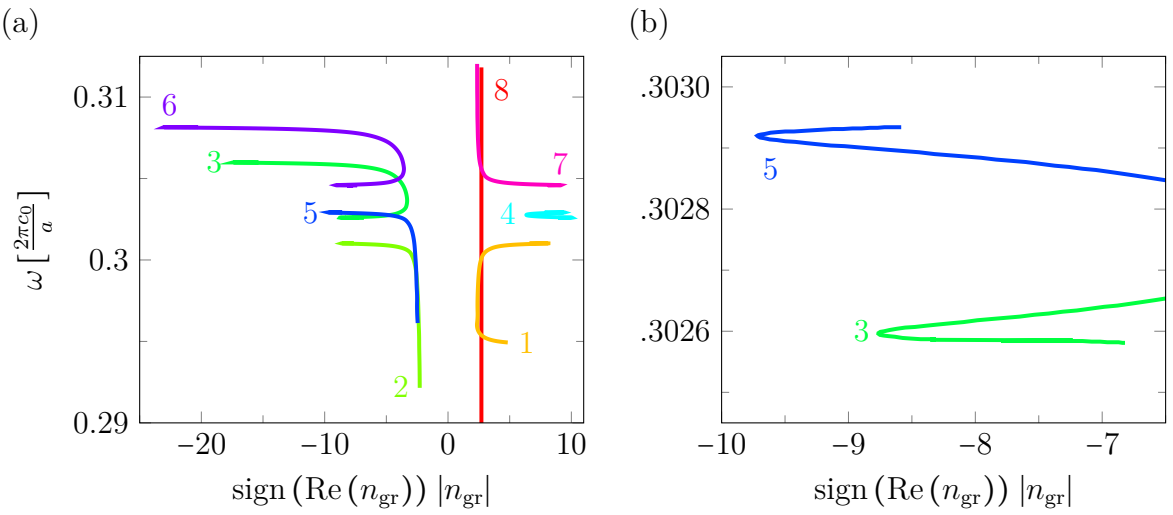

Fig. 20: Perturbatively calculated lossy pump- [8] and signal-/idler-group indices [1–7] for the modes of the designed structure [$d_{\mathrm{center}} = 1.7\,a$, $d_{\mathrm{side}} = 1.55\,a$, $h_{\mathrm{WGs}} = 1.2\,a$, $r_{\mathrm{holes}} = 0.2\,a$, $\Delta x_{\mathrm{holes}} = 0.25\,a$, $\Delta y_{\mathrm{WGs}} = 0.4\,a$] considered for the JSA-calculations — (a) the full calculated picture and (b) zoomed into an interesting region. In order to show the pump in the same region as signal and idler its frequency values were divided by two.

Lastly I want to mention that Fig. 20 (a) and Fig. 19 (b) look quite similar. Unlike the lossy group indices the imaginary parts of k don't show any sign of local extreme at the positions of the anti-crossings in the depicted region.

4.2. Exemplary Depiction of Interesting Parts of the Joint Spectral Amplitude

For the calculation of the JSA the number of unit cells along $\vec{e}_x$ had to be fixed. As a first approach a length of 100 periods was used, which corresponds to a real space length of approximately 45 µm[11].

Exemplarily the interesting parts of the $\mathrm{JSA}_{8\,3\,2}$ with bandlet 8 as a pump, bandlet 3 as signal and bandlet 2 as idler are given in Fig. 21. The parts of the full JSA for these two bandlets that are not shown here, are: First the pump amplitude $A^{(p)}_{8\,\omega_3+\omega_2}$, which was set to 1 for all frequencies, in order to see the full range of effects originating from the other terms; for experiments the frequency profile of the pump will have to be considered additionally to the shown JSAs. And secondly the $\sqrt{\omega_s\omega_i}$-term, which simply corresponds to a tilted plane in terms of (ω_s, ω_i).

The absolute value of the group index term $\boxed{n_{\mathrm{gr}}}_{3\,2}$ in Fig. 21 (a) is, as can be expected from the functions shown in Fig. 20, strongest in the upper right corner [for high signal and idler frequencies]. Because of the very steep rise of the group indices at the anti-crossings, $\left|\boxed{n_{\mathrm{gr}}}_{3\,2}\right|$ becomes much smaller very strongly if one moves away from there. Over most of the shown region $\left|\boxed{n_{\mathrm{gr}}}_{3\,2}\right|$ is nearly constant and approximately 25 times smaller than at its maximum. This maximum is lying at the most upward and rightmost position shown in Fig. 21 (a) because, as mentioned in the previous subsection, the bandlets were not extrapolated outside of the frequency regions of the respective loss-less bandlets. Would I have been able to correctly calculate the lossy bands further, I expect to have found $\left|\boxed{n_{\mathrm{gr}}}_{3\,2}\right|$ to become smaller again [31, 32], as hinted at in Fig. 20 (b).

The absolute value of the phase-matching term $\boxed{\mathrm{PM}}_{8\,3\,2}$ is shown in Fig. 21 (b). The white line marks the positions of phase-matching, i.e. $\mathrm{Re}\left(\Delta k_{832}(\omega_3+\omega_2, \omega_3, \omega_2)\right) = 0$. Theory predicts a result of the form $N\,\mathrm{sinc}\left(\Delta k_{832}(\omega_3+\omega_2, \omega_3, \omega_2)\frac{L}{2}\right)$ for a loss-less case [see (33) on page 17]. Its maximum is N for $\Delta k_{832}(\omega_3+\omega_2, \omega_3, \omega_2) = 0$. $\left|\boxed{\mathrm{PM}}_{8\,3\,2}\right|$ is maximal at perfect phase-matching and the global maximum in this plot is approximately

[11] From (44) on page 22 it follows with $\omega \sim 0.3\frac{2\pi c_0}{a}$ and $\lambda = 1500\,\mathrm{nm}$ that $a \sim 450\,\mathrm{nm}$.

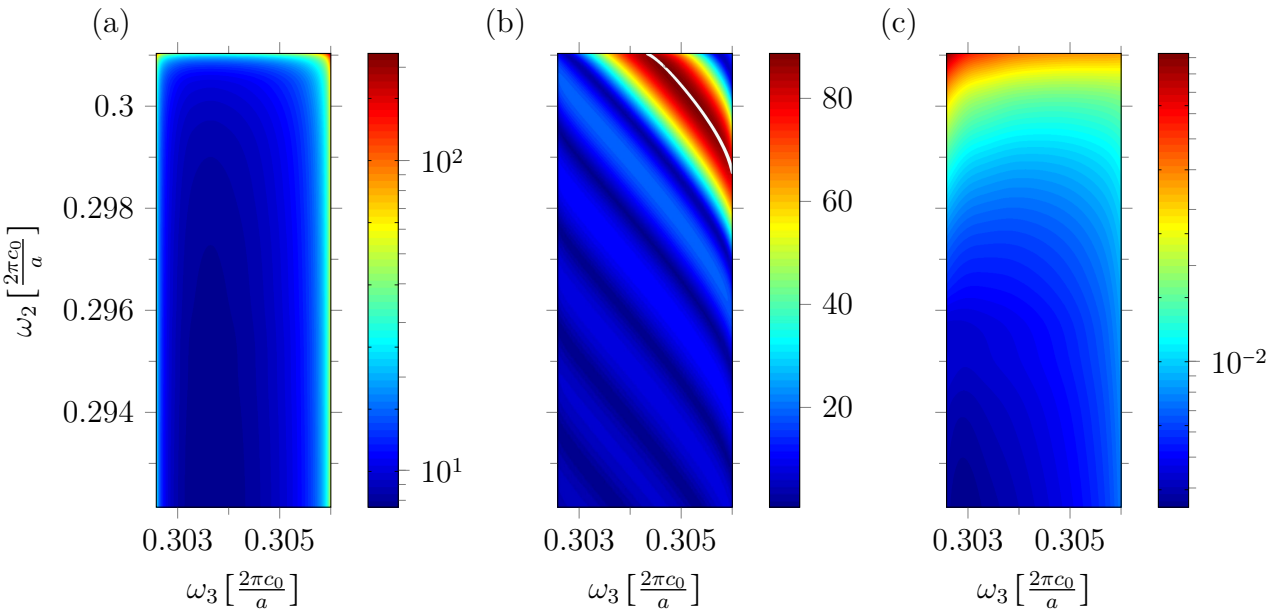

Fig. 21: (a) $\left|\boxed{n_{\mathrm{gr}}}_{32}\right|$, (b) $\left|\boxed{\mathrm{PM}}_{832}\right|$ and (c) $\left|\boxed{\mathrm{MO}}_{832}\right|$ for the lossy bandlets as labeled in Fig. 19 on page 44. (a) and (c) are shown with a logarithmic color-scale.

at 89. Comparing this to the number of periods in the simulation of $N = 100$ a noticeable difference to the loss-less case can be observed. Apart from this overall damping the graph shows, as in the loss-less case, a sinc-like behavior.

The absolute value of the mode overlap term $\boxed{\mathrm{MO}}_{832}$ in Fig. 21 (c) is maximal for small ω_3 and big ω_2. If one looks at Fig. 19 (a), one will see that bandlet 2 and 3 originate from the same undisturbed center-WG band. Furthermore the mode profile is changing continuously along the bandlet of the non-lossy simulation. These are the reasons why, the nearer the modes of bandlet 2 and 3 are to each other in terms of frequency, the more the modes will resemble each other.
For the calculation of the mode overlap term the modes of the loss-less simulations were used. Correspondingly the mode-overlap will be even bigger, compared to the lossy modes. Here the mode overlap $\boxed{\mathrm{MO}}_{832}$ essentially describes the self-similarity of the mode along the undisturbed center WG band, while at the same time incorporating the pump mode. The latter is however assumed to be unchanged over the course of its bandlet.

The full JSA for these two bandlets consists of a product of the previously mentioned individual parts [see (40) on 19] and is shown in Fig. 22. We find that the most efficient SPDC happens for big ω_2, as seen in the group-index and mode-overlap terms.

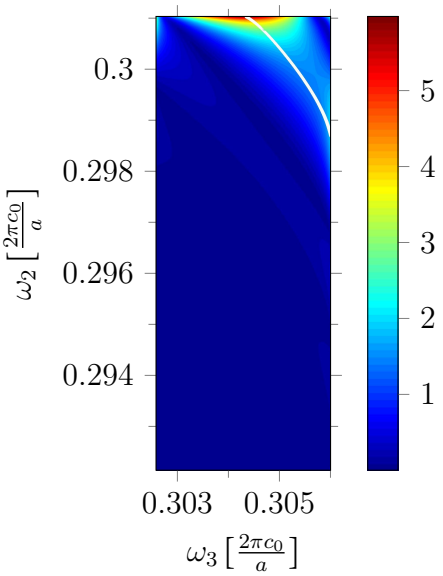

Fig. 22: $|\mathrm{JSA}_{8\,3\,2}|$ for the lossy bandlets as labeled in Fig. 19 on page 44 with a pump amplitude $A^{(p)}_{8\,\omega_3+\omega_2} \equiv 1$.

Superimposed is the damped oscillatory behavior of the phase-matching term.

4.3. Full Joint Spectral Amplitude for the Designed Structure

For the full number of different JSAs every possible combination of pump, signal and idler bandlets has to be considered. With one pump bandlet and $m = 7$ signal and idler bandlets the number of possible combinations is $m^2 = 49$.

The act of calling the two created photons signal and idler, however, is arbitrary. This becomes obvious if we e.g. choose band 3 as signal and band 7 as idler or band 7 as signal and band 3 as idler; the experimental observations will both times be a photon of band 7 in the forward direction and a photon of band 3 in the backward direction. Experimentally the labels signal and idler have no meaning; numerically however we need to be able to distinguish all possibilities, which is why these names are used.
The experimental arbitrariness of these names is represented by the fact that the JSA is unchanged under a concurrent exchange of signal and idler bandlets and frequencies:

$$\mathrm{JSA}_{m_p\,m_s\,m_i}(\omega_s+\omega_i,\omega_s,\omega_i) = \mathrm{JSA}_{m_p\,m_i\,m_s}(\omega_i+\omega_s,\omega_i,\omega_s)\ . \tag{47}$$

Considering this the number of different combinations to be calculated is only $\frac{m\,[m+1]}{2} = 28$.

This is still quite a big number of possibilities for presenting them in a master thesis. Each of these JSAs has a distinct shape and the possible values vary over several orders of magnitude, i.e. some processes are much more efficient than others. In order to get an overview over the possible processes and to easily see which process is dominant, I chose to show the squared absolute values of all JSAs summed up. Prior to that I want to show the positions of phase-matching, to get an idea of what can be expected. The latter can be seen in Fig. 23.

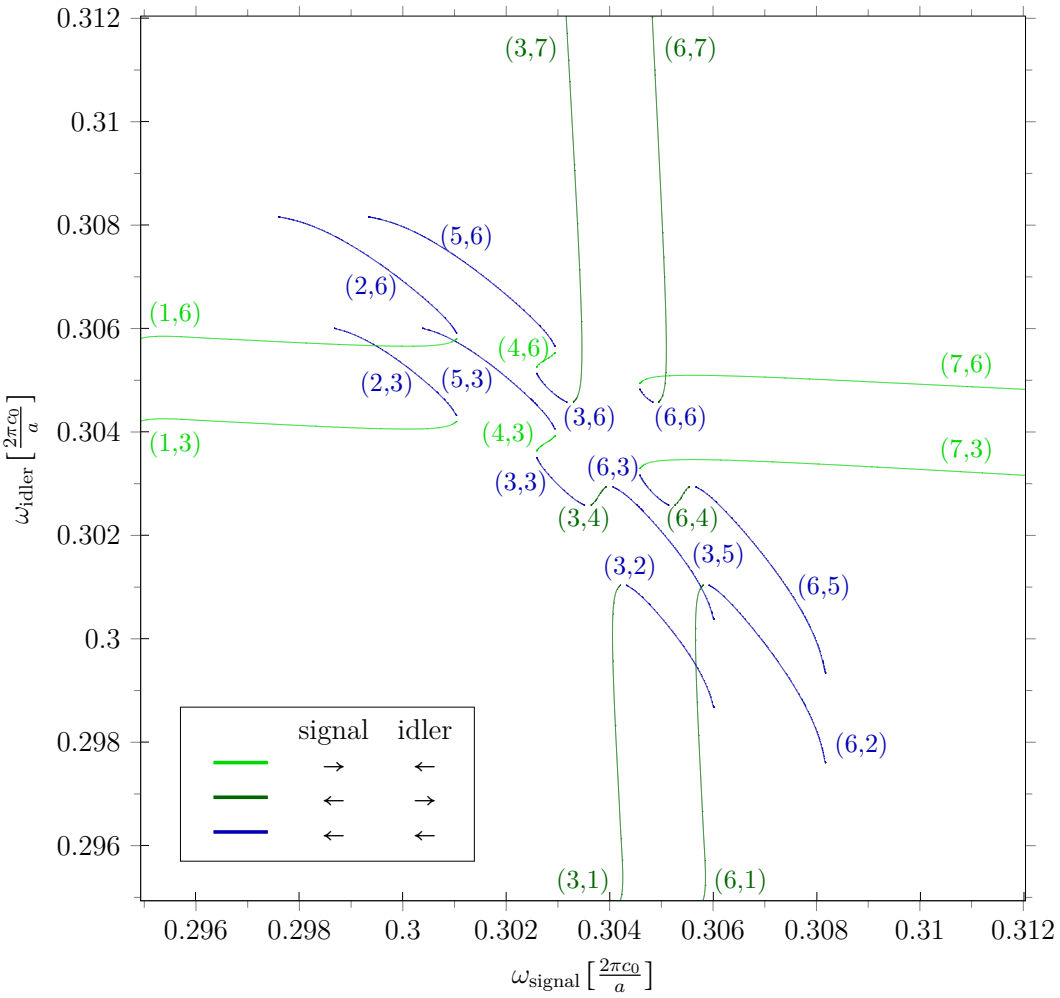

Fig. 23: $\mathrm{Re}\,(\Delta k) = 0$-contours for the designed structure [$d_{\text{center}} = 1.7\,a$, $d_{\text{side}} = 1.55\,a$, $h_{\text{WGs}} = 1.2\,a$, $r_{\text{holes}} = 0.2\,a$, $\Delta x_{\text{holes}} = 0.25\,a$, $\Delta y_{\text{WGs}} = 0.4\,a$] with the bandlets as shown in Fig. 19 on page 44. → depicts a forward and ← a backward propagating mode. (m_s, m_i) is naming the bandlet number of the signal m_s and of the idler m_i.

The phase-matching lines in Fig. 23 are color-coded with respect to the propagation directions of signal and idler. The directions of propagation of the created photons are an experimentally well accessible observable. The experimentally distinguishable combinations are signal and idler both forward, both backward or counter-propagating. Numerically, forward-propagating signal and backward-propagating idler were also distinguished from backward-propagating signal and forward-propagating idler; experimentally this is not possible however, because of the arbitrariness which mode to call signal or idler [see (47)].

The first thing one can notice in Fig. 23 is that the full result is symmetric with respect to the line at $\omega_{\text{signal}} = \omega_{\text{idler}}$. This also is a direct result of the ambiguity of which mode to call signal or idler, represented by the fact that, exactly as for the full JSA, $\Delta k_{m_p m_s m_i}(\omega_s + \omega_i, \omega_s, \omega_i) = \Delta k_{m_p m_i m_s}(\omega_i + \omega_s, \omega_i, \omega_s)$.

Secondly one sees, that for this structure no phase-matching for forwardly co-propagating modes exists. As explained in section 3.7 on page 41 the down-folded pump mode has to lie between the signal and idler modes for phase-matching. In the band diagram in Fig. 19 (a) on page 44 we see that all shown signal and idler bandlets with forward propagating modes [1,4 and 7] lie below the down-folded pump bandlet. Correspondingly no phase-matching can be expected.
This however does not mean that no forwardly co-propagating signal and idler pairs will be created. One sees in the band diagram Fig. 19 (a) on page 44 that the down-folded pump bandlet is close to bandlet 7. The phase-mismatch is small there. And for not too long structures a noticeable creation probability can be expected. In the chosen example with $N = 100$ periods the absolute value of the phase matching term of the pump and signal and idler of bandlet 7 reaches a maximum of $\left|\boxed{\text{PM}}_{877}\right| \approx 43$. Compared to the maximum achievable absolute value in the loss-less case for perfect phase matching of $N = 100$, which was explained earlier [see page 46], this is non-negligible.

These fully numerical results promise a lot of phase-matched photon pairs. The phase-matching condition though is only one part contributing to the final result. For the full physical description one will have to look at the JSA.

As mentioned earlier, I did not have any specific process in mind, which is why I will show the summed up squared absolute values of the JSAs for all considered bandlets. The pump amplitude was set to 1 for all considered frequencies. And because the propagation directions of the created photons is a well accessible observable, the plots are separated correspondingly. The numerical results are shown in Fig. 24.

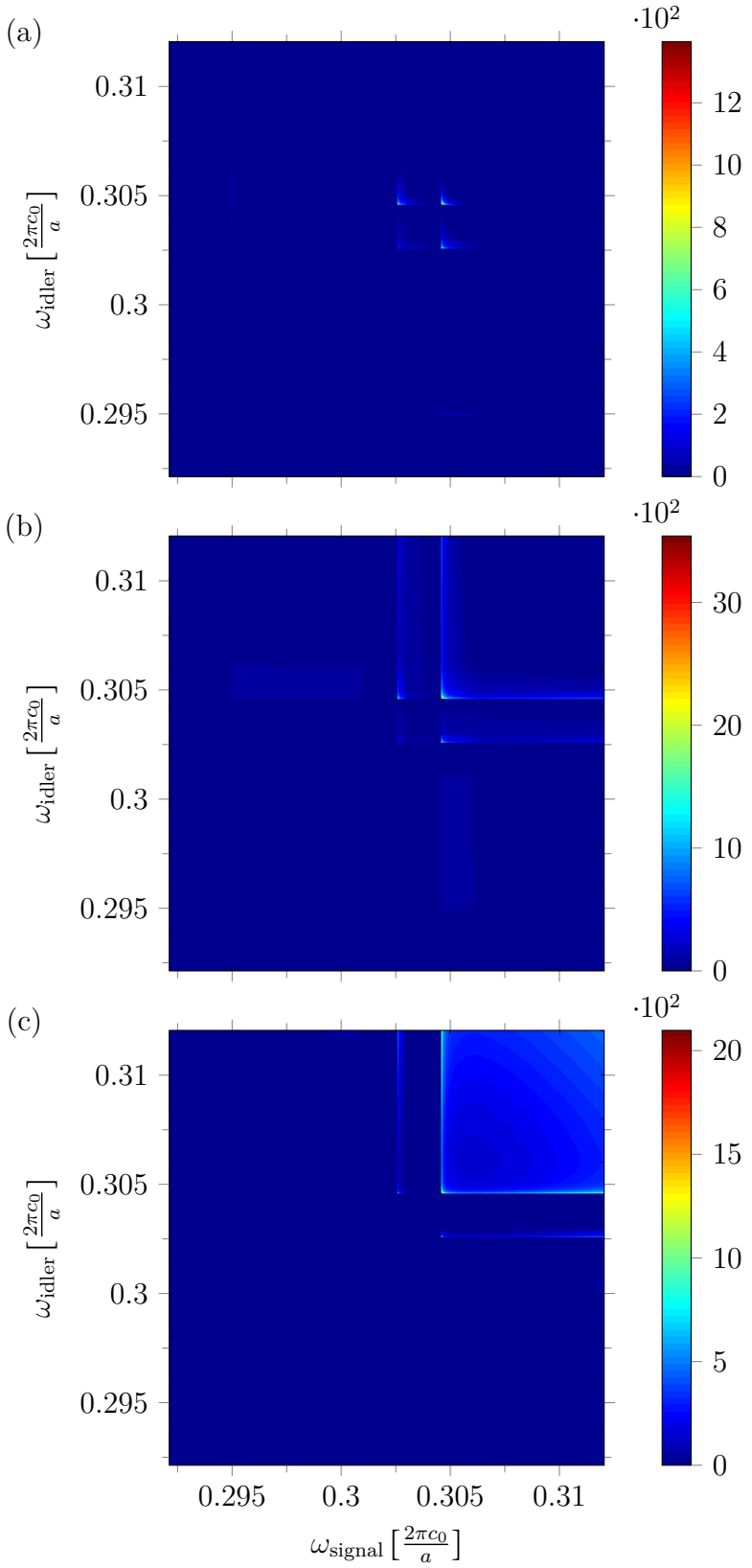

Fig. 24: $\sum_{i,j} |\text{JSA}_{8\,i\,j}(\omega_{\text{signal}} + \omega_{\text{idler}}, \omega_{\text{signal}}, \omega_{\text{idler}})|^2$ for (a) backward-propagating, (b) counter-propagating and (c) forward-propagating signal and idler [L = 100 a].

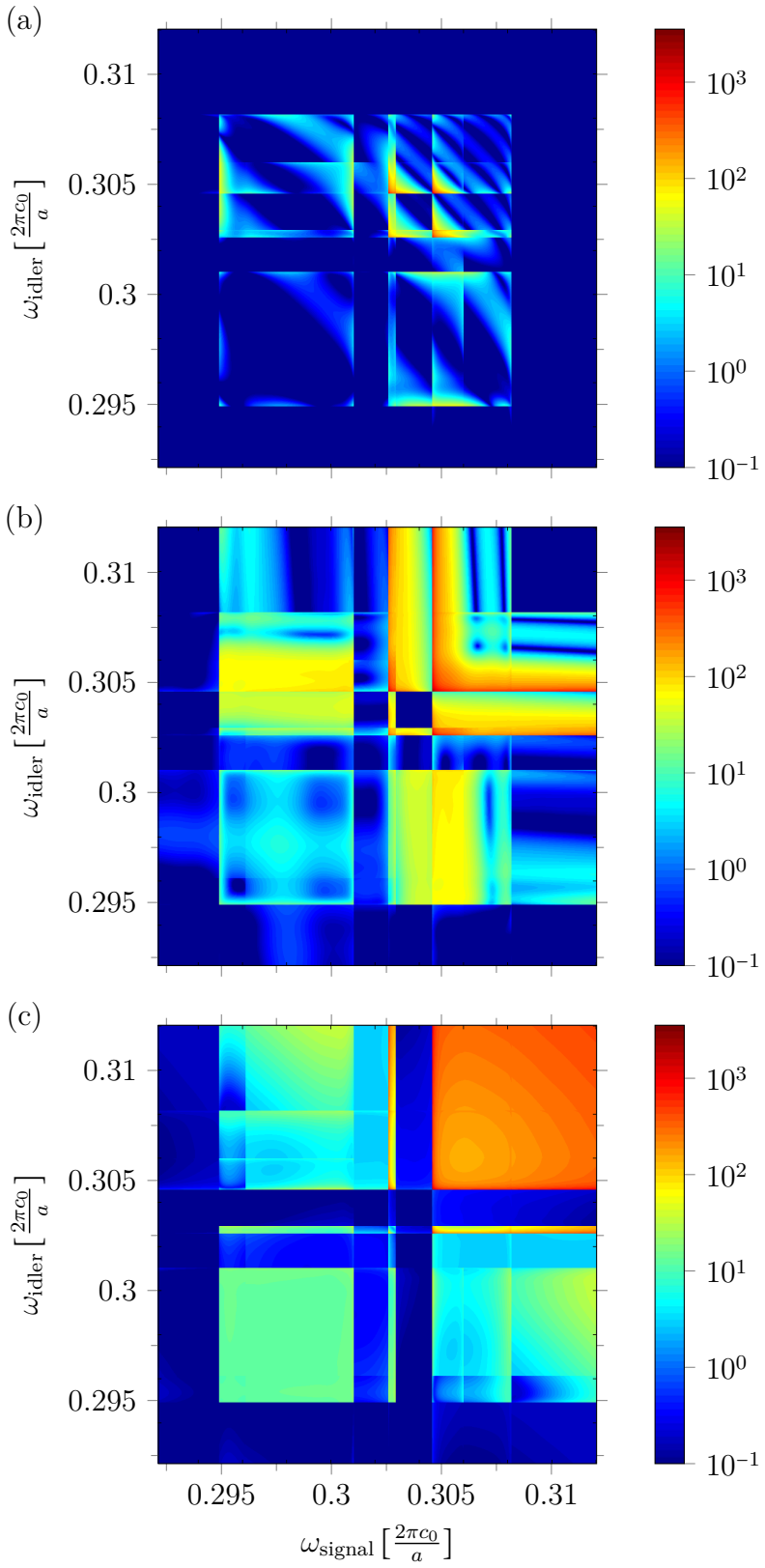

Fig. 25: $\sum_{i,j} |\mathrm{JSA}_{8\,i\,j}(\omega_{\text{signal}} + \omega_{\text{idler}}, \omega_{\text{signal}}, \omega_{\text{idler}})|^2$ with logarithmic color-scale for (a) backward-propagating, (b) counter-propagating and (c) forward-propagating signal and idler [L = 100 a].

All the JSAs are symmetric with respect to $\omega_{\text{signal}} = \omega_{\text{idler}}$. As for the phase-matching lines in Fig. 23 this symmetry originates from the ambiguity of naming a mode signal or idler [see (47) on page 48].

According to the different maxima of the color-bars it was found that the absolute values of the summed squared absolute values of the JSA for counter-propagating modes have the highest one, the ones for forwardly co-propagating modes get only up to two thirds and the ones for backwardly co-propagating modes only to a third. These relations though are strongly dependent on the length of the structure. This will be further investigated in section 4.4.

The positions of most efficient photon-pair generation are seen to mostly coincide with the positions expected from the phase-matching lines of Fig. 23. The bandlet combinations corresponding to the 4 most efficient regions visible for backwardly co-propagating signal and idler in Fig. 24 (a) are 6 and 6 [upper right], 3 and 3 [lower left], 3 and 6 [upper left] and 6 and 3 [lower right]. For counter-propagating signal and idler in Fig. 24 (b) bandlets 6 and 7 [vertical] and 7 and 6 [horizontal] make up the dominant region on the upper right and bandlets 3 and 7 [vertical] and 7 and 3 [horizontal] account for the second brightest regions next to the first. For forwardly co-propagating signal and idler in Fig. 24 (c) the upper right region of comparatively high JSA is much wider than any of the previously described ones. It stems from bandlet 7, i.e. two photons are created of the same bandlet. The other visible regions originate from bandlets 4 and 7 [vertical] and 7 and 4 [horizontal].
These findings reflect the fact, that for a forward propagating pump forwardly co-propagating solutions are inherently more broadband compared to backwardly co- and counter-propagating photon pairs. In choosing forward, counter, or backward propagating photon pairs one can thus choose, independently of the pump, a broader, less broad or narrow bandwidth for signal and idler.

For the bandlet combinations of Fig. 24 (c), i.e 7 and 7, 4 and 7 and 7 and 4, no phase-matching to the selected pump-mode exists. Nevertheless JSA-values comparable in magnitude to the phase-matched processes are achieved. This is because the phase-mismatch is not too big, the length of the structure is only 100 periods and the absolute values of the mode-overlap $\boxed{\text{MO}}_{877}$ are, apart from at the position of the anti-crossing, quite big [compare Fig. 18 (c) and (f) on page 42].

Then again it exist phase-matching positions in Fig. 23, for which no contribution in

the summed up JSA can be seen. For those the mode-overlap term is too small.

All of these observations are specific to the designed structure and the chosen length. If one increases the length of the structure, the phase-matching term will become more and more important. For a loss-less case this can be easily seen in the phase-matching term $\boxed{\text{PM}}$, whose amplitude is proportional to a sinc with the total length of the structure in its argument [see (33) on page 17]. That means, around the positions of perfect phase-matching, the phase-matching term $\boxed{\text{PM}}$ will become narrower for longer structures. For a lossy structure additionally the overall losses will increase with the length. The actual behavior for the chosen structure as a function of its length will be discussed in the next subsection.

4.4. Effect of the Length of the Structure

The total efficiency of SPDC as obtained from the integration of the summed squared absolute values of the JSAs over the full simulated signal and idler frequencies as a function of the length of the structure for the arbitrarily chosen $\mathrm{Im}(\varepsilon_r) = 0.001$ is given in Fig. 26. The results are again classified by the experimentally observable propagation directions of signal and idler, namely forward- [→→], counter- [→←] and backward-propagating [←←].

For the ←← modes the material-loss leads to an asymptotic behavior for long structures. With 800 periods 99 % of the maximum 0.115×10^{-2} are reached. For structures shorter than 1000 periods the efficiency is smaller for ←← modes compared to →→ and →← modes. The maximum over all considered lengths for the ←← modes is at least 10 times smaller than the maxima of the →→ or →← photon pairs. For structures longer than 7000 periods it is at least 10 times stronger than any of the other contributions.
This asymptotic behavior can be understood with a simplified picture. One has to consider that the forward propagating pump as well as all other signal and idler modes are damped along their propagation directions. This means that the pump intensity is decaying along the length of structure. Accordingly the non-linear efficiency becomes smaller further along the structure. For ←← photon pairs the contribution to the creation probability from places further along the structure additionally becomes smaller, because potentially created photons have to propagate all the way back to the beginning of the lossy structure. This means, that the main contribution for the ←← modes originates from the region in the structure near the input of the pump mode.

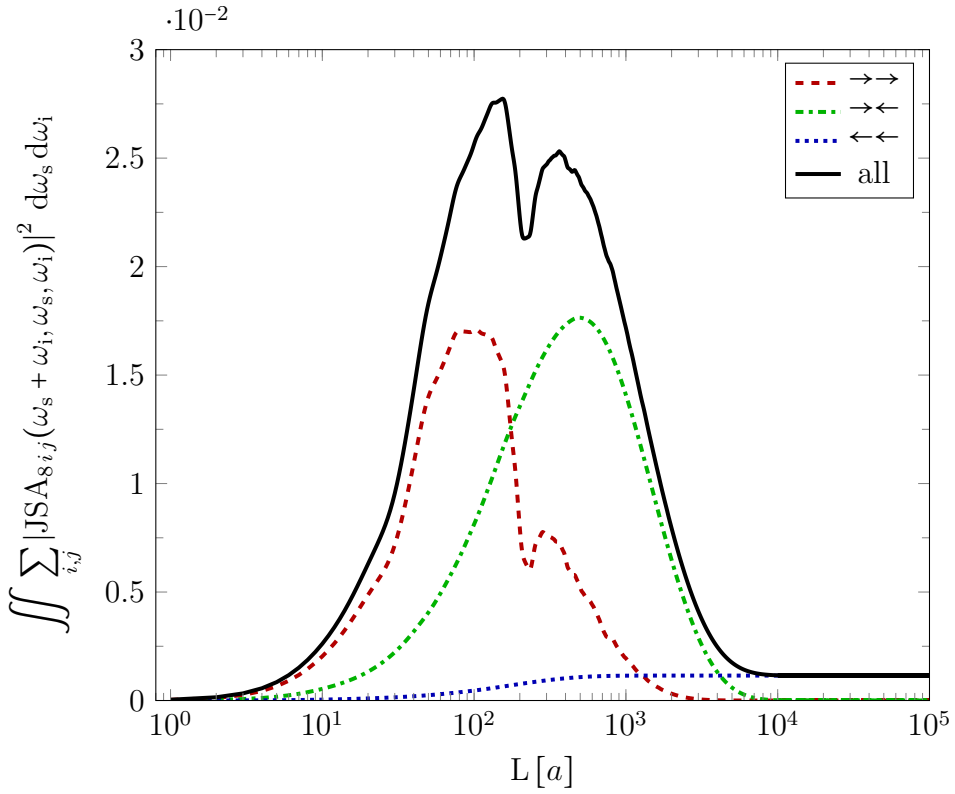

Fig. 26: $\iint \sum_{i,j} |\mathrm{JSA}_{8\,i\,j}(\omega_\mathrm{s}+\omega_\mathrm{i},\omega_\mathrm{s},\omega_\mathrm{i})|^2 \,\mathrm{d}\omega_\mathrm{s}\,\mathrm{d}\omega_\mathrm{i}$ as a function of the length L of the designed structure [$d_\mathrm{center} = 1.7\,a$, $d_\mathrm{side} = 1.55\,a$, $h_\mathrm{WGs} = 1.2\,a$, $r_\mathrm{holes} = 0.2\,a$, $\Delta x_\mathrm{holes} = 0.25\,a$, $\Delta y_\mathrm{WGs} = 0.4\,a$].

The fact, that the maximum of the creation probability for ←← modes is much smaller compared to the maxima of →← or →→ modes, originates from the previously mentioned fact, that for this structure the mode overlap for the forward propagating signal and idler modes is much bigger with the pump mode, compared to the backward propagating ones. This was shown for the chosen length of $L = 100\,a$, but the variation of the length of the structure changes solely the PM in the JSA.
The main photon pairs contributing are, with smaller and smaller quantities, bandlets 6 and 6, bandlets 6 and 3 and bandlets 3 and 3. As mentioned earlier, the phase-matching condition becomes more and more important for longer structures. Accordingly the regions of efficient SPDC for ←← photon pairs are strongly confined to the phase-matching lines shown in Fig. 23 on page 49.

The most efficiently created modes for structure lengths smaller than 170 periods are the →→ ones. Their maximum value is 1.71×10^{-2} for a structure length of 103 periods.

At around 280 periods a second local maximum can be seen for the →→ photon pairs. Both of these maxima originate from signal and idler modes of bandlet 7. For the first and higher maximum a quite wide JSA in terms of frequency as shown in Fig. 24 (c) is responsible; the second maximum originates from a much more narrow but higher valued JSA at the highest considered frequency values around $0.305\,\frac{2\pi c_0}{a}$.
The very broadband JSA here for →→ modes originates from the fact, that the high group index for small frequencies of bandlet 7 compensates the slightly bigger phase-mismatch, compared to modes with higher frequencies. As mentioned earlier, a high group index not only corresponds to increased non-linear interactions with the material, but also stronger losses. That is why the contribution to the creation probability of modes of bandlet 7 lower in frequency becomes smaller after the first maximum quite fast. The modes of bandlet 7 higher in frequency have smaller group indices and smaller phase-mismatches, which is why they have a maximal creation probability for a a longer structure.
For very long propagation distances in a lossy structures every mode is damped away. Accordingly the creation probability for →→ photon pairs approaches 0 for long structures.

The counter-propagating signal and idler pairs show, although for a much longer structure, an even higher total creation efficiency compared to the →→ modes. The global maximum for →← modes is 1.77×10^{-2} at a length of 494 periods. Here the photon pairs of bandlets 6 and 7 contribute the most. For this length of the structure the resulting JSA has a quite narrow bandwidth around the phase-matching lines, which are shown in Fig. 23 on page 49.

Again, depending on the actual structure and a physically more reasonable pump amplitude [here it was $A^{(p)}_{8\,\omega_3+\omega_2} \equiv 1$], this results will look differently. As a general insight I would like to state that for forward propagating and counter-propagating signal and idler the forward-propagating mode will for long structures be damped away, so that those efficiencies will always show a global maximum. The purely backward-propagating signal and idler photons just won't see the rest of the structure after a certain length, which is why they will always asymptotically reach a global maximum for long structures.

4.5. Effect of Tuning the Pump Mode

To further investigate the effects of the phase-matching term, I varied the position of the pump bandlet by shifting it up or down. It should be mentioned that I did this manually

here, i.e. I added a constant value to the frequencies of the pump-bandlet. One could however imagine different designs, where the pump bandlet would be shifted in similar ways relative to the signal and idler bandlets. At the same time changes to the signal and idler bandlets would be unavoidable, but could be weak [25]. Because I wanted to focus on the effect of a shift of the pump bandlet alone, I chose above method.

For the simulations a structure length of 100 periods was assumed again. And for simplicity the squared absolute values of the JSAs of all propagation directions of signal and idler were summed up now. The resulting figures can be seen in Fig. 27.

Regarding the effect of the pump bandlet shifts on the JSAs it is, because the mode profiles of the pump were assumed to be unchanged along the pump bandlet, $\boxed{\text{PM}}$ the only affected term. This means that all differences in these figures compared to Fig. 24 on page 51 arise solely from the different phase-mismatch terms.

In Fig. 27 (a) the combinations of bandlets 6 and 6 and bandlets 3 and 6 are the most efficient ones. The maximal efficiency is comparable to the one of the previous calculations with the unshifted pump bandlet. The regions of high JSA values are however much narrower and strongly confined around the phase-matching regions. As can be seen in the inset band diagram, there exist two crossings of the down-folded pump bandlet with the signal and idler bandlets 3 and 5. At these points energy- and momentum-conservation [i.e. phase-matching] are fulfilled, but for the bandlet combination of 3 and 3 no contributions to the JSA can be seen. This is because the mode overlap is comparatively small, as can be seen from the field profiles in Fig. 18 (h) and (j) on page 42.

In Fig. 27 (b) the combinations of the bandlet 6 and 4 and bandlets 6 and 7 make the main contributions. The maximal value is a factor 5 smaller compared to Fig. 27 (a). Additionally an overall shift to lower frequencies, consistent with the shift of the pump mode, can be observed.

In the inset of Fig. 27 (c) the closeness of the pump bandlet and bandlets 1 and 4 can be seen. As stated earlier, it is the mode overlap of the modes of bandlets 1, 4, and 7 with the pump bandlet modes quite good. Accordingly the JSA shows high values for the bandlet combinations 4 and 4 [dot in center], 1 and 4 [narrow regions left and below the center dot] and 1 and 1 [lower left region]. Additionally the regions of bandlets 1 and 7 [lower right and upper left] and 5 and 7 [right or above the center dot] can be seen. With these wide regions with nearly constant high JSA values broad bandwidths of photon pairs could be created with this structure.

Fig. 27 (d), where the pump bandlet is shifted even lower, the highest values one again

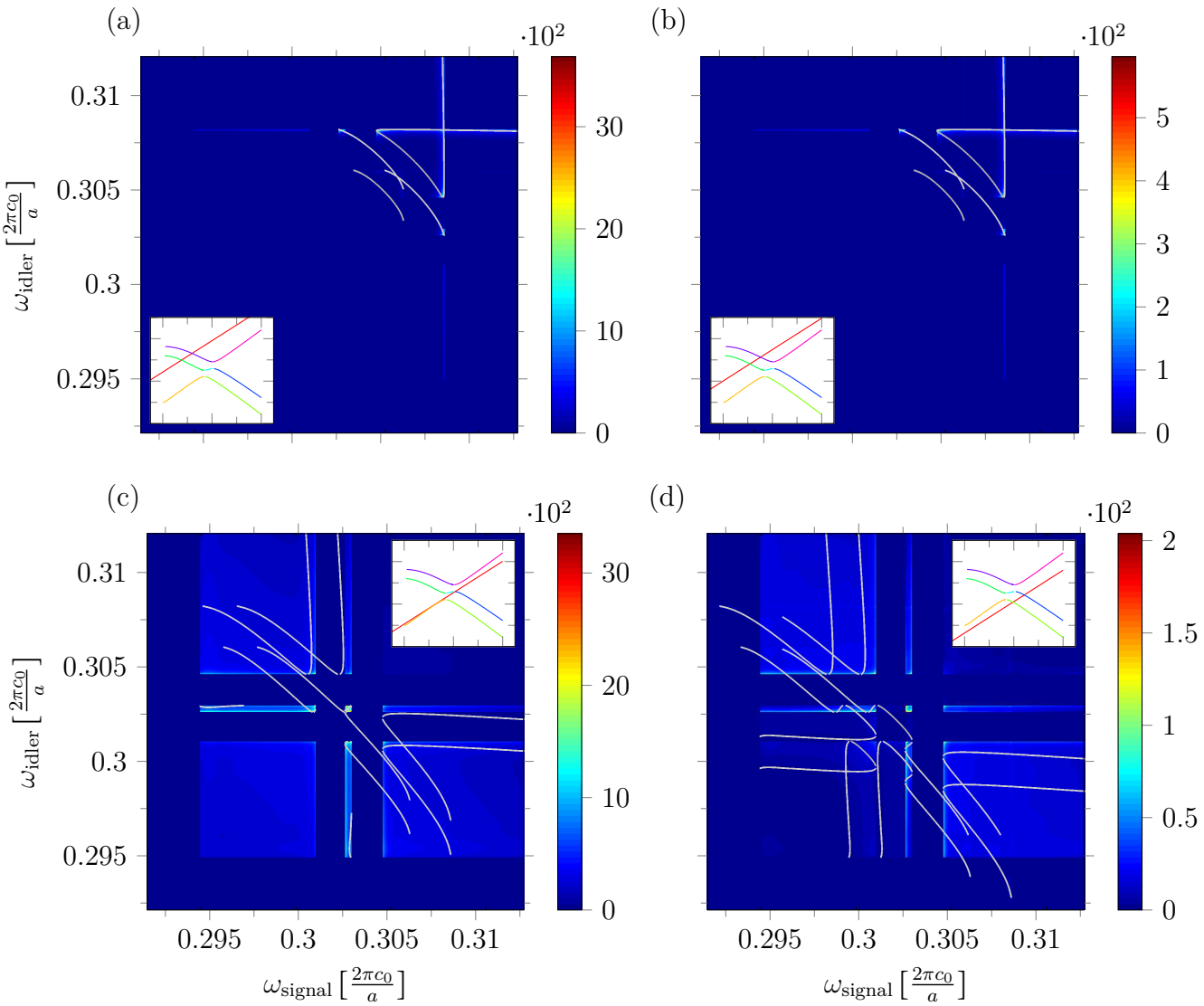

Fig. 27: $\sum_{i,j} |\text{JSA}_{8\,i\,j}(\omega_{\text{signal}} + \omega_{\text{idler}}, \omega_{\text{signal}}, \omega_{\text{idler}})|^2$ combined from all considered bandlets as a function of a manually induced shift of the pump bandlet in terms of frequency [(a) $+0.009\,\frac{2\pi}{a}$, (b) $+0.005\,\frac{2\pi}{a}$, (c) $-0.005\,\frac{2\pi}{a}$, (d) $-0.009\,\frac{2\pi}{a}$; $d_{\text{center}} = 1.7\,a$, $d_{\text{side}} = 1.55\,a$, $h_{\text{WGs}} = 1.2\,a$, $r_{\text{holes}} = 0.2\,a$, $\Delta x_{\text{holes}} = 0.25\,a$, $\Delta y_{\text{WGs}} = 0.4\,a$, $\text{L} = 100\,a$]. The white lines show phase-matching [$\text{Re}(\Delta k) = 0$]. In the insets the unshifted signal and idler bandlets and the shifted pump bandlet are shown [the ticks and signal/idler bandlets are the same as in Fig. 19 on page 44].

sees for the bandlet combination 4 and 4. The overall magnitude is, compared to the previous one, smaller by a factor of 10. The phase-matching positions do not coincide with the positions of high JSA, because the mode-overlap of bandlets 2 or 5 with the

pump mode is quite bad [see Fig. 18 (a) and (d) or (b) and (j) on page 42].

To summarize I state, that the regions of high JSA will move generally with the bandlet of the pump mode. For an efficient JSA however, as expected from a product, all factors of the JSA as given in (40) on page 19 have to be sufficiently big coincidentally.

5. Conclusion and Outlook

The aim of this thesis was to better understand the possibilities guiding periodic nanostructures of optically non-linear materials offer for controlling the properties of optically non-linear processes. In this thesis I focused on an optical material with a strong χ_2 non-linearity. For the non-linear optical process spontaneous parametric down-conversion [SPDC] was chosen.

As a first step the non-linear interaction was formulated analytically in terms of the guided modes of the nanostructure. Because the structure was assumed to be periodic along its guiding direction as well, the modes were Bloch modes. These Bloch modes could be slightly lossy, which every mode in a fabricated nanostructure is today. To simplify the involved calculations, it was assumed that the χ_2 process is weak and that correspondingly only single photon pairs are created. This way a less computationally demanding result for the joint spectral amplitude [JSA] could be derived, whose absolute value squared represents the creation probability density of the photon pair created in a SPDC process.

For actual calculations a structure consisting of three coupled waveguides [WGs] side by side on a substrate was chosen. The outer WGs were structured periodically with cylindric holes. The non-linear material was assumed to be made of lithium niobate [$LiNbO_3$], which features a substantial χ_2 non-linearity. The goal of this design was to confine the pump mode in the unstructured center WG and thus shield it from the losses, the periodic outer WGs otherwise would have induced. The signal and idler modes on the contrary were intrinsically loss-less even in a periodic structure. Therefore they extended transversally over all three WGs and could be affected by the periodicity of the outer WGs.
To understand the physical effects that dictate the linear-optical properties of this structure, and indirectly the non-linear properties as well, the coupling of WGs, the effects coupling the WGs, the periodicity and the substrate were investigated in detail via fully vectorial eigensolvers of the Maxwell equations. With the findings from these investigations a design for a structure with promising linear optical properties was found.

For this structure I then calculated its non-linear properties via the formula found in the first step. The results were presented in detail for one specific structure. Additionally the effects of varying the length or the phase-matching condition by shifting the pump modes in frequency are discussed.
The proposed structure is found to show a lot of interesting non-linear properties.

Via choosing an appropriate pump, using frequency filters for signal and idler and distinguishing between forward and backward propagating photons, e.g. a variety of entangled two-photon states can be designed.

The results of this thesis should enable the reader to design the linear and non-linear optical properties of periodic nanostructures to his wishes. Prior to an actual experiment additional care will have to be taken, to efficiently couple the light in and out of the structure. Because of the small size of the structure the proposed nanostructure not only offers good control over the optical properties, but e.g. on-chip implementations for applications in optical quantum networks should be possible.

6. References

[1] J.-H. Han and J. U. Kang, "Correlated photon-pair source for secured C-band quantum communications", IEEE Photonics Technology Letters **23**, 1178–1180 (2011).

[2] J.-H. Han, "Photon pair sources for quantum information networks and remote sensing systems", in "Optical Internet 2014 (COIN), 2014 12th International Conference on," (IEEE, 2014), pp. 1–2.

[3] O. Slattery, L. Ma, P. Kuo, Y.-S. Kim, and X. Tang, "Frequency correlated biphoton spectroscopy using tunable upconversion detector", Laser Physics Letters **10**, 075201 (2013).

[4] O. Alibart, J. Fulconis, G. K. L. Wong, S. G. Murdoch, W. J. Wadsworth, and J. G. Rarity, "Photon pair generation using four-wave mixing in a microstructured fibre: theory versus experiment", New Journal of Physics **8**, 67 (2006).

[5] S. Clemmen, K. P. Huy, W. Bogaerts, R. G. Baets, P. Emplit, and S. Massar, "Continuous wave photon pair generation in silicon-on-insulator waveguides and ring resonators", Optics express **17**, 16558–16570 (2009).

[6] S. Saravi, F. Setzpfandt, and T. Pertsch, "Counter-propagating spatially entangled bell-states generation in photonic crystal waveguides", in "CLEO: Science and Innovations," (Optical Society of America, 2016), pp. JTu5A–25.

[7] N. Gutman, W. H. Dupree, Y. Sun, A. A. Sukhorukov, and C. M. de Sterke, "Frozen and broadband slow light in coupled periodic nanowire waveguides", Opt. Express **20**, 3519–3528 (2012).

[8] "INRAD lithium niobate datasheet", http://www.lambdaphoto.co.uk/pdfs/Inrad_datasheet_LNB.pdf .

[9] M. M. Abouellell and F. J. Leonberger, "Waveguides in lithium niobate", Journal of the American Ceramic Society **72**, 1311–1321 (1989).

[10] J. D. Jackson, *Classical Electrodynamics* (John Wiley & Sons, 1963), 3rd ed.

[11] S. G. Johnson and J. D. Joannopoulos, "Block-iterative frequency-domain methods for maxwell's equations in a planewave basis", Opt. Express **8**, 173–190 (2001).

[12] G. G. Paulus, "Classical nonlinear optics", (2014). Script to the lecture of the same name at the FSU Jena in the WS2014.

[13] J. D. Joannopoulos, S. G. Johnson, J. N. Winn, and R. D. Meade, *Photonic crystals: molding the flow of light* (Princeton university press, 2011).

[14] F. Bloch, "Über die Quantenmechanik der Elektronen in Kristallgittern", Zeitschrift für Physik **52**, 555–600 (1928).

[15] S. Saravi, "face-to-face conversations", .

[16] S. Skupin, "Waveguide theory", (2011). Script of a lecture at FSU Jena in 2011.

[17] J. E. Sipe, N. A. R. Bhat, P. Chak, and S. Pereira, "Effective field theory for the nonlinear optical properties of photonic crystals", Physical Review E **69**, 016604 (2004).

[18] A. N. Poddubny, I. V. Iorsh, and A. A. Sukhorukov, "Generation of photon-plasmon quantum states in nonlinear hyperbolic metamaterials", Physical Review Letters **117**, 123901 (2016).

[19] A. F. Oskooi, D. Roundy, M. Ibanescu, P. Bermel, J. D. Joannopoulos, and S. G. Johnson, "MEEP: A flexible free-software package for electromagnetic simulations by the FDTD method", Computer Physics Communications **181**, 687–702 (2010).

[20] A. Taflove, S. C. Hagness *et al.*, *Computational electrodynamics: the finite-difference time-domain method* (Artech House, 1995).

[21] M. R. Wall and D. Neuhauser, "Extraction, through filter-diagonalization, of general quantum eigenvalues or classical normal mode frequencies from a small number of residues or a short-time segment of a signal. i. theory and application to a quantum-dynamics model", The Journal of chemical physics **102**, 8011–8022 (1995).

[22] V. A. Mandelshtam and H. S. Taylor, "Harmonic inversion of time signals and its applications", The Journal of chemical physics **107**, 6756–6769 (1997).

[23] A. F. Oskooi, L. Zhang, Y. Avniel, and S. G. Johnson, "The failure of perfectly matched layers, and towards their redemption by adiabatic absorbers", Opt. Express **16**, 11376–11392 (2008).

[24] K. C. Huang, E. Lidorikis, X. Jiang, J. D. Joannopoulos, K. A. Nelson, P. Bienstman, and S. Fan, "Nature of lossy bloch states in polaritonic photonic crystals", Physical Review B **69**, 195111 (2004).

[25] S. Saravi, S. Diziain, M. Zilk, F. Setzpfandt, and T. Pertsch, "Phase-matched second-harmonic generation in slow-light photonic crystal waveguides", Physical Review A **92**, 063821 (2015).

[26] R. Quintero-Bermudez, "Parametric frequency conversion in nanostructured waveguides", masterthesis, Friedrich-Schiller-Universität Jena (2015).

[27] S. Sanna and W. G. Schmidt, "Lithium niobate x-cut, y-cut, and z-cut surfaces from ab initio theory", Physical Review B **81**, 214116 (2010).

[28] I. H. Malitson, "Interspecimen comparison of the refractive index of fused silica", JOSA **55**, 1205–1209 (1965).

[29] D. E. Zelmon, D. L. Small, and D. Jundt, "Infrared corrected sellmeier coefficients for congruently grown lithium niobate and 5 mol.% magnesium oxide–doped lithium niobate", JOSA B **14**, 3319–3322 (1997).

[30] P. Radaelli, *Symmetry in crystallography: understanding the international tables*, vol. 17 (Oxford University Press, 2011).

[31] T. P. White and A. A. Sukhorukov, "Transition from slow and frozen to superluminal and backward light through loss or gain in dispersion-engineered waveguides", Physical Review A **85**, 043819 (2012).

[32] J. G. Pedersen, S. Xiao, and N. A. Mortensen, "Limits of slow light in photonic crystals", Physical Review B **78**, 153101 (2008).

[33] P. Sivarajah, A. A. Maznev, B. K. Ofori-Okai, and K. A. Nelson, "What is the brillouin zone of an anisotropic photonic crystal?" Physical Review B **93**, 054204 (2016).

A. Derivation of Bloch Modes

To start a potentially lossy 1D-periodic photonic crystal described with $\hat{\varepsilon}_r(\vec{r},\omega)$ is assumed. The direction of periodicity was w.l.o.g. chosen to be along $\vec{e}_x$, so that the primitive lattice vector is $\vec{a} = a\vec{e}_x$. This means that

$$\hat{\varepsilon}_r(\vec{r},\omega) = \hat{\varepsilon}_r(\vec{r}+\vec{R}_n,\omega) \quad , \quad \forall \vec{R}_n = n\,\vec{a}\ ,\ n \in \mathbb{Z}\ . \tag{48}$$

Via the coordinate transformation $\vec{r}' = \vec{r} + \vec{R}_n$ in (5), using (8) and $\vec{\nabla}' = \vec{\nabla}$, one gets

$$\vec{\nabla} \times \left[\hat{\varepsilon}_r^{-1}(\vec{r},\omega)\left[\vec{\nabla} \times \vec{H}(\vec{r}+\vec{R}_n,\omega)\right]\right] = \left[\frac{\omega}{c_0}\right]^2 \vec{H}(\vec{r}+\vec{R}_n,\omega)\ . \tag{49}$$

Comparing (49) and (5) and requiring continuity of $\vec{H}(\vec{r},\omega)$ in $\vec{r}$ it follows:

$$\vec{H}(\vec{r},\omega) = \vec{H}(\vec{r}+\vec{R}_n,\omega)\ \mathrm{e}^{\mathrm{i}\,\varphi(\vec{R}_n,\omega)} \quad , \quad \forall \vec{R}_n\ ,\ \varphi(\vec{R}_n,\omega) \in \mathbb{C}. \tag{50}$$

Looking at the two identical results of shifting $\vec{H}(\vec{r},\omega)$ once by $2\,\vec{R}_n$ or twice by $1\,\vec{R}_n$ one gets

$$\vec{H}(\vec{r}+2\vec{R}_n,\omega)\ \mathrm{e}^{\mathrm{i}\,\varphi(2\vec{R}_n,\omega)} = \vec{H}(\left[\vec{r}+\vec{R}_n\right]+\vec{R}_n,\omega)\ \mathrm{e}^{\mathrm{i}\,2\varphi(\vec{R}_n,\omega)}\ . \tag{51}$$

This means that $\varphi(\vec{R}_n,\omega)$ is linear in $\vec{R}_n$, i.e. it can be written as

$$\varphi(\vec{R}_n,\omega) =: \vec{R}_n \cdot \vec{\Phi}(\omega) \quad , \quad \vec{\Phi}(\omega) \in \mathbb{C}^3\ . \tag{52}$$

Assuming that the fields in the 1D photonic crystal can be described with electromagnetic waves, the following ansatz is made

$$\vec{H}(\vec{r},\omega(k)) =: \vec{H}(\vec{r},k)\ \mathrm{e}^{\mathrm{i}\,k\,x} \quad , \quad k \in \mathbb{C}\ , \tag{53}$$

with the wave-vector component along the periodicity k and the dispersion relation $\omega(k)$. Pluggin (52) and (53) into (50) one finds

$$\vec{\Phi}(\omega) = x\,\vec{e}_x \quad \text{and} \quad \vec{H}(\vec{r},k) = \vec{H}(\vec{r}+\vec{R}_n,k)\ . \tag{54}$$

From the spatial periodicity of $\hat{\varepsilon}_r(\vec{r},\omega)$ a periodicity for the dispersion relation $\omega(\vec{k})$

can be derived as well. For that purpose one can plug (53) into (5) for $\vec{k} = k\vec{e}_x$

$$\left[\frac{\omega(k)}{c_0}\right]^2 \vec{H}(\vec{r},k) = [\vec{\nabla} + \mathrm{i}\,\vec{k}] \times \left[\hat{\varepsilon}_r^{-1}(\vec{r},\omega)\,\left[[\vec{\nabla} + \mathrm{i}\,\vec{k}] \times \vec{H}(\vec{r},k)\right]\right] , \tag{55}$$

as well as for $\vec{k} + \vec{G}_n$, where it is $\vec{G}_n = n\frac{2\pi}{a}\vec{e}_x$ with $n \in \mathbb{Z}$ [12],

$$\begin{aligned}\left[\frac{\omega(k+G_n)}{c_0}\right]^2 \vec{H}(\vec{r},k+\vec{G}_n) &= [\vec{\nabla} + \mathrm{i}\,\vec{k} + \mathrm{i}\,\vec{G}_n] \times \left[\hat{\varepsilon}_r^{-1}(\vec{r},\omega)\,\left[[\vec{\nabla} + \mathrm{i}\,\vec{k} + \mathrm{i}\,\vec{G}_n] \times \vec{H}(\vec{r},k+G_n)\right]\right] \\ &= \left[[\vec{\nabla} + \mathrm{i}\,\vec{k}] \times \left[\hat{\varepsilon}_r^{-1}(\vec{r},\omega)\,\left[[\vec{\nabla} + \mathrm{i}\,\vec{k}] \times [\vec{H}(\vec{r},k+G_n)\,\mathrm{e}^{\mathrm{i}\,\vec{G}_n\cdot\vec{r}}]\right]\right]\right]\mathrm{e}^{-\mathrm{i}\,\vec{G}_n\cdot\vec{r}}\end{aligned} \tag{56}$$

and compare the results[13].
This is solved by

$$\vec{H}(\vec{r},k) = \vec{H}(\vec{r},k+G_n)\,\mathrm{e}^{\mathrm{i}\,\vec{G}_n\cdot\vec{r}} \quad \text{and} \quad \omega(k) = \omega(k + n\,\tfrac{2\pi}{a}) \quad , \quad \forall n \in \mathbb{Z}\,. \tag{57}$$

Because the modes of $\vec{k}$ and $\vec{k} + \vec{G}_n$ are the same, it makes no sense to distinguish between them. This is the reason, that in the description of periodic problems one typically restricts the values of k to $(-\frac{\pi}{a}, \frac{\pi}{a}]$. The region in which all corresponding wave-vectors lie, is called the first Brillouin zone [1. BZ].
Every periodic function can be expressed by a Fourier series, so the eigensolutions ca be expressed as:

$$\vec{H}(\vec{r},\omega(k)) = \sum_n \vec{h}(y,z,k+n\,\tfrac{2\pi}{a})\,\mathrm{e}^{\mathrm{i}[k+n\frac{2\pi}{a}]x} = \Bigg[\overbrace{\sum_n \vec{h}(y,z,k+n\,\tfrac{2\pi}{a})\,\mathrm{e}^{\mathrm{i}\,n\frac{2\pi}{a}x}}^{\vec{H}(\vec{r},k)}\Bigg]\mathrm{e}^{\mathrm{i}\,k\,x}\ . \tag{58}$$

The $\vec{h}(k + n\,\frac{2\pi}{a})$ are called Bloch harmonics. In looking at above formula one finds, that $\vec{k} + \vec{G}_n$ are the wave-vectors of the Bloch harmonics. Thus one sees, that the physical momenta of the waves are, contrary to the used label k for the Bloch modes, not confined to the 1. BZ.

[12] The lattice spanned by all $\vec{G}$ is called the reciprocal lattice. This is a very important concept in solid state physics [e.g. crystallography or electrons in crystals]. For further informations the interested reader is referred to the literature.

[13] For 2D or 3D PCs slightly more care has to be taken [33]. There one will have to rescale the reciprocal vectors by the anisotropic $\hat{\varepsilon}_r$ values, do this derivation and rescale the results by $\hat{\varepsilon}_r^{-1}$. This can lead to a deformation of the BZs.

B. Numerical Approach Used to Find the Real ω, Complex k Bandlets

For an easier formulation I will write any bandlet as a Taylor expansion of ω in terms of k up to the polynomial order M as follows:

$$f(k,\omega) = -[\omega - \omega_0] + \sum_{n=0}^{M} a_n(k,\omega)\,[k-k_0]^n = 0\,. \tag{59}$$

In this equation all quantities are possibly complex. In the following I will again denominate the real or imaginary part of a complex quantity by single or double primes.

A lossless system can be described by purely real k and ω values

$$\tilde{f}(k',\omega') = -[\omega' - \tilde{\omega}_0'] + \sum_{n=0}^{M} \tilde{a}_n'(k',\omega')\,[k'-\tilde{k}_0']^n = 0\,. \tag{60}$$

This is what MPB returns.

As mentioned above, all quantities are potentially complex for lossy systems. Depending on the physical view on the system, ω or k can be chosen purely real. For a system, whose modes are decaying in time, but are perfectly periodic in space, e.g. a leaky cavity, k is purely real-valued:

$$\tilde{\tilde{f}}(k',\omega) = -[\omega - \tilde{\tilde{\omega}}_0] + \sum_{n=0}^{M} \tilde{\tilde{a}}_n(k',\omega)\,[k'-\tilde{\tilde{k}}_0']^n = 0\,. \tag{61}$$

This is the description that was used in MEEP for the simulations to determine the band diagrams.

In the description of the SPDC process I used to describe the modes as perfectly harmonic in time, but decaying over the course of the length of the structure. Physically this corresponds to exciting a mode at the beginning of the structure and describing how it decays when it is propagating through it. In this description ω is purely real-valued:

$$\tilde{\tilde{f}}(k,\omega') = -[\omega' - \tilde{\tilde{\omega}}_0'] + \sum_{n=0}^{M} \tilde{\tilde{a}}_n(k,\omega')\,[k-\tilde{\tilde{k}}_0]^n = 0\,. \tag{62}$$

From a physical point of view it is obvious that (61) and (62) have to become identical to (60), when the losses approach zero. Because the master equation is continuous in k, all of the above equations are assumed to be similar for small losses. That is why

$\tilde{\tilde{f}}(k',\omega)$ is approximated with the parameters of the lossless simulation:

$$\tilde{\tilde{f}}(k',\omega) \approx -[\omega - [\tilde{\omega}_0 + \mathrm{i}\,\tilde{\tilde{\omega}}_0''] + \sum_{n=0}^{M} \tilde{a}_n(k',\omega')\,[k' - \tilde{k}_0']^n = 0\,. \tag{63}$$

To get to the picture required for the SPDC description (63) is now projected on a different subspace, namely the one with purely real-valued ω and complex k:

$$\tilde{\tilde{f}}(k',\omega) \approx F(k,\omega') = -[\omega' - [\tilde{\omega}_0' + \mathrm{i}\,\tilde{\tilde{\omega}}_0'']] + \sum_{n=0}^{M} \tilde{a}_n(k',\omega')\,[k - \tilde{k}_0']^n = 0\,. \tag{64}$$

Because I was not able to satisfactorily fit the bands calculated with MPB with polynomials[14], I chose to use MATLAB's cubic spline interpolation **spline**() to calculate the bands from the points returned by MPB. The important characteristics of cubic splines are that they go exactly through the calculated (k',ω')-points returned by MPB and are continuous up to their second derivative, as expected from a physical solution. This meant that in each section between adjacent simulated (k',ω')-points of one bandlet I got a third order polynomial $[M = 3]$ with $\tilde{\omega}_0'$, $\tilde{k}_0'$ and $\tilde{a}_n(k',\omega')$.
The $\tilde{\tilde{\omega}}_0''$ are the imaginary frequency values calculated with MEEP for the same structure but with material losses.
In order to find the bandlets I determined the roots of $F(k,\omega')$[15]. A third order polynomial has three roots, which is why I chose the roots corresponding to a lossy mode[16] and with the real k'-value nearest to the non-lossy wavenumbers to find $k(\omega')$.

With this approach one problem arises: Because the cubic splines are continuous up to their second derivative at the points of the initial bands only and the lossy bands with purely real-valued ω are determined by finding the roots of a third order polynomial, the results become discontinuous at those points. For small losses and a sufficiently fine sampling of the bands this effect though is negligible.

[14] I tested polynomials with orders varying from 3 to 25. None of the fits was satisfactorily. For higher orders the description additionally became numerically unstable.
[15] After having written my own function to invert third order polynomials, I found that MATLAB offers a function to find the roots of polynomials of arbitrary order, namely **roots**().
[16] A forward propagating mode has a $k'' > 0$ and a backward propagating mode a $k'' < 0$.

C. Band Diagram Tunability Based on Design Parameters

Apart from the previously mentioned parameter variations of Δy_{WGs} in Fig. 14 on page 36 and $\Delta x_{\mathrm{holes}}$ in Fig. 15 on page 37 in the following the tunability of the band diagrams depending on the structure parameters will be presented.

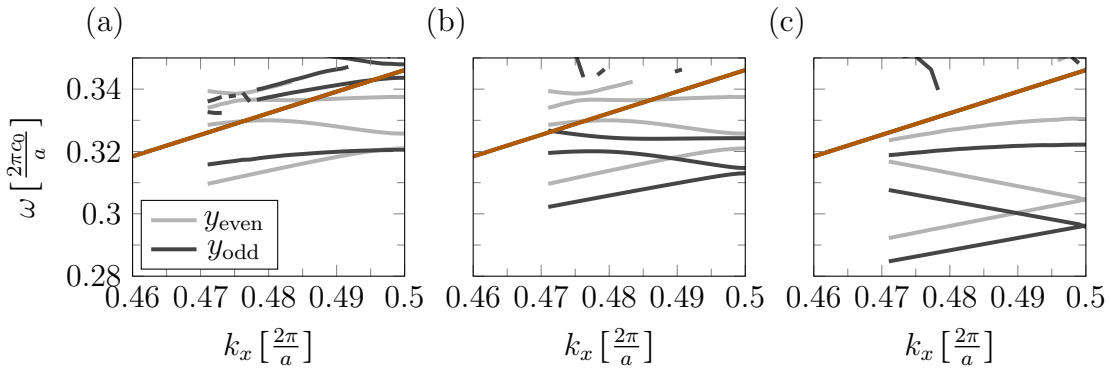

Fig. 28: Band diagrams for the variation of d_{center}: (a) $0.8\,a$, (b) $1.1\,a$, (c) $1.4\,a$ [$d_{\mathrm{side}} = 1.2\,a$, $h_{\mathrm{WGs}} = 1.15\,a$, $r_{\mathrm{holes}} = 0.3\,a$, $\Delta x_{\mathrm{holes}} = 0\,a$, $\Delta y_{\mathrm{WGs}} = 0.6\,a$].

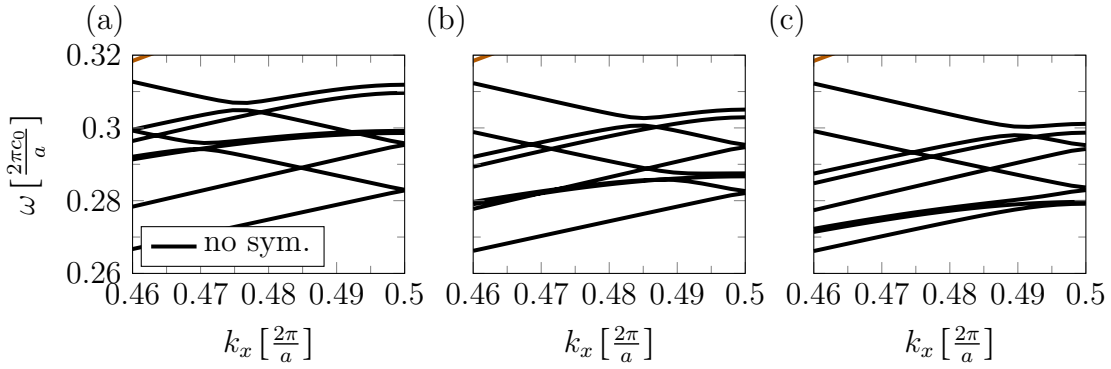

Fig. 29: Band diagrams for the variation of d_{side}: (a) $1.4\,a$, (b) $1.7\,a$, (c) $2.0\,a$ [$d_{\mathrm{center}} = 1.7\,a$, $h_{\mathrm{WGs}} = 1.2\,a$, $r_{\mathrm{holes}} = 0.2\,a$, $\Delta x_{\mathrm{holes}} = 0\,a$, $\Delta y_{\mathrm{WGs}} = 0.5\,a$].

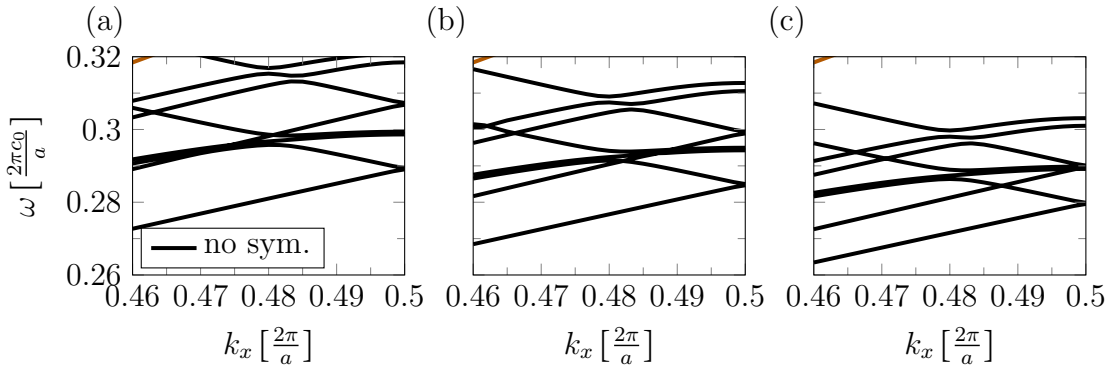

Fig. 30: Band diagrams for the variation of h_{WGs}: (a) $1.0\,a$, (b) $1.1\,a$, (c) $1.3\,a$ [$d_{\mathrm{center}} = 1.7\,a$, $d_{\mathrm{side}} = 1.55\,a$, $r_{\mathrm{holes}} = 0.2\,a$, $\Delta x_{\mathrm{holes}} = 0.25\,a$, $\Delta y_{\mathrm{WGs}} = 0.4\,a$].

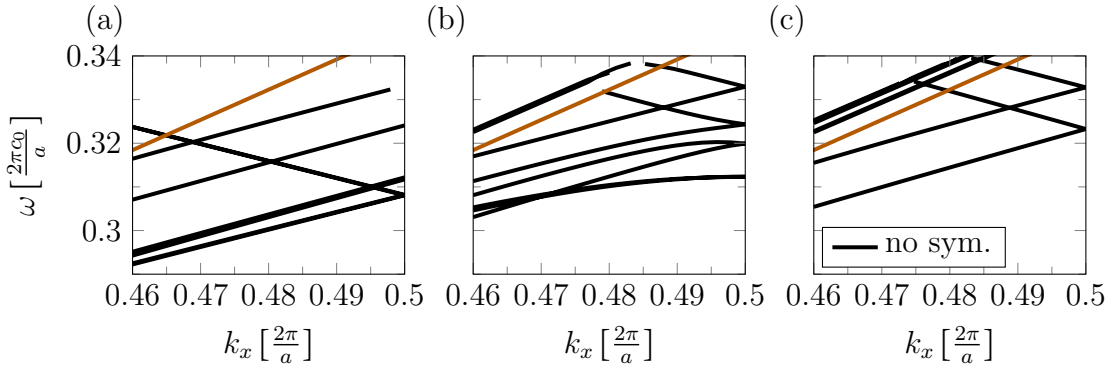

Fig. 31: Band diagrams for the variation of r_{holes}: (a) $0.0\,a$, (b) $0.2\,a$, (c) $0.4\,a$ [$d_{\mathrm{center}} = 0.9\,a$, $d_{\mathrm{side}} = 1.2\,a$, $h_{\mathrm{WGs}} = 1.1\,a$, $\Delta x_{\mathrm{holes}} = 0.5\,a$, $\Delta y_{\mathrm{WGs}} = 1\,a$].

D. Color-Codes, Abbreviations and Symbols

	no symmetry
	y-even
	y-odd
	z-even
	z-odd
	z-even and y-even
	z-even and y-odd
	z-odd and y-even
	z-odd and y-odd
	pump bandlets

$\leftarrow\leftarrow$	backward-propagating signal and idler
$\rightarrow\leftarrow$	counter-propagating signal and idler
$\rightarrow\rightarrow$	forward-propagating signal and idler

$[\hat{a}, \hat{b}]$	commutator
δ_{mn}	Kronecker delta
$\delta(x)$	Dirac delta function
Δx_{holes}	relative displacement of the holes in the outer WGs in the designed structure along $\vec{e}_x$ [see Fig. 12 on page 34]
Δy_{WGs}	distance between the outer and the center WG in the designed structure [see Fig. 12 on page 34]
a	the length of one period
m. BZ	m-th Brillouin zone
c_0	speed of light in vacuum
c.c.	complex conjugate
d_{center}	width of the center WG in the designed structure [see Fig. 12 on page 34]
d_{side}	width of the outer WGs in the designed structure [see Fig. 12 on page 34]
$\vec{e}_{x_\alpha}$	unity vector along direction x_α
FDTD	finite-difference time-domain [simulation]
h_{WGs}	height of all WGs in the designed structure [see Fig. 12 on page 34]
H.c.	Hermitian conjugate
$\text{Im}\,(z)$	imaginary part of $z \in \mathbb{C}$

$\left(\vec{F}, \vec{G}\right)$	inner product of the vector fields $\vec{F}$ and $\vec{G}$ as defined by (7) on page 5
$\mathrm{JSA}_{m_p\, m_s\, m_i}$	joint spectral amplitude for a pump mode of bandlet m_p, signal mode of bandlet m_s and idler mode of bandlet m_i
k	wave vector component along propagation direction $\vec{e}_x$
$\boxed{\mathrm{PM}}_{m_p\, m_s\, m_i}$	complex phase-mismatch term as shown in (43) on page 20
L	full length of the simulated structure
$\mathrm{LiNbO_3}$	lithium niobate
MEEP	MIT Electromagnetic Equation Propagation [an FDTD solver]
$\boxed{\mathrm{MO}}_{m_p\, m_s\, m_i}$	mode-overlap term as shown in (41) on page 19
MPB	MIT Photonic-Bands [eigenmode-solver for electro-magnetic problems]
n_{gr}	group index as defined by (14) on page 8
$\boxed{n_{\mathrm{gr}}}_{m_s\, m_i}$	mode-overlap term as shown in (42) on page 19
PC	photonic crystal
$\mathrm{Re}\,(z)$	real part of $z \in \mathbb{C}$
r_{holes}	radius of the cylindrical holes in the outer WGs in the designed structure [see Fig. 12 on page 34]
$\mathrm{SiO_2}$	silica
SPDC	spontaneous parametric down conversion
UC	unit cell
WG	waveguide
w.l.o.g.	without loss of generality

Declaration of Authorship

I hereby declare that I am the sole author of this master thesis and that I have not used any sources other than those listed in the bibliography and identified as references. I further declare that I have not submitted this thesis at any other institution in order to obtain a degree.

On the part of the author there are no objections to making this master thesis publically available.

Jena, 14$^{\text{th}}$ of March 2017

_____

Johannes Wilde